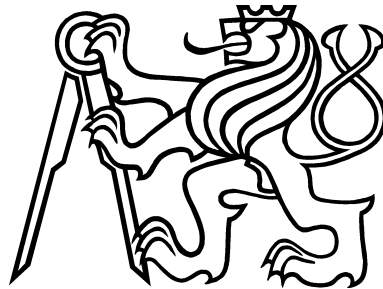CZECH TECHNICAL UNIVERSITY IN PRAGUE

Faculty of Nuclear Sciences and Physical Engineering
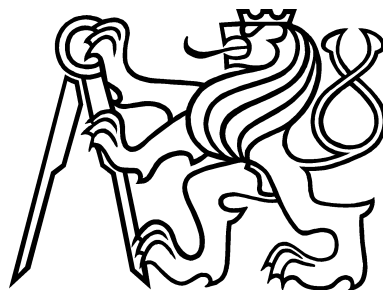
DIPLOMA THESIS

Influence of Pile-up on Search for Black Holes at LHC

Prague, 2011   Bc. Michal Vlasák

ČESKÉ VYSOKÉ UČENÍ TECHNICKÉ V PRAZE

Fakulta jaderná a fyzikálně inženýrská

DIPLOMOVÁ PRÁCE

Vliv pile-up událostí na hledání černých děr na LHC

Praha, 2011   Bc. Michal Vlasák

Prohlášení

Prohlašuji, že jsem svou diplomovou práci vypracoval samostatně a použil jsem pouze podklady (literaturu, projekty, SW atd.) uvedené v přiloženém seznamu.

V Praze dne _____   _____

                                            podpis

Acknowledgement

stránka se zadáním

Influence of Pile-up on Search for Black Holes at LHC

Author: Bc. Michal Vlasák

Field of Study: Nuclear Engineering

Specialization: Experimental Nuclear Physics

Supervisor: Prof. RNDr. Vladislav Šimák, DrSc., (FNSPE, CTU)

Consultant: -

Abstract:

The possibility of producing microscopic black holes at particle colliders such as the Large Hadron Collider (LHC) results from consequences of certain extra-dimensional theories. Once these microscopic black holes are produced, they evaporate via the Hawking radiation into several Standard Model particles which could be then detected and studied at the ATLAS detector. Nevertheless, at the LHC energy of $\sqrt{s} = 14$ TeV and the luminosity of 10^{34} cm^{-2}s^{-1} several additional soft collisions, the so-called pile-up, occur and represent a serious background.

Study of the influence of pile-up events on the microscopic black holes searches is the aim of this thesis. Since microscopic black holes are expected to decay mostly to quarks and gluons and in the view of the further multi-jet final state analysis, the main attention is focused on jets production and on finding the optimal jet cuts to suppress the pile-up effects. Jets with $p_T > 50$ GeV and $|\eta| < 2.8$ present optimal way to neglect pile-up effects and they are used in the following multi-jet final state study of microscopic black holes with real data collected in 2010 in pp collisions at $\sqrt{s} = 7$ TeV and with integrated luminosity of ~ 35 pb^{-1}.

Keywords: LHC, extra dimensions, microscopic black hole, jet, pile-up

Vliv pile-up událostí na hledání černých děr na LHC

Autor: Bc. Michal Vlasák

Obor: Jaderné inženýrství

Specializace: Experimentální jaderná fyzika

Vedoucí práce: Prof. RNDr. Vladislav Šimák, DrSc., (FJFI, ČVUT)

Konzultant: -

Abstrakt:

Možnost produkce mikroskopických černých děr na částicových urychlovačích jako je Large Hadron Collider (LHC) plyne z důsledků některých extra-dimenzionálních teorií. Vzniklé mikroskopické černé díry se poté vypaří Hawkingovým zářením na několik částic standardního modelu, které mohou být zaznamenány a studovány detektorem ATLAS. Ovšem, při energii LHC $\sqrt{s} = 14$ TeV a luminozitě 10^{34} cm^{-2}s^{-1} se objevuje další vážné pozadí ve formě měkkých srážek, tzv. pile-up.

Cílem této práce je studium vlivu pile-up událostí na hledání mikroskopických černých děr. Hlavní pozornost je věnována zejména na produkci jetů a na nalezení optimálních selekčních kritérií na potlačení pile-up efektů, a to nejen z důvodu předpokládaného rozpadu mikroskopických černých děr převážně na kvarky a gluony, ale také s ohledem na následující analýzu multi-jetového kanálu. Optimální kritéria na jety pro zanedbání pile-up efektů jsou $p_T > 50$ GeV a $|\eta| < 2.8$. Tyto výsledky jsou dále použity v analýze multi-jetového kanálu mikroskopických černých děr s reálnými daty nasbíraných v roce 2010 v pp srážkách při $\sqrt{s} = 7$ TeV a integrované luminositě ~ 35 pb^{-1}.

Klíčová slova: LHC, extra dimenze, mikroskopická černá díra, jet, pile-up

Contents

List of Figures

List of Tables

Preface

The production of microscopic black holes at particle colliders presents one of the most exciting consequences of some theories containing additional extra dimensions. These scenarios, developed in recent years, assume that only gravity might propagate into extra dimensions whereas all other Standard Model fields live on the familiar three-dimensional brane.

The Large Hadron Collider in CERN near Geneva is the first particle collider able to create these microscopic black holes. It is expected that they would evaporate quickly into several Standard Model particles via the so-called Hawking radiation, which could be then detected at the ATLAS detector. Therefore, detailed analyses of the real data collected are needed to observe any signs of this exotics phenomena.

At the Large Hadron Collider additional multiple proton-proton interactions are expected to occur, the so-called *pile-up*. These additional soft collisions are not related to the physics event and represent a serious background. Moreover, it is assumed that the pile-up influence will increase with the luminosity and the centre-of-mass energy. Hence, the suppression of these pile-up effects is challenging and inevitable for further physical analysis.

The aim of this thesis is to study the influence of pile-up on microscopic black holes searches. In the following, especially the study of pile-up influence on the jet signal is under investigation. The purpose is to find optimal jet criteria to suppress this additional background and use them in the further analysis. After that, the microscopic black holes are searched for in the multi-jet final state in pp collisions with real data collected in 2010 with centre-of-mass energy of $\sqrt{s} = 7$ TeV and integrated luminosity of ~ 35 pb^{-1}.

The outline of this thesis is as follows. Chapter 1 summarizes the Standard Model of particle physics, as well as its unanswered questions and gives the motivation for new physics beyond it. A description of the ATLAS detector is in Chapter 2. In the following Chapter, the extra-dimensional scenarios are presented with their current experimental bounds and particle consequences. Assuming the possibility of this extra-dimensional framework, Chapter 4 then describes the production and decay of a microscopic black holes within extra dimensions at particle colliders. In the last Chapter, the discovery reach of microscopic black hole at ATLAS is simulated and discussed along with the study of the pile-up influence on jet production. Finally, the results of microscopic black hole searches in multi-jet final state are presented.

Chapter 1

Theoretical Framework

Physicists have successfully described three of the four known particle interactions in the Standard Model of particle physics. Only gravity is still refusing to fit in the common treatment. Gravity is considerably weaker than the other interactions. The strength of the electromagnetic force between two electrons is $\sim 10^{40}$ larger than the gravitational one. The electroweak energy scale and the Planck scale, at which gravitational interactions become strong, differ by about sixteen orders of magnitude. This large difference between the scales of the two fundamental interactions is known as the hierarchy problem.

The purpose of first Chapter is to briefly summarize the Standard Model of particle physics, introduce its weak and not yet solved parts and propose a solution of hierarchy problem by supposing extra spatial dimensions. The Large Hadron Collider is able to observe some of the signs of extra-dimensional scenarios as, for example, production of microscopic black holes. These microscopic black holes are generally expected to be very unstable, decaying quickly into all spectrum of Standard Model particles via the Hawking radiation.

1.1 Standard Model

The Standard Model of particle physics, developed in the early 70's, has successfully explained a lot of experimental results from particle experiments. This model well describes the standard blocks of matter, quarks and leptons, and also three out of four fundamental interactions[1]: the electromagnetic, the weak, and the strong interaction. Furthermore, it introduces all their carrier particles, and explains extremely well how these forces act on all the matter particles.

All existing hadrons are well described and classified by the quark model, independently proposed by Murray Gell-Mann and George Zweig in 1964 [1]. In the quark model, baryons are composed of three quarks (qqq), as proton $p = (uud)$, neutron $n = (udd)$, lambda $\Lambda = (uds)$, etc., and mesons are composed of a quark and an anti-quark $(q\bar{q})$, such as $\pi^+ = (u\bar{d})$, $\pi^- = (\bar{u}d)$, $K^+ = (u\bar{s})$, $K^- = (\bar{u}s)$, etc.. Nowadays, six quarks are known:

---

[1]Gravity is not yet included in the Standard Model.

up u, down d, strange s, charm c, bottom b and top t. The quarks have six degrees of freedom called "flavor" and another degree of freedom called "color". A quark with some flavor could change to another quark with different flavor via the weak interaction mediated by charged gauge bosons $W^\pm$. The "color" interaction between quarks, the strong interaction, is mediated by gluons.

Leptons are fermions as well as quarks are, but they do not have flavor or color. There are six known leptons as well: electron e^-, muon μ^-, tau τ^- and their three corresponding neutrinos ν_e, ν_μ, and ν_τ. Contrary to the quarks, leptons do not interact through the strong interaction, but only through the weak interaction, and electron, muon and tau also through the electromagnetic interaction.

There are three generations of quarks and leptons

$$\begin{pmatrix} u \\ d \end{pmatrix}, \qquad \begin{pmatrix} c \\ s \end{pmatrix}, \qquad \begin{pmatrix} t \\ b \end{pmatrix}, \tag{1.1}$$

$$\begin{pmatrix} e \\ \nu_e \end{pmatrix}, \qquad \begin{pmatrix} \mu \\ \nu_\mu \end{pmatrix}, \qquad \begin{pmatrix} \tau \\ \nu_\tau \end{pmatrix}, \tag{1.2}$$

and their main properties are listed in Tab. 1.1 and Tab. 1.2, respectively.

Quark	m [GeV]	Q	I	I_Z	S	C	B	T
u	$0.0015 - 0.0033$	$-\frac{1}{3}$	$\frac{1}{2}$	$-\frac{1}{2}$	0	0	0	0
d	$0.0035 - 0.0060$	$+\frac{2}{3}$	$\frac{1}{2}$	$+\frac{1}{2}$	0	0	0	0
s	$0.104^{+0.026}_{-0.034}$	$-\frac{1}{3}$	0	0	-1	0	0	0
c	$1.27^{+0.07}_{-0.11}$	$+\frac{2}{3}$	0	0	0	$+1$	0	0
b	$4.20^{+0.17}_{-0.07}$	$-\frac{1}{3}$	0	0	0	0	-1	0
t	171.2 ± 2.1	$+\frac{2}{3}$	0	0	0	0	0	$+1$

Table 1.1: Main properties of quarks. m: mass, Q: electric charge, I: isospin, I_Z: 3rd component of isospin, S: strangeness, C: charmness, B: bottomness, T: topness [2].

Besides quarks and leptons, the Standard Model also consists of photons γ, weak bosons $W^\pm$, Z and gluons g, which represent intermediated particles from electromagnetic, weak, and strong interaction, respectively. Photons and gluons are massless whereas weak gauge bosons $W^\pm$ and Z have masses (80.399 ± 0.023) GeV and (91.1876 ± 0.0021) GeV [2], respectively[2].

The Higgs boson is the last piece of the Standard Model, which has not yet been discovered. This particle plays the key role in explaining the origin of mass of other elementary particles and the mass hierarchy between, for example, the massless photon and the very heavy $W^\pm$ and Z bosons. Since 1964, when Peter Higgs developed the

---

[2] Unless stated otherwise, familiar natural units $c = \hbar = k_B = G = 1$ are assumed in this thesis.

Lepton	m [MeV]	Q	L_e	L_μ	L_τ
e	0.511	-1	$+1$	0	0
ν_e	$< 2.2 \cdot 10^{-6}$	0	$+1$	0	0
μ	105.65	-1	0	$+1$	0
ν_μ	< 0.17	0	0	$+1$	0
τ	1776.84	-1	0	0	$+1$
ν_τ	< 15.50	0	0	0	$+1$

Table 1.2: Main properties of leptons. m: mass, Q: charge, L_e: electron number, L_μ: muon number, L_τ: tau number [2].

Higgs field theory and proposed that the Universe is pervaded by this field [3], [4], particle physicists have been looking for evidence of its existence.

Even though the Standard Model predicts that the Higgs boson should exist, it does not predict its exact mass. The most stringent direct lower limit on the Higgs boson mass is from a combination of searches at the four LEP (Large Electron Positron collider) experiments, yielding $m_H > 114.4$ GeV [5]. On the other hand, precision electroweak fits constrain the mass to $m_H < 144$ GeV [6]. Experiments at Fermilab, D0 and CDF, excluded the Higgs mass around 170 GeV [7], [8]. Current experimental limits on the Higgs boson mass are shown in Fig. 1.1.
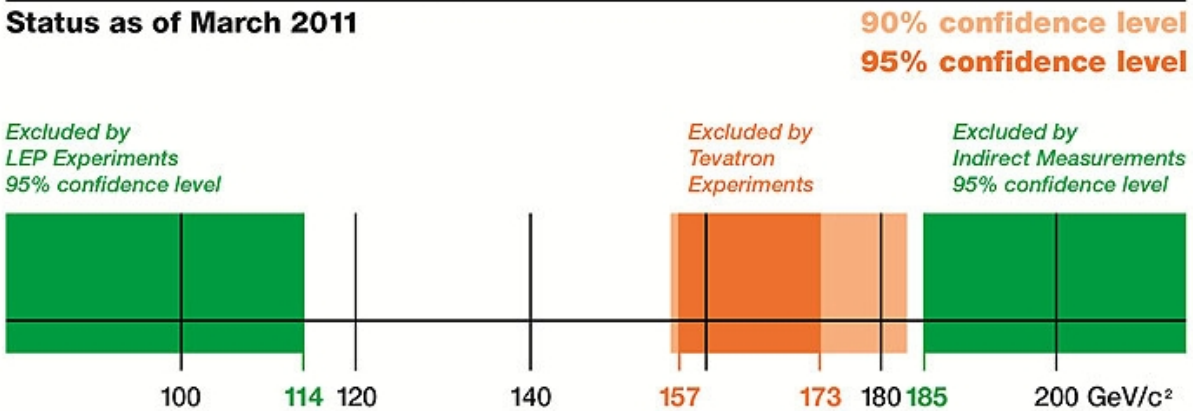
Figure 1.1: Current limits on the Higgs boson mass [9].

Nowadays, the Standard Model presents well experimentally tested theory, however, it does not represent the final model or theory at all. As it will be discussed in the next Section, the Standard Model keeps many questions unanswered. There could as well be a phenomena awaiting discovery, especially at high energies, which is not described by the Standard Model.

1.2 Motivation for New Physics

The Standard Model presents the best model which particle physicists have until now. However, even though this model agrees with particle experiments results, it rests a number of shortcomings and problems to solve, which will be briefly introduced in the following.

Newton's unfinished business...

As an example of the Standard Model problems is mass itself. Where does the mass come from? What is the origin of the mass? Why do some of elementary particles have the masses they have and why the others have not? Important question is also whether neutrinos have small but finite mass(es) or if they are massless. Answer to this question may have important consequences in astrophysics and cosmology. The most likely explanation of the particles mass problem today may be the Higgs mechanism.

An invisible problem...

Another example is an "invisible" problem. Today's visible Universe, from an ant to a galaxy, is made up of known ordinary particles. If one takes all these particles together, all planets, stars, and galaxies, it gives only 4% of the Universe. What is 96% of the Universe made of? These 96% is commonly called *dark matter* and *dark energy*, and they are incredibly difficult to detect and observe. So far they could have been studied only via cosmological observations through the gravitational forces they exert as, for example, galaxy rotation. Dark matter and dark energy are one of the most exciting and biggest challenges of particle physics and cosmology.

Nature's favouritism...

The idea of antimatter is known since 1928 (Paul Dirac) and it was experimentally confirmed in 1932 (Carl David Anderson). Nowadays, it is clear that antiparticles do exist, however, everything in the visible Universe is made of matter, not antimatter. Take a look at the birth of the Universe, the Big Bang, or more likely at few moments after the Big Bang, when matter and antimatter were created. Matter and antimatter then annihilated into the so called relict background, however, somehow a tiny fraction of matter survived and then formed the whole known Universe. Why is there no more antimatter? And what was the reason that made this tiny fraction? Is the baryon number conserved or not?

This huge disproportion between matter and antimatter is also known as the *baryon asymmetry*. The convenient dimensionless number, which characterizes the magnitude of the baryon asymmetry of the Universe, is the ratio of the baryonic charge density $(n_B - n_{\bar{B}})$ to the number density of photons, n_γ, in cosmic microwave radiation, given as

$$\beta = (n_B - n_{\bar{B}})/n_\gamma \simeq 3 \cdot 10^{-10}. \tag{1.3}$$

This number is about eight orders of magnitude higher than it has been obtained by any theory without violation of baryon number conservation.

The necessary conditions for the generation of the asymmetry, as formulated by A. D. Sakharov [10], are following: (1) Violation of the baryon number (B) symmetry, (2) violation of the discrete symmetries C (charge conjugation) and CP (the composition of parity and C), and (3) deviation from thermal equilibrium in the early Universe.

Theories that explain how to produce such a tiny number, *theories of baryogenesis*, represent perhaps the best example of the perfect interplay between particle physics and cosmology. Until now, many mechanisms for the generation of the baryon asymmetry have been proposed, but there is no idea which one is correct. Grand Unified Theories which, among others, predict baryon number violation are perfect candidates for a theory of baryogenesis [11].

Hidden worlds...

In 1921, Theodor Kaluza showed in his paper "Zum Unitätsproblem der Physics" [12] that the gravitational and electromagnetic field could be geometrically unified in five dimensions. The idea of Kaluza-Klein theory [13], [14] was received by unified-field theorists. This idea of extra dimension(s) and unification of forces led through multi-dimensional supergravity theories in the 1980s to the current favorite contenders for a possible "theory of everything", ten-dimensional superstrings. Are there any extra dimensions? And how many? If extra dimensions do exist, what kind of particles could live there and how experimental particle physicists would find these hidden dimensions or some of their signs in the "standard" four-dimensional world?

Problems above mentioned represent only a part of the Standard Model "black clouds" which have not yet been solved or explained. Besides the question of the origin of particle masses, dark energy, baryon asymmetry or the idea of extra dimensions, the Standard Model has also an unfinished business with the gravity. Gravity is not included in the Standard Model and if the fundamental forces could be unified, this unifying theory has to also answer the question of how to construct a consistent quantum theory of gravity. Another "skeleton in the closet" is the hierarchy problem, which will be described in the next Section.

The good news is that many of these questions could be early answered by experiments at the Large Hadron Collider as, for example, the ATLAS experiment, which will be briefly described in Chapter 2.

1.3 Hierarchy Problem

In previous sections the Standard Model of particle physics was presented also with some of its "weak" parts, which it could not describe well yet. As it was already mentioned, the Standard Model works exceptionally well in explaining many diverse experimental results. However, there is also a significant mystery, one whose solution is almost bound to lead to

new insights into the underlying structure of matter. In this Section this mystery will be introduced, known to particle physicists as the *hierarchy problem.*

The basic question seems to be "What is and what represents hierarchy problem and where does it come from?". One can find a short explanation and answer in Lisa Randall's response [15]:

> *"The gist of it is that the universe seems to have two entirely different mass scales, and we don't understand why they are so different. There's what's called the Planck scale, which is associated with gravitational interactions. It's a huge mass scale, but because gravitational forces are proportional to one over the mass squared, that means gravity is a very weak interaction. In units of GeV, which is how we measure masses, the Planck scale is 10 to the 19th GeV. Then there's the electroweak scale, which sets the masses for the W and Z bosons. These are particles that are similar to the photons of electromagnetism and which we have observed and studied well. They have a mass of about 100 GeV. So the hierarchy problem, in its simplest manifestation, is how can you have these particles be so light when the other scale is so big."*

It is important to point out that the hierarchy problem is not caused by any disagreements or differences between the Standard Model predictions and experimental results.

The hierarchy problem presents a devastating hidden family secret lurking inside the Standard Model. If one uncritically assumes that the strength of electromagnetic and weak force and the gauge boson masses take the values that have been measured in experiments then everything agrees with prediction. However, if one takes a look at the mass parameter (the weak scale mass that determines the elementary particle masses) one could find out it is ten million billion times, or sixteen orders of magnitude, lower than the mass expected from general theoretical considerations. By guessing the value of the weak scale mass based on a high-energy theory one may obtain it and therefore all particle masses too, but completely wrong.

The hierarchy problem could be explained, for example, as a question of why gravity is so weak or, from another point of view, as the question of why the Higgs boson mass, and hence the weak gauge boson masses, are so small. Nevertheless, no matter what point of view one chooses, the hierarchy problem represents a gaping hole in the understanding of particle physics.

1.3.1 Hierarchy Problem in Grand Unified Theory

One could clearly see from Tab. 1.1 and Tab. 1.2 that the Standard Model particles do not have the same masses, charges, and other properties. Particle physicists do not think these particles should all have the same properties. However, it is expected that particles experiencing similar forces would be somewhat similar, for example, to have comparable[3]

---

[3]This is a similar assumption as, for example, an expectation that the height of twin brothers will be (almost) the same. It could be a little bit bizarre if one of them would have say 4 ft. and the other one 7 ft. or the first one would be 10 times higher then the second one.

masses in a single theory, such as a Grand Unified Theory (GUT). Unfortunately, in a GUT the masses are not at all the same or within certain limits similar. And not only by a factor of ten or thousand, but the mismatch between masses is more like a factor of ten trillion.

As an example, one could take the Higgs boson. It is expected that the Standard Model Higgs boson mass would be in order to 100 GeV which is relatively light particle. A GUT Higgs boson partner of the Standard Model one, on the other hand, has to be extremely heavy. And "heavy" means with the mass of roughly the GUT scale mass. In other words, in the GUT force symmetry, these two particles related by this symmetry have to have enormously different masses. In GUT the weak and the strong interactions are unified, so that every particle connected with the weak force must also have some partner connected with the strong force.

Moreover, the GUT partner of Standard Model Higgs boson is able to interact simultaneously with a quark and a lepton, in other words, it transforms a quark to a lepton and vice versa and thereby it enables the proton to decay. Today's limits of proton life time agree with the expectation that if the GUT Higgs boson exists it has to have a mass similar to a GUT scale mass, about one million billion GeV. As Lisa Randall says in her book [16]: "*If this particle existed but was not this heavy, you and this book would decay before you finished reading this sentence.*"

Even though one does not see this mass problem or is wiling to assume without any explanation that one particle is light and the other is extremely heavy, one would still run into problems with an effect called *quantum mechanics contribution*, which will not be described here but more information can be found in [16].

1.3.2 Hierarchy Problem of Particle Physics

Up to now, it was rather the GUT hierarchy problem, but the true hierarchy problem is worse. As it was already mentioned, the theory consisting of the Standard Model combined with gravity contains two enormously different energy scales. First one, the weak scale energy at which electroweak symmetry is broken, which is ~ 250 GeV, and second one, the Planck scale energy, which determines the strength of gravitational interactions, which is $\sim 10^{19}$ GeV.

Gravity could always be safely ignored for the most calculations in particle physics. A huge Planck scale mass equivalent to extremely feeble gravity gives particle physicists a basic question they would like to answer: Why is gravity so weak that it can be ignored in particle physics calculations? Or, in other words, why Planck scale mass is so huge? Why is it ten million billion times higher than the masses relevant to particle physics scales, all of which are less than a few hundred GeV?

Take an example of particle physicist who knows gravity's strength but knows nothing about measured weak gauge boson masses. If one would ask this physicist to estimate the Higgs particle's mass using quantum field theory then as Lisa Randall in [16] notices: "*... he would conclude from his calculation that the ratio between the Planck scale mass and the mass of the Higgs particle (or the weak scale mass, which is determined by the Higgs*

particle's mass) should be far closer to unity than to ten million billion! His estimate of the weak scale mass would be so close to the Planck scale mass that particles would all be black holes, and particle physics as we know it would not exist." And as Lisa Randall continues "*Although he would have no a priori expectation for the value of either the weak scale mass or the Planck scale mass individually, he could use quantum field theory to estimate the ratio and he would be totally wrong. Clearly, there is an enormous discrepancy here.*"

1.4 Extra Dimension(s) on Stage

The hierarchy problem represents really urgent mystery confronting the Standard Model. The hierarchy problem was the main motivation to start searching for new physics beyond the Standard Model. These searches lead to a birth of many hoping-to-be-physical theories like technicolor, grand unified theories, supersymmetry, and also models with extra dimension(s).

Theories with extra dimensions are probably one of the most untypical and at the same time fascinating adepts to solve the hierarchy problem and also to try to unify fundamental forces. Extra dimensions might play a crucial role in solving some of the puzzles of the Universe and they have opened one's eyes and imaginations to a new amazing possibilities. As it will be shown later in Chapter 3, there are more options of shapes and sizes of extra dimensions. For example, the scenario suggested that the apparent hierarchy between two fundamental scales of nature is generated by a large volume of extra dimensions, whereas another framework proposed that observed hierarchy results from a strong curvature of the extra-dimensional space.

Which one, if any, of these ideas is correct and describes the real world? The answer is not yet known. However, the fantastic thing is that this question could be answered soon. There are and there will be tests of extra-dimensional spacetime in astrophysics or cosmology, and more, some of the extra-dimensional consequences will be experimentally tested at the Large Hadron Collider experiments.

There are some interesting consequences which result from extra-dimensional theories such as the Standard Model particles "live" in the four-dimensional brane, whereas gravity or some not-yet-known particles are able to propagate through extra dimensions. At least there is the most exciting and impressive one - the possibility to create a microscopic black holes at particle accelerators such as the Large Hadron Collider. This exotic consequence of extra-dimensional models will be discussed in more detail in Chapter 4.

Chapter 2

Overview of ATLAS Detector

The ATLAS (**A T**oroidal **L**HC **A**pparatu**S**) detector is one of the Large Hadron Collider's (LHC) experiment. The ATLAS experiment was proposed in its current form in 1994, and officially funded by the CERN member countries at the beginning of 1995.

Besides confirming the present experimental results, the aim of the ATLAS detector is to find the last, not yet observed, Standard Model particle - the Higgs boson [18], and also to probe (or rule out) the new theories beyond the Standard Model, mentioned in the previous Chapter. This machine is designed to study in detail all physical properties of particles originating from proton-proton (or ion-ion) collisions.

In this Chapter, a brief description of the main parts of the ATLAS detector will be presented. The ATLAS trigger and data acquisition system will be describe in the last Section.

2.1   Physics Requirements and Detector Overview

First of all, let one briefly summarise the coordinate system and nomenclature used to describe the ATLAS detector and the particles. The interaction point in the centre of the ATLAS detector is defined as the origin of the coordinate system. The z-axis is defined by the beam direction and the $x-y$ plane is transverse to the beam direction. The positive x-axis is defined as pointing from the interaction point to the centre of the LHC ring and the positive y-axis is defined as pointing upwards. The side-A of the detector is defined as that with positive z and side-C is that with negative z. The azimuthal angle ϕ is measured as usual around the beam axis, and the polar angle θ is the angle from the beam axis.

In experimental particle physics, pseudorapidity, η, is a commonly used spatial coordinate describing the angle of a particle relative to the beam axis. It is defined as

$$\eta = -\ln\tan\left(\frac{\theta}{2}\right). \tag{2.1}$$

Figure 2.1: Left: Civil Engineering in the ATLAS cavern in February 2000 [19]. Right: A historical moment: Closure of the LHC beam pipe ring on 16th June 2008 [20].

In terms of η, the detector can be divided in three sections:

- Barrel: $|\eta| < 1.05$

- Extended Barrel: $1.05 < |\eta| < 1.4$

- Endcap: $|\eta| > 1.4$.

The distance ΔR in the pseudorapidity-azimuthal angle space is defined as

$$\Delta R = \sqrt{\Delta \eta^2 + \Delta \phi^2}. \tag{2.2}$$

As was mentioned above, the ATLAS detector has great ambitions. It will provide a rich physics potential, ranging from more precise measurements of Standard Model parameters to the search for new physics phenomena. Since small cross-section is expected for many of the processes mentioned, the formidable LHC luminosity and resulting interaction rate are needed. However, at designed luminosity, the LHC will produce a total rate of 10^9 inelastic events. It means that every candidate event for new physics will on the average be accompanied by 23 inelastic events per bunch-crossing which presents a serious experimental difficulty. All benchmark physics' goals can be turned into a set of general requirements for the LHC detectors [17]:

- Due to the experimental conditions at the LHC, the detectors require fast, radiation-hard electronics and sensor elements. In addition, high detector granularity is needed to handle the particle fluxes and to reduce the influence of overlapping events.

- Large acceptance in pseudorapidity with almost full azimuthal angle coverage is required.

- Good charged-particle momentum resolution and reconstruction efficiency in the inner tracker are essential. For offline tagging of τ-leptons and b-jets, vertex detectors close to the interaction region are required to observe secondary vertices.

- Very good electromagnetic calorimetry for electron and photon identification and measurements, complemented by full-coverage hadronic calorimetry for accurate jet and missing transverse energy measurements, are important requirements, as these measurements form the basis of many of the studies mentioned above.

- Good muon identification and momentum resolution over a wide range of momenta and the ability to determine unambiguously the charge of high p_T muons are fundamental requirements.

- Highly efficient triggering on low transverse-momentum objects with sufficient background rejection, is a prerequisite to achieve an acceptable trigger rate for most physics processes of interest.

The overall ATLAS detector layout is shown in Fig. 2.2.
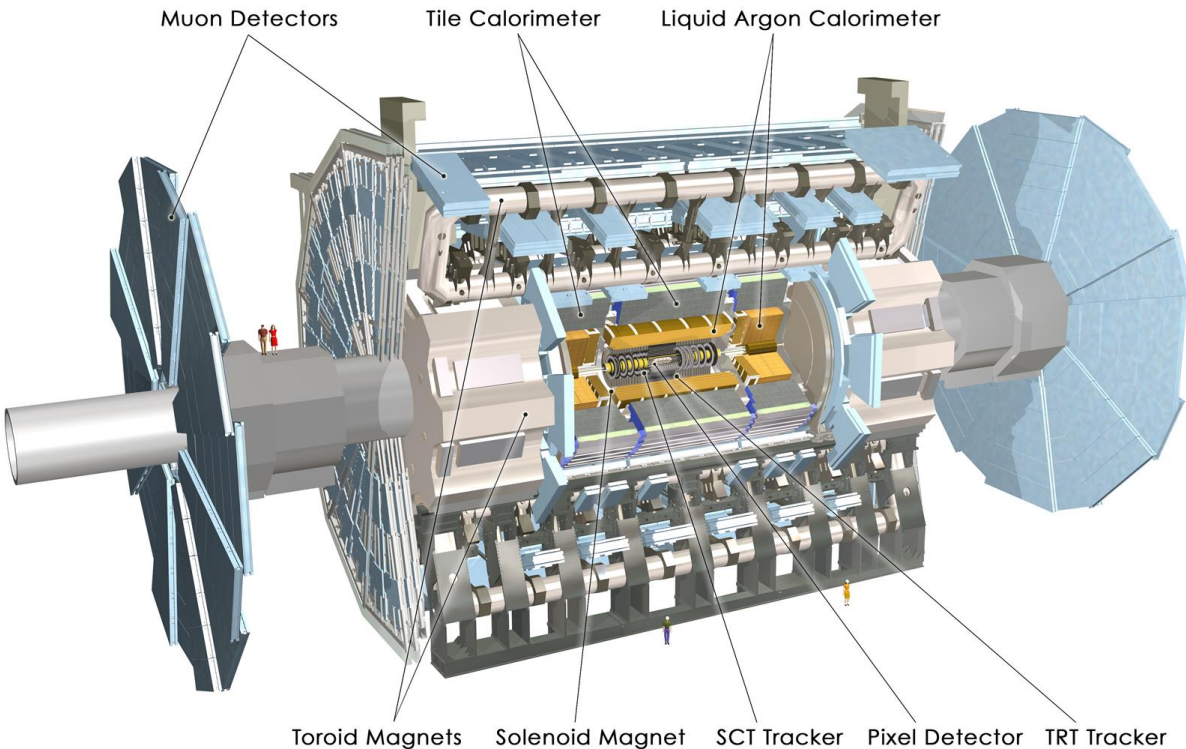
Figure 2.2: Cut-away view of the ATLAS detector. The dimensions of the detector are 25 m in height and 44 m in length. The overall weight of the detector is approximately 7000 tonnes [17].

2.2 Inner Detector

The inner detector is the closest to the beampipe. It spans 2.3 m in height and 7.0 m in length. It is made of three subdetectors: the **Pixel Detector**, the **SemiConductor Tracker** (SCT) and the **Transition Radiation Tracker** (TRT). The layout of the Inner Detector is illustrated in Fig. 2.3.

The inner detector is enclosed in a 2 T solenoidal magnetic field, generated by about 10 km of superconducting cable, wound into a coil at the inner surface of the calorimeter cryostat. The outer wall of the cryostat acts as a return yoke for the magnetic field. The coil, weighing about 4 tons, is cooled to 4.5 K by liquid helium. The main parameters of the inner detector are summarised in Tab. A.1 (in Appendix A).
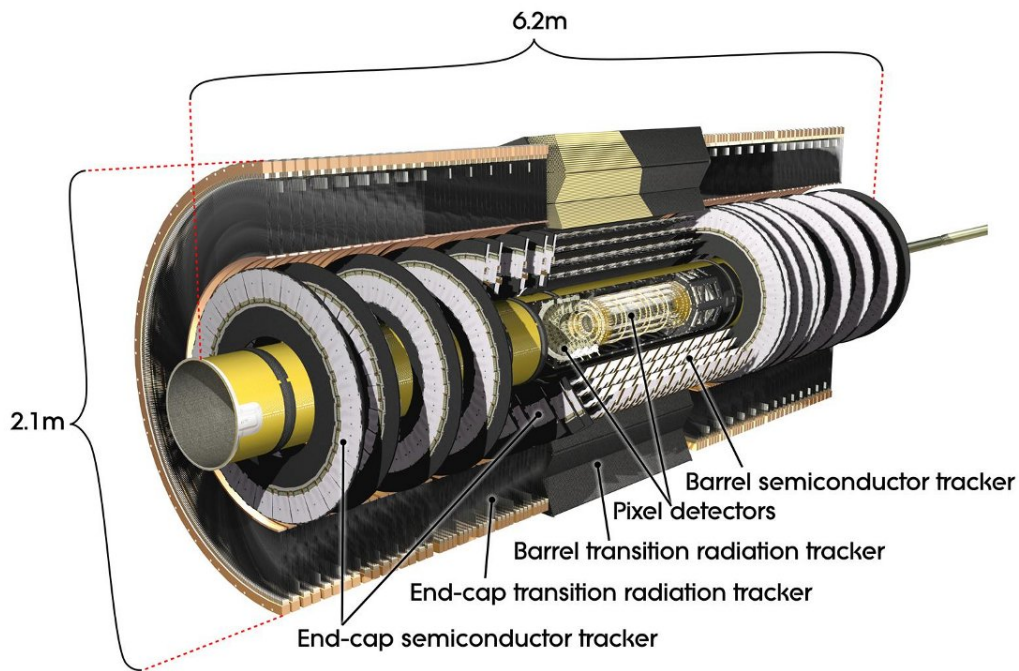
Figure 2.3: Overview of the ATLAS inner detector [17].

Pixel Detector

The pixel detector is the innermost detector in the inner detector. It is made up of three layers of silicon modules in the barrel and three wheels in each end-cap. There is a total number of 1744 modules, each measuring two by six centimetres. Each module is built from a 250 μm thick silicon sensor divided into pixels of 50×400 μm. About 80 million readout channels are needed, which is about 50% of the total readout channels. The pixel provides three absolute position measurements along the charged tracks and is particularly useful to determine the position of secondary decay vertices in the event.

SemiConductor Tracker

The SemiConductor Tracker (SCT) is located around the pixel detector, from $R = 25.5$ cm to $R = 54.9$ cm in the barrel and $R = 25.1$ cm to $R = 61.0$ cm in the end-cap. Silicon strips are used with 80 μm pitch assembled in double-sided modules with a stereo angle of 40 mrad between the two sides. Four different geometries for the 4088 modules are used: rectangular module in the barrel and three wedge-shaped module geometries in the end-caps. They are suited for the three different rings of modules on the end-cap disk: inner, middle and outer. The number of rings of SCT disks varies between one to three, starting from the outer ring. The thickness of the silicon sensoris 285×15 μm. The total number of readout channels is approximately 6 million and covers a surface of silicon of 63 m^2. Therefore, the SCT presents one of the largest existing silicon detectors.

Transition Radiation Tracker

The Transition Radiation Tracker (TRT) is the last layer of the inner detector. The TRT is a straw tube detector interleaved with thin foil which provides transition radiation photons to be detected by the straw tubes. In the barrel, the detector is divided into 32 modules composed of three rings and the straws are parallel to the beam axis. In each end-cap, 20 wheels are assembled together, in which the straws are perpendicular to the beam axis. The 4 mm straw tube forms the cathode and a 31 μm gold-plated tungsten wire forms the grounded anode. The number of readout channels is approximately 351000. The combination of precision trackers at small radii with the TRT at a larger radius gives very robust pattern recognition and high precision in both $R - \phi$ and z coordinates.

2.3 Calorimeters

Once the neutral and charged particles have crossed the tracking system, they will reach the calorimeters, where they will shower and hence their energy will be deposited and measured in the detector. In this process, electromagnetic and hadronic matter behaves differently and needs to be treated by two separate calorimeter systems. That is the reason why ATLAS detector has the **Electromagnetic calorimeter** (EM) and the **Hadronic calorimeter** (HCAL). These calorimeters cover the range $|\eta| < 4.9$. A view of the calorimeters is presented on Fig. 2.4 and the main parameters are summarised in Tab. A.2 (in Appendix A).

2.3.1 LAr Electromagnetic Calorimeter

The electromagnetic calorimeter is made of lead as absorber material and copper-kapton electrodes arranged in an accordion geometry. The accordion is kept in a cold Liquid Argon (LAr) vessel, which serves as the active material. Four individual vessels form the detector: two half-barrels and two end-caps, covering up to pseudorapidity $|\eta| < 3.2$. There is a small gap at $|\eta| = 0$ and one at $1.37 < |\eta| < 1.52$. The calorimeter is divided into three
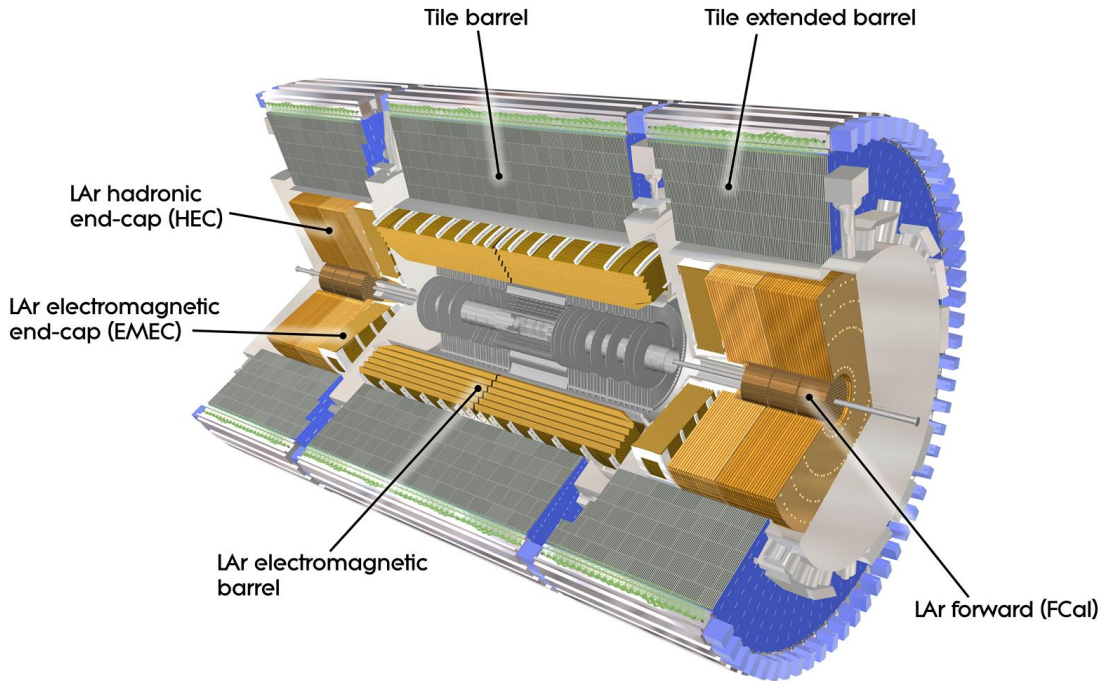
Figure 2.4: Scheme of the full calorimeter [17].

radial layers (two in certain regions of pseudorapidity) and has a decreasing granularity as a function of distance from the beampipe. In the region of $|\eta| < 1.8$, a presampler detector is used to correct for the energy lost by electrons and photons upstream of the calorimeter.

2.3.2 Hadronic Calorimeter

The hadronic calorimeter uses two different technologies to absorb the hadrons from the collisions. At $1.5 < |\eta| < 3.2$, the **Hadronic End-Caps** (HEC) use LAr technology and are located inside the same cold vessels as the EM calorimeter. The HEC consists of two independent wheels, each equipped with 32 wedge-shaped modules, using copper plates as absorber material. To minimize the drop in material density at the transition between the end-cap and the forward calorimeter (around $|\eta| = 3.1$), the HEC extends out to $|\eta| = 3.2$, thereby overlapping with the forward calorimeter. Similarly, the HEC η range also slightly overlaps that of the tile calorimeter ($|\eta| < 1.7$) by extending to $|\eta| = 1.5$.

Surrounding the EM and HEC calorimeters, the **Tile Calorimeter** (TileCal) uses steel plates as absorber material interleaved with scintillator tiles as active material. It is divided into two parts: the Barrel covering the range $0 < |\eta| < 1.0$ and the Extended Barrel covering $0.8 < |\eta| < 1.7$. The barrel and extended barrels are divided azimuthally into 64 modules. Radially, the tile calorimeter extends from an inner radius of 2.28 m to an outer radius of 4.25 m. It is segmented in depth in three layers, approximately 1.5, 4.1

and 1.8 interaction lengths (λ) thick for the barrel and 1.5, 2.6, and 3.3 λ for the extended barrel. The total detector thickness at the outer edge of the tile-instrumented region is 9.7 λ at $\eta = 0$.

Finally, a **Forward Calorimeter** (FCal) system is needed to cover the pseudorapidity range up to 4.9. The FCal is made of three layers: one for EM particle detection using copper plates as absorber and two more for hadronic particle detection using Tungsten plates as absorber. The detector is housed in the LAr vessel. The FCal is approximately 10 interaction lengths deep, and consists of three modules in each end-cap: the first, made of copper, is optimised for electromagnetic measurements, while the other two, made of tungsten, measure predominantly the energy of hadronic interactions. Each module consists of a metal matrix, with regularly spaced longitudinal channels filled with the electrode structure consisting of concentric rods and tubes parallel to the beam axis.

2.4 Muon Chambers

The conceptual layout of the muon spectrometer is shown in Fig. 2.5 and the main parameters of the muon chambers are summarised in Tab. A.3 (in Appendix A). The muon spectrometer is designed with two separate sets of detectors: trigger chambers (fast) and precision chambers (slow). They are enclosed in the toroidal magnet system of ATLAS which provides strong bending power in a large empty volume, allowing for a minimization of multiple scattering effects and a good charge identification for high p_T muons. The precision chambers allow one to have good momentum resolution without loss of trigger efficiency.

The muon spectrometer is based on the magnetic deflection of muon tracks in the large superconducting air-core toroid magnets, instrumented with separate trigger and high-precision tracking chambers. Over the range $|\eta| < 1.4$, magnetic bending is provided by the large barrel toroid. For $1.6 < |\eta| < 2.7$, muon tracks are bent by two smaller end-cap magnets inserted into both ends of the barrel toroid. Over $1.4 < |\eta| < 1.6$, usually referred to as the transition region, magnetic deflection is provided by a combination of barrel and end-cap fields. This magnet configuration provides a field which is mostly orthogonal to the muon trajectories, while minimising the degradation of resolution due to multiple scattering.

The precision tracking muon system is composed of two subdetectors: the **Monitored Drift Tubes** (MDTs) and the **Cathode Strip Chambers** (CSCs). The MDTs provide a precision measurement of the track coordinates in the principal bending direction of the magnetic field. The MDTs occupy most of the solid angle, with three concentric layers in the barrel and up to $|\eta| = 2.7$ in the end-cap small and big wheels (located on each side of the end-cap toroid). A chamber consists of 3 to 8 layers of drift tube filled with gas. It has a maximum counting rate of 500 Hz/cm². The CSCs are used at large pseudorapidities in the innermost plane over $2 < |\eta| < 2.7$. The CSCs are a multiwire proportional chambers which use two perpendicularly segmented cathode planes to locate particles. Their maximum counting rate is 1000 Hz/cm².
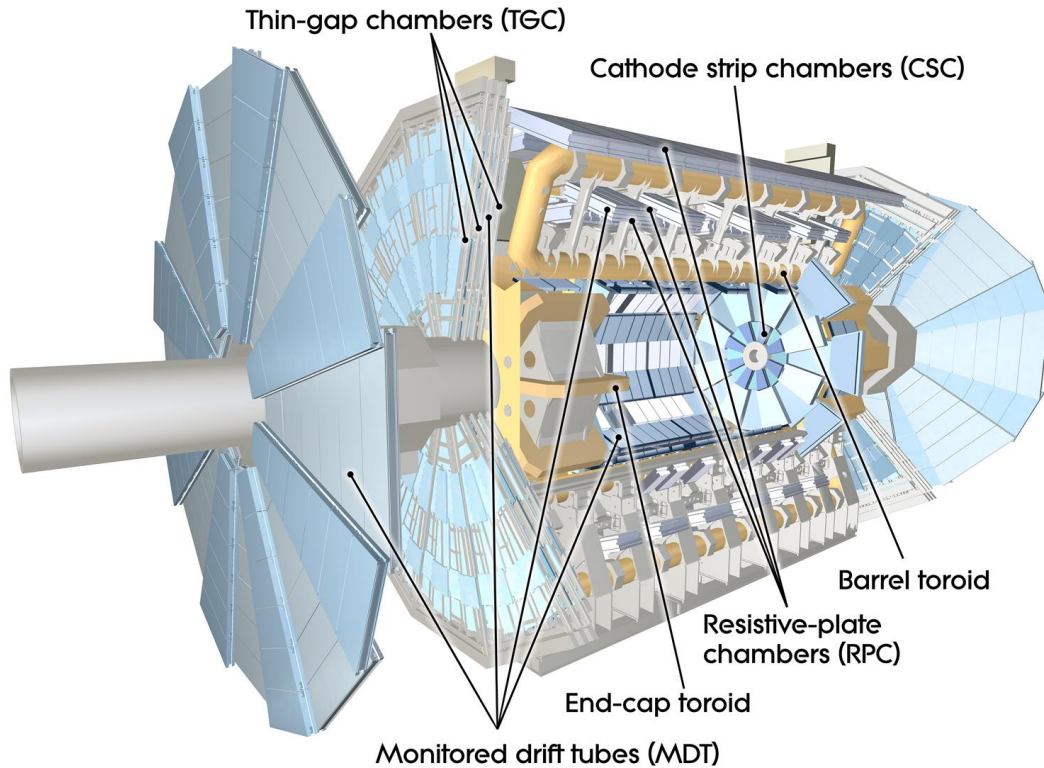
Figure 2.5: Overview of the ATLAS muon spectrometer components [17].

The trigger system covers the pseudorapidity range $|\eta| < 2.4$. The trigger chambers are also divided into two subdetectors: the **Resistive Plate Chambers** (RPCs) in the barrel and the **Thin Gap Chambers** (TGCs) in the end cap. The RPC extends to $|\eta| = 1.05$ and uses the same detection principle as a spark chamber. The TGC covers the range $1.05 < |\eta| < 2.4$ and is a multiwire proportional chamber with a smaller wire-cathode gap than the wire-wire gap. The trigger chambers for the muon spectrometer serve a threefold purpose: provide bunch-crossing identification, provide well-defined p_T thresholds, and measure the muon coordinate in the direction orthogonal to that determined by the precision-tracking chambers.

2.5   Magnet System

Fig. 2.2 shows the general layout, the four main layers of the detector and the four superconducting magnets, the **Central Solenoid** (CS), the **Barrel Toroid** (BT) and two **End-Cap Toroids** (ECT). The ATLAS magnet system consists of [17]:

- a solenoid, which is aligned on the beam axis and provides a 2 T axial magnetic field for the inner detector, while minimising the radiative thickness in front of the barrel electromagnetic calorimeter;

Figure 2.6: Left: The eight torodial magnets can be seen on the huge ATLAS detector with the calorimeter [21]. Right: ATLAS magnet toroid end-cap [22].

- a barrel toroid and two end-cap toroids, which produce a toroidal magnetic field of approximately 0.5 T and 1 T for the muon detectors in the central and end-cap regions, respectively.

Central solenoid: The central solenoid is designed to provide a 2 T axial field. Its inner and outer diameters are 2.46 m and 2.56 m so that the desired calorimeter performance can be achieved. The layout was carefully optimised to keep the material thickness in front of the calorimeter as low as possible, resulting in the solenoid assembly contributing a total of ~ 0.66 radiation lengths at normal incidence. This required, in particular, that the solenoid windings and LAr calorimeter share a common vacuum vessel, thereby eliminating two vacuum walls. Its axial length is 5.8 m and the coil mass is 5.4 tonnes.

Barrel toroid: The cylindrical volume surrounding the calorimeters and both end-cap toroids is filled by the magnetic field of the barrel toroid, which consists of eight coils encased in individual racetrack-shaped, stainless-steel vacuum vessels (see Fig. 2.6 (left)). The coil assembly is supported by eight inner and eight outer rings of struts. The overall size of the barrel toroid system as installed is 25.3 m in length, with inner and outer diameters of 9.4 m and 20.1 m, respectively.

End-cap toroids: These toroids generate the magnetic field required for optimising the bending power in the end-cap regions of the muon spectrometer system. They are supported off and can slide along the central rails, which facilitates the opening of the detector for access and maintenance. Each end-cap toroid consists of a single cold mass built up from eight flat, square coil units and eight keystone wedges, bolted and glued together into a rigid structure to withstand the Lorentz forces. With a weight of 240 tonnes, the end-cap toroids (Fig. 2.6 (right)) were some of the heaviest objects to be lowered into the cavern.

2.6 Trigger and Data Acquisition System

As already discussed, Large Hadron Collider (LHC) should work at a designed luminosity of 10^{34} cm^{-2}s^{-1} in order to allow the studies of rare events. This condition will lead to over 23 interactions per bunch crossing. Thus, each second close to 10^9 interactions occur.

Most of these interactions are minimum bias events that are of a limited interest corresponding to an amount of data of $\sim 10^4$ Gbyte s^{-1}. Therefore, it is necessary to select significant data in order to register only the interesting portion of the total amount of data coming from the collision. To satisfy this request, the ATLAS trigger system and data acquisition system (DAQ) have been designed with the challenging role of selecting bunch crossings containing significant events by reducing the data rate from 40 MHz (collision rate) to $100 - 200$ Hz with an event size of approximately 1.3 Mbyte.

The ATLAS trigger and DAQ system is based on three levels of online event selection: Level-1 (L1) trigger, Level-2 (L2) trigger, and Event Filter (EF). The L2 trigger and EF form together the High Level Trigger (HLT) (see Fig. 2.7). Each trigger level refines the decisions made at the previous level and, where necessary, applies additional selection criteria.
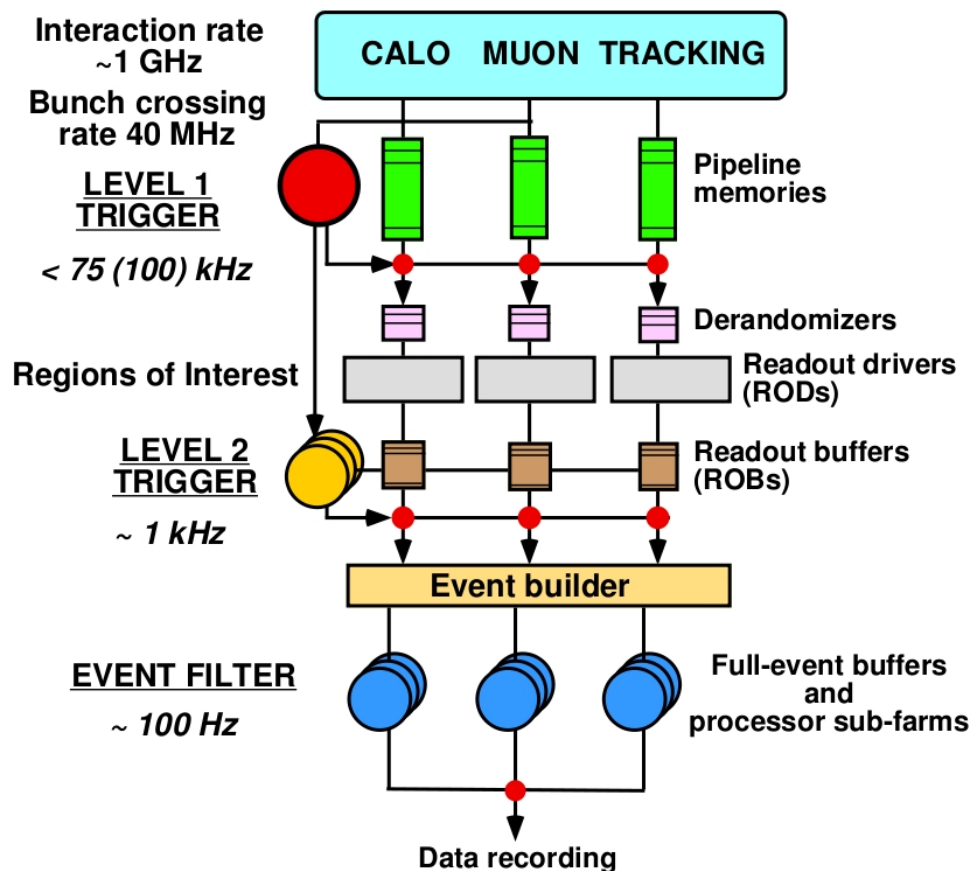
Figure 2.7: Block diagram of the Trigger/DAQ system [23].

Level-1 Trigger

The L1 trigger is designed to operate at a maximum pass rate of 75 kHz. The L1 trigger decision is based on information with a coarse granularity of two sub-detector systems: the muon trigger chambers and the calorimeters. It searches for signatures of high-p_T muons in the muon system trigger chambers (RPC and TGC), and for signatures of jets, electrons/photons clusters, τ-leptons decays, and large missing transverse energy in the calorimeter. The L1 trigger decision time must be less than 2.5 μs. The information of accepted events by the L1 trigger will be send to the L2 trigger as Regions-of-Interest (RoI) and stored in the Readout Buffers (ROBs).

Level-2 Trigger

The L2 trigger reduces further the event rate to a maximum of 3.5 kHz by using detailed information from the RoI. For a L1 muon trigger, the L2 trigger will use the information from the precision MDT chambers to improve the muon momentum estimate, which allows a tighter cut on this quantity. For a L1 calorimeter trigger, the L2 trigger has access to the full detector granularity, and has in addition the possibility to require a match with a track reconstructed in the inner detector. The L2 trigger has an event dependent latency, which varies from 1 ms for simple events to about 10 ms for complicated events.

When the L2 trigger accepts the event, it will be transfer to the event filter via the DAQ system. This process of data movement is called "Event Building". Before event building, an event is composed of many fragments which are in each ROB. The event builder collects a full event with many fragments from ROBs. After event building, this full event will be stored in a memory which is associated with the event filter. The average event processing time at this level is about 40 ms per event.

Event Filter

The event filter (EF) is the highest trigger system to reduce the event rate to ~ 100 Hz, and trigger decision time is up to ~ 1 s. The EF is able to access the full events with full granularity. Thus, the EF can reconstruct complete events by using offline reconstruction algorithms. The selected events from the EF are stored in mass storage farms. One can use the stored data for further study.

2.7 Expected Performance

To conclude the ATLAS detector description it could be useful to summarize its performance in real data-taking. In order to establish the expected performance of the detector, one has to consider two aspects simultaneously. Firstly, the hardware commissioning, i.e. how well the detector parts are working with respect to their specifications and, secondly, the physics commissioning, i.e. how well is one able to reconstruct the physics objects one wants to measure.

To achieve this, several tools are available such as the usage of simulated data, covering the various scenarios of data-taking with different center-of-mass energies, with or without pile-up and misalignment, etc. The data from test beams are also useful, as is the acquisition of cosmic ray and single beam data [17].

In the hardware commissioning phase, determination of the intrinsic accuracies and resolutions of the subdectectors using test beams is needed. For the innermost part of the ATLAS detector, the inner detector, the value for the accuracy should be sufficiently small to be able to distinguish two close-by tracks. Starting with the pixel detector, it is expected to measure hits with a precision of 10 μm in the transverse direction $(R - \phi)$ and 115 μm in the longitudinal direction (z). In the second part of the inner detector, the SCT, the longitudinal precision is reduced (due to the strip technology), leading to 17 μm in $(R - \phi)$ and 580 μm in z. For the last layer of the inner detector, the TRT, its straw drift time accuracy is 130 μm (it does not record the z position).

Move now to the next part of the detector, the calorimeters. The resolution in energy and the linearity in the response are the important parameters. Eq. (2.3) shows these parameters for the LAr calorimeter barrel, and eq. (2.4) shows the same for the tile calorimeter for $\eta = 0.35$

$$\frac{\sigma(E)}{E} = \frac{(10.1 \pm 0.4)\%}{\sqrt{(E)(\text{GeV})}} \oplus (0.2 \pm 0.1)\%, \tag{2.3}$$

$$\frac{\sigma(E)}{E} = \frac{(56.4 \pm 0.4)\%}{\sqrt{(E)(\text{GeV})}} \oplus (5.5 \pm 0.1)\%. \tag{2.4}$$

The first term is the sampling term, measuring the fluctuations of the electromagnetic shower and the second term is the constant term, which measures linearity.

Finally, let one look at the last, outermost part of the ATLAS detector, the muon chambers. The time resolution is important for the trigger chambers, while the position accuracy is more relevant for precision chambers. The RPC has a 10 mm accuracy in z and ϕ with a 1.5 ns time resolution and the TGS, in the forward region, reaches 2-6 mm in z, 3-7 mm in ϕ and 4 ns time resolution. On the other hand, the precision of CSC chambers has a 40 μm z accuracy, a 5 mm ϕ accuracy and a 7 ns time resolution, while the MDT reaches an average resolution of 3 μm per chamber.

The second part of commissioning concerns the physical objects one would like to reconstruct. Using the data from the different subdetectors, five types of objects are of interest for physics: low-p_T charged particles, photons, electrons, jets and muons. Detailed description of their reconstruction methods could be found in [17]. The first type of objects is measured by the track they leave in the inner detector without escaping it. The second and the third, being electromagnetic objects, are identified by their energy deposit (cluster) in the electromagnetic calorimeter. In the case where a track is matched to this cluster, the object is an electron. If not, the cluster is identified as a photon.

As well known, a jet is the experimental signature of a quark or a gluon in the final state of the primary interaction. Jets are detected by the energy they leave in the hadronic

calorimeter. The last objects, muons, are identified by a track in the muon chambers matched to a track in the inner detector.

Moreover, performance benchmarks need to be established in order to trigger on all the physical objects described above. This is particularly important since the trigger decision online is irreversible and it needs to be efficient in order not to miss any interesting physics events.

Chapter 3

Introduction to Extra Dimensions

The possibility that Universe has more than three spatial dimensions has been attracting continuing interest for many years. Strong motivation for considering space as multi-dimensional comes from theories which incorporate gravity in a reliable manner, string theory and M-theory. An important issue in extra-dimensional theories is the mechanism by which extra dimensions are hidden, so that space-time is effectively four-dimensional. In recent years, new extra-dimensional theories have been developed. Lowering the string scale in the TeV region provides a theoretical framework for solving the mass hierarchy problem and unifying all interactions. Moreover, this new phenomenological ideas lead to relating the physics of extra dimensions to observables in a variety of physics experiments.

The purpose of this Chapter is to introduce the framework of these extra-dimensional theories. The big advantage of these models is that their phenomenological consequences might be observable at today's particle colliders, whether, for example, the deviation of Newton's law at small distances, the graviton production in particle processes or the possibility to create microscopic black holes. The last example will be discussed in detail in next Chapter 4.

3.1 Three Dimensions ... Enough or Not?

3.1.1 Minkowski's idea

The idea that the Universe has more than three dimensions has been suggested a long time ago. It goes back to 1860s when Bernhard Riemann introduced in his Habilitation lecture [24] the concept of what is now known as the Riemannian space and curvature tensor.

The new coordinates of extra dimensions need not necessarily be lengthlike or space-like. As Hermann Minkowski showed in his paper "Raum und Zeit" in 1909 [25], the successes of Maxwell's unified electromagnetic theory and Einstein's Special relativity could be understood geometrically if time, along with space, were considered part of a four-dimensional spacetime manifold. It is worth noting that the modern physics would be unimaginable without the notion of spacetime (for example, the General relativity).

Minkowski first presented[1] his views on relativity at the annual meeting of the German Society of Natural Scientists and Physicians in Köln in September 21, 1908. The opening passage of the talk was a rather dramatic proclamation [25]:

> *"Gentlemen! The conceptions of space and time which I would like to develop before you arise form the soil of experimental physics. Therein lies their strength. Their tendency is radical. Henceforth, space by itself, and time by itself, are doomed to fade away in the shadows, and only a kind of union of the two will preserve an independent reality."*

In the closing passage he concluded:

> *"The validity without exception of the world-postulate, I would like to think, is the true nucleus of an electromagnetic image of the world, which, discovered by Lorentz, and further revealed by Einstein, now lies open in the full light of day."*

These two passages have helped consolidate the image of Minkowski's geometrically motivated approach to relativity and of his alleged commitment to the electromagnetic view of nature.

An interesting historical note is that it was Henry Poincaré who first realized (before July 1905) that the Lorentz transformations have a natural geometric interpretation as rotations in a four-dimensional space whose fourth dimension is time. The question why Poincaré did not develop further this revolutionary idea is still unanswered. However, it seems that the most probable explanation might be his *conventionalism*[2]. Poincaré thought that this idea of a mathematical four-dimensional space would not necessarily force one to assume that the world itself is also four-dimensional. That could be the reason why he had seen nothing revolutionary in this idea.

Going back to 1914, Gunnar Nordström proposed the observed world to be an effective theory of a fundamental theory existing in more than four dimensions. Without General relativity at that time, he wrote down Maxwell's equations in five dimensional spacetime. He reduced the equations to Maxwell-Nordström electromagnetic-gravitational theory in four dimensions by wrapping the fifth dimension on a circle.

Later, in 1918, Hermann Weyl introduced the concept of gauge invariance in the first attempt to unify electromagnetism and gravitation in a geometric context. As, on the 1st of March 1918, he wrote to Einstein [26]: *"These days I succeeded, as I believe, to derive electricity and gravitation from a common source ..."*.

Einstein admired Weyl's theory as *"... a coup of genius of the first rate ..."*, but immediately realized that it was physically untenable: *"Although your idea is so beautiful, I have to declare frankly that, in my opinion, it is impossible that the theory corresponds to nature."*[3]

---

[1]His lecture was later published as "Raum und Zeit" [25].

[2]"He believed that our physical theories are nothing more than convenient descriptions of the world and therefore it is really a matter of convenience which theory one would use in a given situation." [25]

[3]More details on Weyl's attempt to unify gravitation and electromagnetism, early history of gauge

3.1.2   Kaluza-Klein Theory

Independently on Nordström and inspired by the Weyl's work, Theodor Kaluza proposed another geometrical unification of gravitation and electromagnetism. Einstein reacted positively. On 21 April 1919 he wrote [26]: "*The idea of achieving [a unified theory] by means of a five-dimensional cylinder world never dawned on me ... . At first glance I like your idea enormously*". And later he added: "*The formal unity of your theory is startling*".

However, in his theory the matter part was studied only in a non-relativistic approximation and the five-dimensional geodesic equation was only written on this limit. Kaluza was aware of this limitations and as he noted [26]:

> "*In spite of all the physical and theoretical difficulties which are encountered in the above proposal it is hard to believe that the derived relationships, which could hardly be surpassed at the formal level, represent nothing more than a malicious coincidence. Should it sometimes be established that the scheme is more that an empty formalism this would signify a new triumph for Einstein's General Theory of Relativity, whose suitable extension to five dimensions is our present concern.*"

Oskar Klein tried to explain the apparently unobserved nature of the extra dimension. He assumed it is rolled up to a small size and periodic with period $2\pi\lambda_5$, where λ_5 is the scale of the fifth dimension given as

$$\lambda_5 = 0.8 \times 10^{-30} \text{ cm.} \tag{3.1}$$

And as Oskar Klein noted [13]

> "*The small value of this length together with the periodicity in the fifth dimension may perhaps be taken as a support of the theory of Kaluza in the sense that they may explain the non-appearance of the fifth dimension in ordinary experiments as the result of averaging over the fifth dimension.*"

Einstein and others physicists tried to find[4] a non-singular charged object in the classical Kaluza-Klein theory. Finally, one can read in their joint paper [13] that this search had become frustrated:

> "*It seems impossible to describe particles by non-singular solutions of the field equations. As no arbitrary constants occur in the equations, the theory would lead to electro-magnetic and gravitational fields of the same order of magnitude. Therefore one would be unable to explain the empirical fact that the electrostatic force between two particles is so much stronger than the gravitational force. This means that a consistent theory of matter could not be based on these equations.*"

---

theories and the correspondence between Weyl, Einstein and other leading physicists could be found in [26], [27] and in referencies therein.

[4]Details could be found in [13].
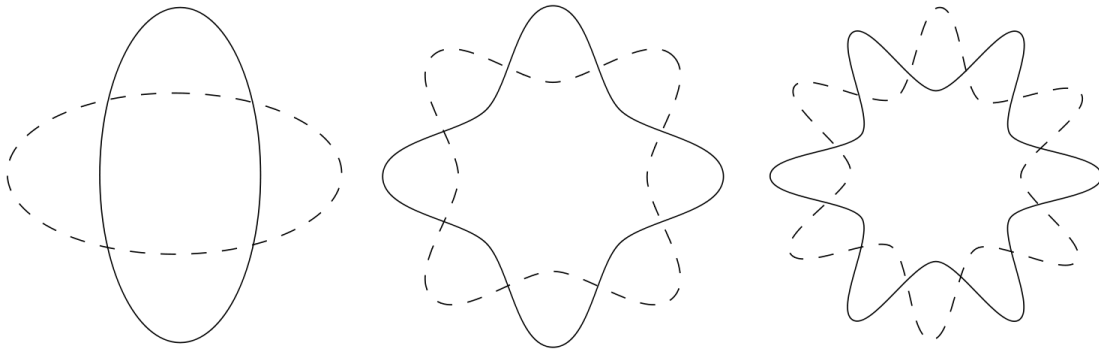
Figure 3.1: Different particles as a different vibrational modes of a string [29].

Einstein did not succeed, which is probably one of the primary reasons why he abandoned working on this theory. In 1943 he argued, together with Pauli, that in Kaluza's theory it would be principally impossible to find a non-singular particle. Einstein never worked in five dimensions again and the Kaluza-Klein theory remained in the background of particle physics.

3.1.3 $3 + 1 + 6 = 10$ ... Strings

Moving now to the late 1960s, physicists would like to understand the strong nuclear force. The basic idea using the strings to describe strong interactions is that specific particles correspond to specific oscillation modes, or quantum states, of the string, as it is shown in Fig. 3.1. However, this string-based description of the strong force made many predictions that directly contradicted experimental findings. The scientific community lost interest in string theory as a theory of strong interactions in 1974 when quantum chromodynamics became the main focus of theoretical research.

Few years later, the string theory turned back on desks. It turned out to be well suited for an ambitious purpose: the construction of a quantum theory that unifies the description of gravity and the other fundamental forces of nature.

The theory is only consistent in a ten-dimensional space-time and in some cases an eleventh dimension is also possible. Where are these six or seven extra spatial dimensions hidden? How is it possible that one is not able to see them?

In the string theory, similarly as in Kaluza-Klein theory, the essence of this beautiful approach reappears. The Kaluza–Klein idea, nowadays referred to as compactification, can be illustrated in terms of the two cylinders shown on Fig. 3.2.

The surface of the first cylinder is two-dimensional. However, if the radius of the circle becomes extremely small, or equivalently if the cylinder is viewed from a large distance, the cylinder looks effectively one-dimensional. One now imagines that the long dimension of the cylinder is replaced by known four-dimensional space-time and the short dimension by an appropriate six, or seven-dimensional compact manifold. At large distances or low

Figure 3.2: From far away a two-dimensional cylinder looks one-dimensional [29].

energies the compact internal space cannot be seen and the world looks effectively four-dimensional.

In principle, the string theory has the potential to provide a complete understanding of particle physics and cosmology. It is clear this is still a distant dream but in this fascinating theory surprises arise over and over. For more information about string theory and living in ten or eleven-dimensional Universe see [28] or [29].

3.1.4 From Small to Large ... Warped ... or Infinite

String idea seems to be an elegant tool to describe the whole Universe and also to unify common fundamental forces. Nowadays, this idea is still only an elegant *theoretical* tool and it is clear that in the near future it will rest *experimentally* untouchable.

It results from the size of a string and so from the size of hidden extra dimensions and the possibility to observe them. The natural first guess for a rough estimate of the fundamental string length scale (and so of the characteristic size of compact extra dimensions too) represents the Planck scale. The Planck length is given by

$$l_{Pl} = \left(\frac{\hbar G}{c^3} \right)^{1/2} = 1.6 \times 10^{-33} \text{ cm} \tag{3.2}$$

and the Planck mass is defined as

$$m_{Pl} = \left(\frac{\hbar c}{G} \right)^{1/2} = 1.2 \times 10^{19} \text{ GeV}, \tag{3.3}$$

where $\hbar$ is the Planck's constant divided by 2π, G is Newton's gravitational constant, and c the speed of light. One could clearly see that the energy 10^{19} GeV needed to observe these hidden extra dimensions is out of today's and near future's particles accelerators. The Large Hadron Collider would have "only" $\sim 10^4$ GeV.

It seems that the idea of extra-dimensional world would not be experimentally tested and confirmed at all. It was not until 1998 that the idea of extra dimensions in space has

been used as a possible solution of one of the most embarrassing problems of the Standard Model of particle physics – the hierarchy problem.

3.1.5 Models with Extra Dimensions

By this year (1998) another extra-dimensional scenarios have appeared. One of these scenarios supposes *large* extra dimensions (described in the Section 3.2), where "large"[5] means the size of order of ~ 1 mm to ~ 1 fm. In another case, the extra dimension is not flat or at least weakly curved, but strongly curved (or warped) by a large negative cosmological constant[6] (see Section 3.3). The observed weakness of gravity is thus due to the gravitational field being allowed to expand into the higher-dimensional space (bulk), while the Standard Model particles are confined to the familiar three-dimensional space (3-brane).

The next one, the model of universal extra dimensions (see Section 3.4) supposes that all particles (or in some extensions only gauge fields) can propagate in the whole higher-dimensional spacetime. These extra dimensions typically have radii of $\sim 10^{-18}$ m and they are compactified on an orbifold. These models come closest to the original idea of Kaluza and Klein.

Other scenarios have appeared as well, for example, the so-called split fermion model. This is not exactly a model on its own, but it serves as a quick fix for some problems that arise within models with a lowered fundamental scale. For example, the proton to decay and other contributions in the Standard Model are usually suppressed by the large value of the Planck scale. If the Planck scale is lowered they could become quite troublesome and it would allow the proton to decay rather fast [30], [31].

The big experimental challenge for these scenarios is that the TeV energy scale is sufficient to prove them. So, nowadays, it looks like one could experimentally "see" these extra dimensions. In other words, one may observe some of their consequences such as production of some new particles, microscopic black holes, etc., which will be tested at the Large Hadron Collider.

Of course, there might be a great danger of getting lost in pure speculations. Like in the first unification proposal of Hermann Weyl, they may create beautiful and highly relevant mathematics which does, unfortunately, not describe nature. However, in the latter case, history shows that such ideas could one day also become fruitful for physics.

3.2 Large Extra Dimensions

In 1998, Nima Arkani-Hamed, Savas Dimopoulos and Gia Dvali (ADD) proposed a new framework for solving the hierarchy problem [32], [33], [34]. In this framework the gravitational and gauge interactions become unified at the weak scale, which is taken as the

---

[5]comparing to the Planck length given in eq. (3.2)

[6]This type of space is known in the literature as an anti-de Sitter (AdS) space, since de Sitter studied the Universe with a positive cosmological constant.

only fundamental short distance scale in nature. The ADD model explains the observed weakness of gravity on distances $\gtrsim 1$ mm by assuming the existence of $n \geq 2$ new compact extra spatial dimensions large compared to the weak scale. As Arkani-Hamed said [35]:

> *"These ideas came very, very quickly. We did some very simple estimates and realized that the size of these extra dimensions would have to be huge compared to the size people had been talking about - maybe as large as a millimeter, in the case of two extra dimensions. But we couldn't immediately find any contradiction with having this crazy idea. This was all in the course of an afternoon, and I think we all thought this was crazy and very amusing but surely there must be something wrong with it. The remarkable thing was that the more we thought about it, and the more different ways we tried to kill it off, we couldn't do it. It survived and was consistent in a pretty non-trivial way with all the experimental results we could imagine. So after four or five months of trying to kill it off every day, we started to become convinced that it wasn't kill-off-able and was a viable idea."*

The ADD model assumptions are the following:

- n extra dimensions, each compactified with radius r (taken to be the same size for each dimension) on a torus with volume $V_{(n)} = (2\pi r)^n$;

- All Standard Model (SM) fields (matter, Higgs, gauge fields) localized to a 3-brane ("SM brane") in the bulk ("gravity only") spacetime;

- Bulk and boundary spacetime is flat, i.e., the bulk and boundary cosmological constants vanish;

- The SM 3-brane is "stiff"; the fluctuations of the brane surface itself in the higher dimensional spacetime can be ignored (or, more technically, the brane fluctuations have masses of order of the cut-off scale).

The important questions that one would like to answer are: what is the relation between four-dimensional, M_{Pl}, and the fundamental (higher-dimensional), M_*, Planck scale of the theory and how large the extra dimensions could possibly be? There exist three main methods of derivation of the relation between M_{Pl} and M_*: Gauss law, Kaluza-Klein method and action method. The first two methods could be found in [82], the third one will be briefly introduced in the following.

3.2.1 Relating Plank Scales

Before one writes down the action for the higher-dimensional gravitational theory, including the dimensionful constants, it could be very useful to examine the mass dimensions of the various quantities that will appear. First, look at the infinitesimal distance, which is related to the coordinates and the metric tensor by

$$ds^2 = g_{MN}dx^M dx^N, \tag{3.4}$$

where the used sign convention for the metric is $(+, -, -, \ldots, -)$. If one assumes that the coordinates carry proper dimension[7] the metric tensor is dimensionless, $[g] = 0$. Looking at the Christoffel symbols which could be calculated as

$$\Gamma^A_{MN} \sim g^{AB} \partial_M g_{NB}, \tag{3.5}$$

one could get that the Christoffel symbols carry dimension one, $[\Gamma] = 1$. Finally, since $R_{MN} \sim \Gamma^2$, the Ricci tensor will carry dimension two, $[R_{MN}] = 2$, and similarly the curvature scalar R, $[R] = 2$. The main point is that all of this is independent on the total number of dimensions.

With assumption that the Einstein-Hilbert action will take the same form as in four dimensions, one could generalize this action to more than four dimensions as

$$S_{4+n} \sim \int d^{4+n} x \sqrt{g^{(4+n)}} R^{(4+n)}. \tag{3.6}$$

The action (3.6) is not dimensionless. To be so, one needs to multiply by the appropriate power of the fundamental Planck scale M_*. Since $R^{(4+n)}$ carries dimension 2 and $d^{4+n}x$ carries dimension $-n - 4$, this has to be the power $n + 2$, thus

$$S_{4+n} = -M_*^{n+2} \int d^{4+n} x \sqrt{g^{(4+n)}} R^{(4+n)}. \tag{3.7}$$

The problem is to find out how the usual four-dimensional action

$$S_4 = -M_{Pl}^2 \int d^4 x \sqrt{g^{(4)}} R^{(4)} \tag{3.8}$$

is contained in higher-dimensional expression (3.7). Using the assumptions of the ADD model above mentioned (the spacetime is flat and n extra dimensions are compact) the n-dimensional metric is given by

$$ds^2 = (\eta_{\mu\nu} + h_{\mu\nu}) \, dx^\mu dx^\nu - r^2 d\Omega^2_{(n)}, \tag{3.9}$$

where x_μ is four-dimensional coordinate, $d\Omega^2_{(n)}$ corresponds to the line element of the flat extra dimensional space in some parametrization, $\eta_{\mu\nu}$ is the flat (Minkowski) 4D metric, and $h_{\mu\nu}$ is the 4D fluctuation of the metric around its minimum. From this one could get [82], [83]

$$\sqrt{g^{(4+n)}} = r^n \sqrt{g^{(4)}}, \qquad R^{(4+n)} = R^{(4)}, \tag{3.10}$$

and therefore

$$S_{4+n} = -M_*^{n+2} \int d^{4+n} x \sqrt{g^{(4+n)}} R^{(4+n)} = -M_*^{n+2} \int d\Omega_{(n)} r^n \int d^4 x \sqrt{g^{(4)}} R^{(4)}. \tag{3.11}$$

---

[7]it means they are not angular variables

The factor $\int d\Omega_{(n)} r^n$ is nothing but the volume of the extra dimensional space, $V_{(n)}$, and for the case of toroidal compactification it would simply be given by $V_{(n)} = (2\pi r)^n$. Therefore the above action (3.11) takes the form

$$S_{4+n} = -M_*^{n+2} V_{(n)} \int d^4x \sqrt{g^{(4)}} R^{(4)}. \tag{3.12}$$

Now, comparing (3.8) with (3.12) one could finally find the matching relation for the gravitational couplings that one have looked for:

$$M_{Pl}^2 = M_*^{n+2} V_{(n)} = M_*^{n+2} (2\pi r)^n. \tag{3.13}$$

Repeating the same matching procedure for the gauge couplings, one gets the relation [83]:

$$\frac{1}{g_4^2} = \frac{V_{(n)}}{g_*^2}. \tag{3.14}$$

3.2.2 Size of Extra Dimensions

A crucial issue in extra-dimensional theories is the mechanism by which extra dimensions are hidden, so that the spacetime effectively looks like a four-dimensional one. One of the possible ways to "hide" these extra dimensions is by assuming that they are finite and compact, which is the case of the ADD model. The smaller the size of extra dimensions is the bigger energy is needed to "see" them. Another way could be, for example, an assumption that extra dimensions are warped, which is presented in Randall-Sundrum model introduced in the Section 3.3.

Now let one try to understand the consequences of (3.13) and (3.14). From (3.14) it could be seen that the gauge coupling in extra dimensions is dimensionful, $[g_*] = -n/2$, and one needs to ask what should be its natural size. With assumption that the same physics that sets the strength of gravitational couplings would also set the gauge coupling, then

$$g_* \sim \frac{1}{M_*^{\frac{n}{2}}}. \tag{3.15}$$

Therefore, one would have the following two equations:

$$\frac{1}{g_4^2} = V_{(n)} M_*^n \sim r^n M_*^n, \tag{3.16}$$

$$M_{Pl}^2 = V_{(n)} M_*^{n+2} \sim r^n M_*^{n+2}, \tag{3.17}$$

from which it follows that

$$r \sim \frac{1}{M_{Pl}} g_4^{\frac{n+2}{n}}. \tag{3.18}$$

From (3.18) it simply implies that in a "natural" higher-dimensional theory $r \sim 1/M_{Pl}$!
And because of the huge value of the Planck scale, there would be no hope of finding out
about the existence of these tiny extra dimensions in the foreseeable future.

All these arguments crucially depend on the assumption that every field propagates in
all dimensions. However, in the ADD model only gravity propagate in the extra dimensions,
whereas Standard Model (SM) fields "live" on the SM brane. If one takes a look at the
experimental bounds on the size of an extra dimension, for example, at deviation from
Newtonian gravity described further, one gets

$$r \leq 0.1 \text{ mm}. \tag{3.19}$$

There exist bounds on the fundamental Planck scale M_* as well. If $M_* < 1$ TeV, quantum
gravity should have already played a role in today's or previous collider experiments. Since
no such hint has appeared, one has to impose that $M_* > 1$ TeV. Therefore, the lowest
possible value of M_* would be $M_* \sim 1$ TeV.

Taking M_* of order of a TeV and reversing the expression (3.13) one would get

$$\frac{1}{r} = M_* \left(\frac{M_*}{M_{Pl}} \right)^{\frac{2}{n}} = (1 \text{ TeV}) 10^{-\frac{32}{n}}, \tag{3.20}$$

where $M_* \sim 10^3$ GeV and $M_{Pl} \sim 10^{19}$ GeV. Using the conversion factor $1 \text{ GeV}^{-1} = 2 \cdot 10^{-14}$ cm, one would obtain from (3.20)

$$r \sim 2 \cdot 10^{-17} 10^{\frac{32}{n}} \text{ cm}. \tag{3.21}$$

One could clearly see from (3.21) why there was the assumption of $n \geq 2$ extra dimensions.
For $n = 1$, one would get the absurdly large value of $r = 2 \cdot 10^{15}$ cm, which is greater than
the astronomical unit $(1.5 \cdot 10^{13}$ cm). However, for two extra spatial dimensions their size
is just of order of ~ 1 mm, for $n = 3$ it is ~ 1 nm and for seven extra spatial dimensions
their size is ~ 1 fm.

3.2.3 Confronting with Experiments/Observations

In the following, some of the most interesting constraints on the ADD model will be briefly
introduced. The main ones come from:

- Newton's law: One has to expect the influence of the extra dimensions on high
  precision measurements; the most obvious being the modification of Newton's law at
  small distances;

- Cosmology and astrophysics: Modification of inflation in the early Universe and
  enhanced supernova-cooling due to graviton emission;

- Additional processes are expected in high-energetic lepton and hadron interactions:
  Production of real and virtual gravitons and the creation of microscopic black holes
  at energies that can be achieved at colliders and in ultra high energetic cosmic rays.

Deviation from Newtonian Gravity

The Newtonian potential between two bodies of masses m_1 and m_2 is given by

$$V\left(r'\right) = \begin{cases} -G_N^{(4+n)} \frac{m_1 m_2}{r'^{1+n}} & r' < r \\ \\ -G_N \frac{m_1 m_2}{r'} & r' > r \end{cases}, \tag{3.22}$$

where r' represents the distance separating the object, not to be confused with the size of the extra dimension, r. A question one would like to answer is how well gravity is measured? Since gravity is really weak at short distances in comparison to the other forces, the answer is rather poor. There have been ideas on the potential modification of gravity at small but macroscopic distances and experimentalists simplified all this by parametrizing deviations in Newton's law as

$$V\left(r'\right) = -G_N^{(4)} \frac{m_1 m_2}{r} \left(1 + \alpha e^{-r'/\lambda}\right), \tag{3.23}$$

where α is the strength of the Yukawa interaction relative to gravity, and λ is a length scale or range. The Yukawa form of the correction to Newton's law roughly corresponds to the exchange of virtual bosons of the mass $m_b = \hbar/(\lambda c)$.

Fig. 3.3 shows how well gravity is tested at macroscopic distances of direct relevance to the ADD model. One could see from Fig. 3.3 there are five experimental results plotted (Lamoreaux, Stanford, Colorado, Eöt-Wash, and Irvine) which provide the strongest constraint on deviations from Newton's law for various ranges of distances and strengths of forces. The strongest constraint relevant to models of extra dimensions comes from the Eöt-Wash experiment that is consistent with Newtonian gravity down to about 200 microns [36].

For two extra dimensions, the predicted deviation from Newtonian gravity occurs at $r \sim 1$ mm. When ADD published the first paper on their model, the best experimental limit on gravitational strength forces happened also to be at about 1 mm. Until now, there have not been found any deviation down to 100 microns [38] so that two extra dimensions with a quantum gravity scale of $M_* = 1$ TeV are ruled out. If one takes three or more extra dimensions, the predicted deviation from Newtonian gravity occurs at distances smaller than ten nanometres. Fig. 3.4 shows the experimental results on new forces at these distances and one could clearly see that these constrains are extremely weak. The good news is that ADD model with $M_* = 1$ TeV and $n \geq 3$ is not excluded by these experiments, the bad news is that today's experiments are so far from testing these strength interactions directly.

Astrophysical Constraints

The effects of Kaluza-Klein (KK) graviton emission could be studied in hot stars such as the Sun, red giants or supernovae such as SN1987A [34], [39], [40]. The various processes involving emission of the KK graviton (G) are:
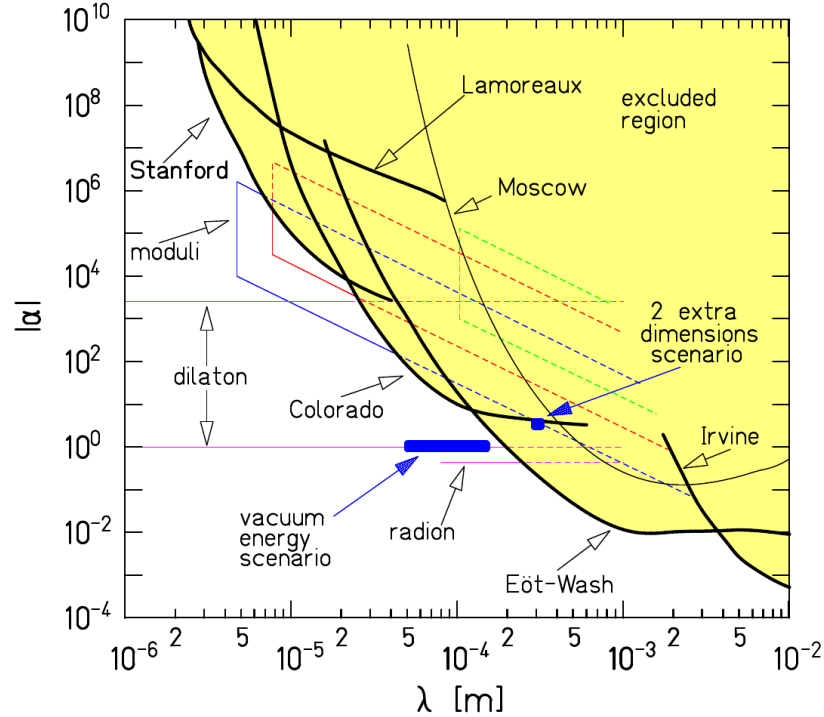
Figure 3.3: 95%-confidence-level constraints on ISL-violating Yukawa interactions with $1~\mu$m $< \lambda < 1$ cm. The heavy curves give experimental upper limits [37].

- Photon-photon annihilation, $\gamma\gamma \to G$

- Electron-positron annihilation, $e^-e^+ \to G$

- Gravi-Compton-Primakoff scattering, $e^-\gamma \to e^-G$

- Gravi-bremsstrahlung in a static electric field, $e^-(Ze) \to e^-(Ze)G$

- Nucleon-nucleon bremsstrahlung, $NN \to NNG$

The temperature of the Sun is ~ 1 keV, and the relevant particles in equilibrium are electrons, protons and photons. The number of densities n_e, n_p and n_γ are roughly comparable, $n_{e,p,\gamma} \sim (\text{keV})^3$. The most important process is photon pair fusion into graviton. This process places a lower bound on $M_{(4+n)}$ as [34]

$$M_{(4+n)} \gtrsim 10^{\frac{18-6n}{n+2}}~\text{GeV}. \tag{3.24}$$

For $n = 2$, one could obtain a bound $M_{(6)} \gtrsim 30$ GeV. Other processes are less important because some of them are suppressed relative to the photon-photon fusion (for example the Gravi-Primakoff process or the Gravi-Compton scattering) and the others are irrelevant since there are no high-Z nuclei present in the Sun (the Gravi-brehmstrahlung process) or
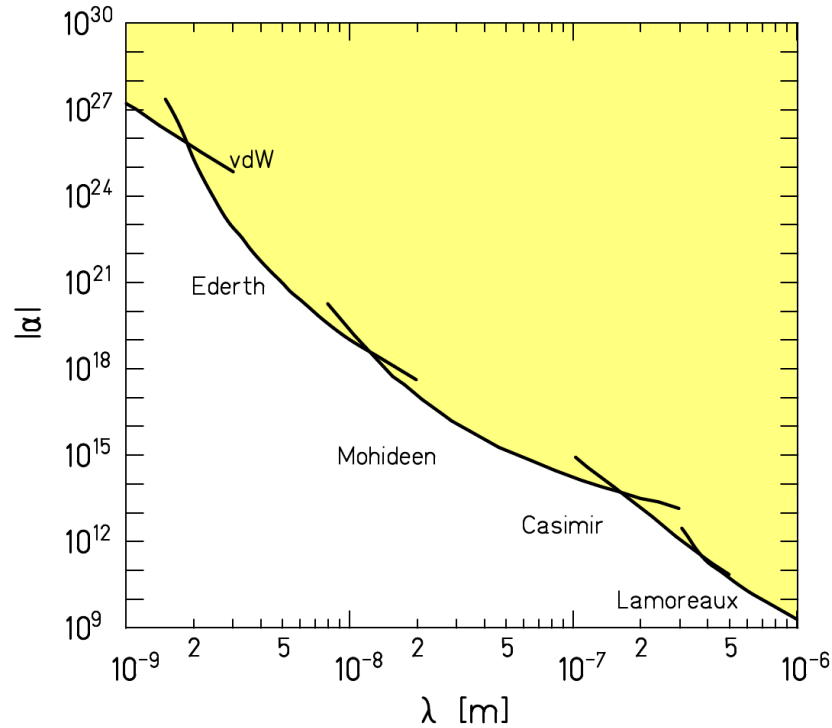
Figure 3.4: Constraints on ISL-violating Yukawa interactions with 1 nm $< \lambda <$ 1 μm [37].

because at these temperatures the collisions of nucleons cannot probe the strong interaction core (the nucleon-nucleon brehmstrahlung process).

For red giants, whose temperature is of $T \sim 10$ keV, the constraints are a bit different, but the temperature is still so low that $M_{(4+n)} \sim 1$ TeV is still safe for all n.

Clearly the strongest bounds come from SN1987A, where the temperature is significantly higher, $T \sim 30$ MeV. SN1987A is the titanic supernova, shown on Fig. 3.5, blazed with the power of 100 million Suns for several months following its discovery on Feb. 23, 1987. There are two dominant processes: the nucleon-nucleon brehmstrahlung and the Gravi-Primakoff process.

The bound on $M_{(4+n)}$ from the nucleon-nucleon brehmstrahlung is given by [34]

$$M_{(4+n)} \sim 10^{\frac{15-4.5n}{n+2}} \text{ TeV.} \qquad (3.25)$$

For $n = 2$, one could see from (3.25) that this strong bound requires $M_{(6)} \gtrsim 30$ TeV [34] or $M_{(6)} \gtrsim 50$ TeV [40]. The bound which follows from the Gravi-Primakoff process is given by

$$M_{(4+n)} \gtrsim 10^{\frac{12-4.5n}{n+2}} \text{ TeV.} \qquad (3.26)$$

Comparing eq. (3.25) and (3.26) one could see that the further bound is weaker. The reason is that while again in the supernovae, nucleon and photon abundances are comparable, the nucleon-nucleon brehmstrahlung cross-section is enhanced by strong-interaction effects [34].
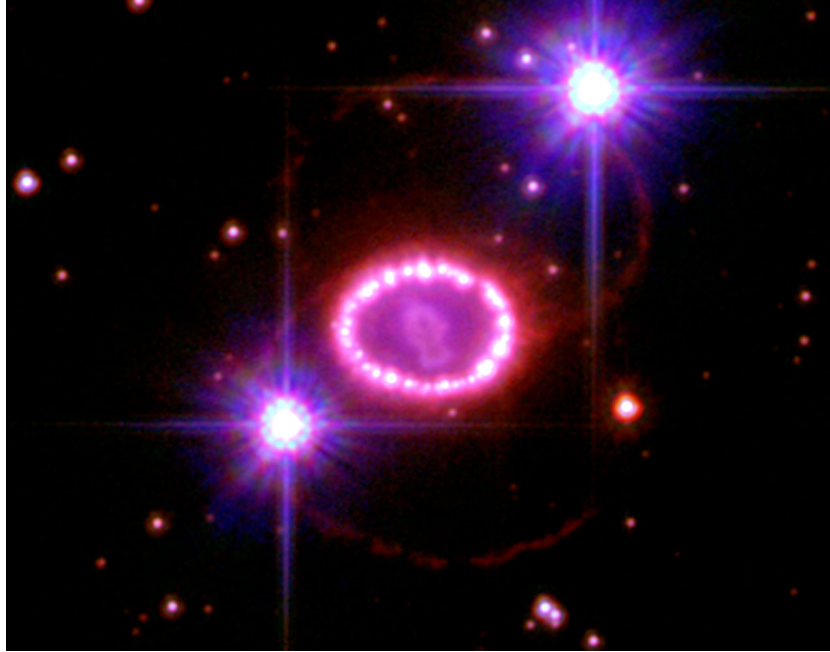
Figure 3.5: SN1987A: A string of 'Cosmic pearls' surrounds an exploding star. A shock wave of material unleashed by the stellar blast is slamming into regions along the ring's inner regions, heating them up, and causing them to glow. The ring, about a light-year across, was probably shed by the star about 20,000 years before it exploded. [41].

The graviton emission from SN1987A puts very strong constraints on models with large extra dimensions in the case $n = 2$. The correspond radius of a bound on the fundamental Planck scale is of order of $\sim 10^{-1}$ μm. For the case of $n > 2$ one does not get a significant bound on M_* from this processes.

Cosmological Implications

Now take a look at the cooling of another big astrophysical system: the entire Universe. The source of the cooling is the same as for supernovae - the graviton emission.

Large extra dimensions offer new ways of understanding the Universe. There exist new scenarios of inflation and baryogenesis within the braneworld context. Inflation on "our brane" can be obtained if another brane falls on top of "our brane" in the early period of development of the Brane Universe [42]. Baryon asymmetry of a desired magnitude can also be produced during the collision of these two branes. Within this non-equilibrium collision baryon number can be transported from one brane to another one. This results in the baryon number excess in our Universe which exactly equals to the hidden "baryon number" deficit in the other Brane Universe. [43]. For more recent developments see Refs. [45], [46], [47].

The decay rate for a graviton into two photons is given as

$$\Gamma_{G \to \gamma\gamma} = \frac{m_G^3}{80\pi M_{Pl}^2}, \tag{3.27}$$

which correspond to a decay time of

$$\tau \sim (10^8 \text{Gyr}) \left(\frac{\text{MeV}}{m_G} \right)^3, \tag{3.28}$$

where m_G is mass of graviton[8]. Hence, once a graviton is produced it decouples from the thermal plasma and does not decay for a long, long time.

To obtain a bound on models within large extra dimension, one has to compare the ordinary Hubble expansion rate to that of cooling by gravitons. These two cooling rates are given respectively by

$$\left. \frac{d\rho}{dt} \right|_{expansion} \sim -3H\rho \sim -3\frac{T^2}{M_{Pl}^2}\rho, \tag{3.29}$$

$$\left. \frac{d\rho}{dt} \right|_{evaporation} \sim \frac{T^n}{M_*^{n+2}}, \tag{3.30}$$

where H is the Hubble constant given as $H = 2.29 \times 10^{-18}$ s^{-1}. These two rates are equal at the so called "normalcy temperature" T_*, which could be easily found by equating the above rates.

$$T_* \sim \left(\frac{M_*^{n+2}}{M_{Pl}} \right)^{\frac{1}{n+1}} = 10^{\frac{6n-9}{n+1}} \text{ MeV}. \tag{3.31}$$

Below this temperature the Universe would expand as a normal four-dimensional Universe. With various number of extra dimension n normalcy temperature T_* goes from ~ 10 MeV ($n = 2$) to ~ 100 GeV ($n = 6$).

The normalcy temperature represents the maximum reheat temperature of the Universe such that cooling by ordinary Hubble expansion dominates. There are two things to note. The good one is that this temperature is above the temperature of big bang nucleosynthesis (BBN), which is about 1 MeV, so there is no need to expect BBN predictions to be modified. The bad one is that it has been generally thought that the Universe was far hotter than tens of MeV to tens of GeV. So, all of phenomena such as dark matter, baryogenesis, inflation, etc. need new mechanisms that operate at low temperatures. For more details see Ref. [48].

Virtual Graviton Exchange and Real Production in Colliders

The existence of the extra dimensions implies the direct or virtual emission of gravitons by Standard Model (SM) particles. Virtual graviton exchange may generate numerous higher dimension operators, contributing to the production of SM particles [49]-[52].

---

[8]The current limits on graviton mass could be found in [44].

Theories with large extra dimensions involve the production of a single graviton mode. Since the lifetime of an individual graviton mode is of order $\Gamma \sim \frac{m_G^3}{M_{Pl}^2}$, which means that each graviton produced is extremely long lived, and once produced it will not decay again within the detector. Therefore, it is like a stable particle which would provide missing energy signals. Gravitons are produced directly in association with photons or jets through the processes:

- $e^+e^- \rightarrow \gamma G$,

- $q\bar{q} \rightarrow \gamma G$,

- $q\bar{q} \rightarrow gG$, $qg \rightarrow qG$, and $gg \rightarrow gG$.

Data from four LEP (Large Electron Positron collider) experiments, ALEPH, DELPHI, L3 and OPAL, have been used to search for extra spatial dimensions [54], [55]. The search for virtual graviton exchange was performed using many different event topologies where the highest sensitivity was obtained using Bhabha events. Since no signs of a signal were observed, the strongest limits on M_{BH} were set as $M_{BH} > 1.20$ TeV. The process of graviton production together with a photon was searched for using events where only a single photon was detected in the experiment.

Fig. 3.6 shows the distribution of the photon energy (divided by the beam energy) from the combined single photon sample selected by DELPHI and L3 together with the predicted graviton signal for a value of $M_D = 1$ TeV[9] and $n = 2$. Since, as one could see, there are no signs of a signal in any of the LEP experiments, these results were used to derive M_D exclusion limits for different numbers of extra dimensions. The obtained M_D limits, as the combined results from ALEPH, DELPHI and L3, are shown in Fig. 3.7. The limits for the number of extra dimensions are between two and six. The present limits from Tevatron experiments D0 and CDF are also shown in this Figure.

At the Tevatron, the graviton can be produced in $q\bar{q} \rightarrow gG$, $qg \rightarrow qG$ or $g \rightarrow gG$ processes corresponding to a jet $+ E_T$ final state, and in $q\bar{q} \rightarrow \gamma G$ corresponding to a $\gamma + E_T$ detector signature. Graviton exchange can be studied in a range of $2 \rightarrow 2$ processes with the best sensitivity in final states with two leptons, photons, or Z bosons [56], [57].

The constraints on the large extra dimensions model are summarized in Tab. 3.1. The sensitivity of large extra dimensions at the Tevatron is comparable to or better than that from the LEP experiments.

The leading experimental signal of graviton production at the Large Hadron Collider (LHC) is $pp \rightarrow$ jet $+ E_T$ coming from the subprocess $qg \rightarrow qG$, $q\bar{q} \rightarrow gG$, and $gg \rightarrow gG$ [51], [53]. The main background comes from processes with a Z boson and one jet in the final state, with the Z decaying into neutrinos.

The subprocess $q\bar{q} \rightarrow G\gamma$ with a photon and missing energy in the final state represents another signal for graviton production. The main background comes from $q\bar{q} \rightarrow Z\gamma$ events. There is, however, a disadvantage of the photon signal over the jet signal which is that the

---

[9]M_D means the same as M_* and it is used in the following only by reason of Fig. 3.6 and Fig. 3.7.
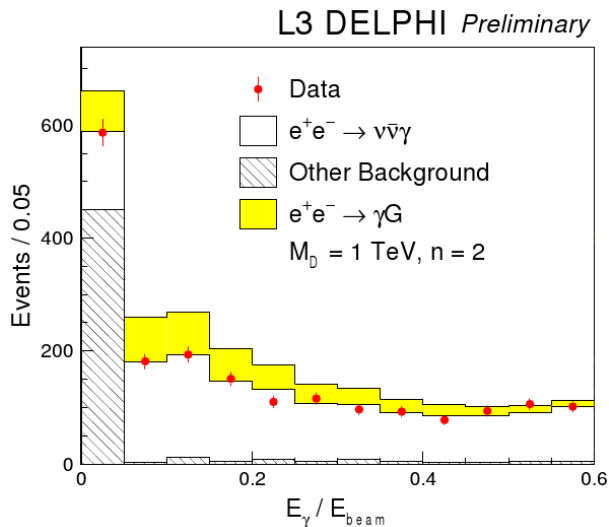
Figure 3.6: Distribution of the ratio of the photon energy to the beam energy for single photon events selected by DELPHI and L3, together with the Standard Model prediction. Expected signal from graviton emission is also shown for $M_D = 1$ TeV and $n = 2$ [54].
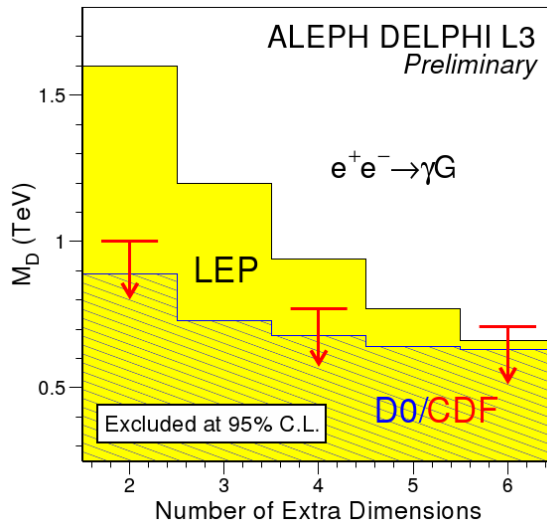
Figure 3.7: The combined ADL M_D limits at 95% CL as a function of n. The current limits from the D0 (hatched area) and CDF (indicated by arrows for $n = 2$, 4 and 6.) experiments are also shown [54].

photon signal is the much lower rate. This is caused by the smallness of the electromagnetic coupling and the lower luminosity of $\bar{q}q$ over qg at large values of $\hat{s}/s$ in pp colliders. The lower rate requires smaller values of M_D to achieve a visible signal, and therefore a much more limited perturbative region. Therefore, the sensitivity range of M_D obtained from the photon signal is much smaller than in the jet case. Nevertheless, in case of discovery in the jet channel, the photon signal can provide a useful independent test.

Microscopic Black Hole Production at Colliders

One of the most exciting predictions of theories with large extra dimensions would be the possibility to create a microscopic black hole from particle collision at the LHC. This prediction is so amazing that it provokes debates not only among the particle physicists but it is also of a great interest to the public. However, this huge interest has not been fruitful all the time. Several doomsday scenarios appeared in which the produced microscopic black hole grows up and "eats" the entire planet Earth including all life on it. Some of these scenarios lead to petitions against the start-up the LHC accelerator.

These unpleasant things accompanying the start-up of the LHC lead to drawing up on an official "LSAG report" [58] by the LHC Safety Study Group[10], who concluded that

---

[10]They did not study only the possible production of microscopic black holes but also the hypothetical objects such as vacuum bubbles, magnetic monopoles and strangelets, and they found no associated risks.

n	D0	CDF		
	$\gamma + E_T$	jet $+ E_T$	$\gamma + E_T$	Combined
2	921	1210	1080	1400
3	877	1080	1000	1150
4	848	980	970	1040
5	821	910	930	980
6	810	880	900	940

Table 3.1: Lower limits on M_D in GeV at 95% CL for n from 2 to 6 observed in the jet$+E_T$ and $\gamma+E_T$ signatures and the combination of the two at CDF, and in the $\gamma+E_T$ signature at D0 [56].

black holes presented no danger:

> *"According to the well-established properties of gravity, described by Einstein's relativity, it is impossible for microscopic black holes to be produced at the LHC. There are, however, some speculative theories that predict the production of such particles at the LHC. All these theories predict that these particles would disintegrate immediately. Black holes, therefore, would have no time to start swallowing matter and to cause macroscopic effects."*

Also, several world-renowned experts in astrophysics, cosmology, general relativity, mathematics and particle physics have also expressed clear individual opinions that LHC collisions are not dangerous, as, for example, Steven Hawking who said:

> *"The world will not come to an end when the LHC turns on. The LHC is absolutely safe. ... Collisions releasing greater energy occur millions of times a day in the earth's atmosphere and nothing terrible happens."*

or Roger Penrose who noted:

> *"I certainly have no worries at all about the purported possibility of LHC producing microscopic black holes capable of eating up the Earth. There is no scientific basis whatever for such wild speculations."*

There are exact analysis [59] in the context of the warped brane-world scenarios as well, whose results are that the possibility of catastrophic black hole growth at the LHC is odd.

Microscopic black holes' properties, such as size of the horizon, mass, cross-section, lifetime, etc. will be described in more details in Chapter 4.

3.3 Warped Extra Dimensions

In the previous Section only flat extra dimensions have been considered. Now, let one see another, *warped*, scenario. Taking four-dimensional theory with only four-dimensional

sources necessarily leads to an expanding Universe. However, one can *balance* the effect of the four-dimensional brane source by putting four-dimensional sources into five dimensions. With five-dimensional bulk cosmological constant one could get a theory where the *effective* four-dimensional one would be vanishing, so that the four-dimensional Universe would still appear to be static and flat for an observer on a brane [63], [64].

However, this four-to-five dimensional trick is not "free of charge". The price to pay for this is that the five-dimensional background itself will be curved which simply follows from the fact that a bulk cosmological constant had to be introduced. The procedure introduced here is that one could "offload curvature" from the brane into the bulk and keep the brane to be flat by curving the extra dimension.

This warped scenario has been first pointed out by V. A. Rubakov and M. E. Shaposhnikov in 1983 [63], but in the following the best known and most concrete example of warped extra dimensions will be discussed: the Randall-Sundrum model.

In 1999, Lisa Randall and Raman Sundrum published two revolutionary papers [60], [61] on how to use the concept of extra dimensions in gravity in a new way. They proposed that the weak scale is generated from a large scale of order of the Planck scale, through an exponential hierarchy. It should be noted

Figure 3.8: From Lisa Randall's logbook [62].

that this exponential arises not from gauge interactions but from the background metric which is a slice of AdS_5 spacetime. This Randall-Sundrum (RS) model relies on the existence of only a single additional dimension. Lisa Randall explains a point of view of their RS model as [15]:

> "Suppose you have a theory with a single brane and five dimensions. Now naively, if you had a fifth infinite dimension, you wouldn't have thought that the gravitational force you see is a characteristic of four dimensions. After all, in four dimensions you see gravity fall off as one over distance squared. Naively, in five dimensions, you would find it fell off as one over distance cubed. But this changes when you have a brane. The brane gives you a different geometry. If you have a flat brane that carries energy in the bulk of the five-

> *dimensional space, then you find that the geometry can't be just flat space. In the simplest theory, it actually looks more like the graviton—the particle that mediates gravity—is trapped on the brane. It doesn't literally live on the brane, but most of its amplitude is concentrated near the brane."*

3.3.1 Model Set-Up

The RS model supposes a four-dimensional metric which is multiplied by a "warp" factor which is a rapidly changing function of an additional dimension. To satisfy all properties above mentioned, (that is even though the extra dimension is curve the brane itself remains static and flat) the most general metric is given by:

$$ds^2 = e^{-A(y)}dx^\mu dx^\nu \eta_{\mu\nu} - dy^2, \tag{3.32}$$

where $e^{-A(y)}$ is called the warp factor, x^μ are coordinates for the familiar four dimensions, while $0 \leq y \leq b$ is the coordinate for an extra dimension, which is a finite interval whose size is set by r_c. Since the source of the hierarchy is an *exponential* function of the compactification radius, to generate a large hierarchy does not require extremely large r_c.

The derivation of function $A(y)$ will not be reviewed here. Author in [83] showed that the non-factorizable RS metric is in its more well-known form given by

$$ds^2 = e^{-2k|y|}dx^\mu dx^\nu \eta_{\mu\nu} - dy^2, \tag{3.33}$$

where k is a scale of order of the Planck scale given as[11]

$$k^2 = -\frac{\Lambda}{24M_{RS}^3}. \tag{3.34}$$

The absolute value of y in (3.33) is taken because the extra dimension is compactified on an orbifold that identifies $y \leftrightarrow -y$.

Now let one have a look at the action of the RS model. It is given as

$$S = S_{bulk} + S_{Planck} + S_{TeV}, \tag{3.35}$$

in which

$$S_{bulk} = -\int d^5x \sqrt{-g}\left(M_{RS}^3 - \Lambda\right), \tag{3.36}$$

$$S_{Planck} = \int d^4x \sqrt{-g_{Planck}}V_{Planck}, \tag{3.37}$$

$$S_{TeV} = \int d^4x \sqrt{-g_{TeV}}\left(V_{TeV} + \text{SM Lagrangian}\right), \tag{3.38}$$

where g_{Planck} and g_{TeV} are the *induced* metrics of the Planck and TeV branes, respectively.

---

[11]M_{RS}, the quantum gravity scale in the RS model, is used here to be distinguished from M_* in the ADD model.
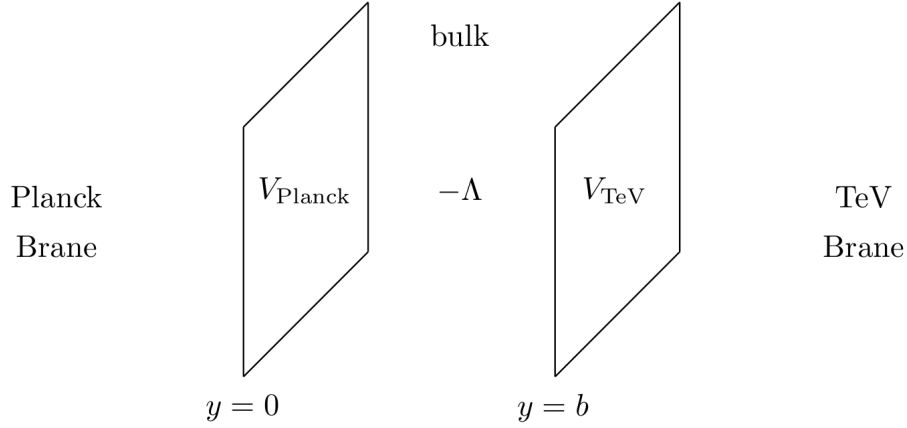
Figure 3.9: Sketch of the warped extra dimension RS model [81].

Using Einstein's equations to match the metric at $y = 0, b$, one obtains

$$V_{Planck} = -V_{TeV} = 24kM_{RS}^3, \tag{3.39}$$
$$\Lambda = -kV_{Planck} \tag{3.40}$$

in terms of the AdS curvature k and the fundamental quantum gravity scale M_{RS}. For more details see [61] or [84]. From eq. (3.39) and (3.40) one could simply get the relation for k given in eq. (3.34).

3.3.2   Physical Implications

Examine the Standard Model (SM) action:

$$S_{SM} = \int d^4x \sqrt{-g_{TeV}} \left[g_{TeV}^{\mu\nu} \left(D_\mu H\right)^\dagger D_\nu H - \lambda \left(H^\dagger H - v^2\right)^2 + \dots \right]. \tag{3.41}$$

If the size of extra dimension is b, then the induced metric at the negative tension is given by

$$(g_{TeV})_{\mu\nu} = e^{-2kb}\eta_{\mu\nu}. \tag{3.42}$$

Now insert the induced metric evaluated on the TeV brane (3.42) into the SM action (3.41) and one obtains

$$S_{SM} = \int d^4x e^{-4kb} \left[e^{2kb}\eta_{\mu\nu}\partial^\mu H \partial^\nu H - \lambda \left(H^\dagger H - v^2\right)^2 + \dots \right]. \tag{3.43}$$

Due to the non-trivial value of the induced metric on the negative tension brane the SM action above (3.43) is not canonically normalized. To get the action for the canonically

normalized fields one needs a field redefinition

$$\begin{aligned}
\widetilde{H} &= e^{-kb}H, \\
\widetilde{A}_\mu &= e^{-kb}A_\mu, \\
\widetilde{f} &= e^{-3kb/2}f.
\end{aligned}$$

(3.44)

With the canonically normalized fields (3.44) the SM action (3.43) is finally given as

$$S_{SM} = \int d^4x \left[\eta^{\mu\nu}(D_\mu\widetilde{H})^\dagger D_\nu\widetilde{H} - \lambda \left(\widetilde{H}^\dagger\widetilde{H} - (e^{-kb}v)^2 \right)^2 + \dots \right].$$

(3.45)

The result is that the warp factor can be rescaled away from all of the dimensionless terms of the SM by field redefinitions (3.44). The Higgs (mass)^2, the only dimensionful operator, gets physically rescaled. One could define a new Higgs vacuum expectation value that absorbs the warp factor by

$$\widetilde{v} = e^{-kb}v.$$

(3.46)

The relation (3.46) is completely general. It is worth noting that any mass parameter m on the visible 3-brane in the fundamental higher-dimensional theory will correspond to a physical mass

$$\widetilde{m} \equiv e^{-kb}m.$$

(3.47)

Eq. (3.47) shows that all mass scales are exponentially suppressed on the negative tension brane, but not on the positive one. That is why the positive tension brane is often also called the *Planck-brane* since the fundamental mass scale there would be unsuppressed of the order of the Planck scale. On the other hand, the negative tension brane is referred to as the *TeV-brane* since the relevant mass scale there is TeV.

What are the sizes of fundamental parameters? One could find the detailed derivation of the four-dimensional effective Planck scale, M_{Pl}, in [61] with the result

$$M_{Pl}^2 = M_{RS}^3 \int_{y=-b}^{y=+b} e^{-2k|y|}dy = \frac{M_{RS}^3}{k} \left(1 - e^{-2kb} \right).$$

(3.48)

One could clearly see from eq. (3.48) that there is a well-defined value for M_{Pl}, even in the $b \to \infty$ limit, where $b = r_c\pi$. This is an important result saying that M_{Pl} depends only weakly on r_c in the large kr_c limit.

Putting e^{kb} of order 10^{15} this mechanism produces TeV physical mass scales from the fundamental ones not far from the Planck scale, 10^{19} GeV. To obtain this, since geometric factor is an exponential, one does not need to require very large hierarchies among the fundamental parameters, v, k, M, and $\mu_c \equiv 1/r_c$; the only thing one needs to require is $kr_c \approx 50$ [61].

The Randall-Sundrum model proposes another way to solve the hierarchy problem. One could consistently exist with an infinite fifth dimension without violating known tests of gravity. Also, it clearly ties in well with the holographic picture which is described in [65]. The Randal-Sundrum model might even provide a new perspective for solving unresolved issues in quantum gravity and cosmology.

3.4 Universal Extra Dimensions

As it was already mentioned above, one of the deepest problems confronting current understanding of fundamental physics is the extreme weakness of the gravitational interaction compared with other fundamental forces. This problem could be partially solved by assuming the existence of extra spatial dimensions. In the last two Sections there were presented two models (ADD and RS) that both could help one to solve the hierarchy problem in the particle physics. In this Section another extra dimensional scenario will be mentioned - *Universal extra dimensions* (UED).

One could find some earlier work with this UED idea in [69]. The UED scenario proposes several attractive features from a particle physics' point of view as well as some cosmological impact. The theoretical background with mathematical description of the UED scenarios could be found in [66], [67], and [68].

3.4.1 UED Models and Collider Signals

The pictures in which only gravity could propagate to extra dimensions lead to interesting consequences for low-energy phenomenology (here it means TeV scale). Looking now at the effective four-dimensional theory, the five-dimensional graviton field appears as one four-dimensional massless graviton plus an infinite number of four-dimensional massive graviton fields (known as Kaluza-Klein towers) with masses equally spaced by an interval $\sim 1/R$. The massless graviton and the individual massive gravitons (the Kaluza-Klein excitations) have the same interaction with normal matter.

Let one have a look at a more general theory. Allowing that all Standard Model (SM) fields could propagate in the bulk one gets one of the UED models[12]. However, this assumption would imply that also the SM particles acquire a Kaluza-Klein (KK) tower of excitations with the same quantum numbers as the original fields. Till now, no such excitations have been observed in collider experiments, which means either the SM fields do not propagate in the bulk, or the scale on which they propagate is much smaller (of order TeV^{-1}) than the scale associated with gravity. A number of studies has been done, which indicates that letting the SM fields to propagate in extra dimensions implies that they must be compactified at a scale $1/R$ above a few TeV (see Ref. [70] and referencies therein). In the following, the UED model of Appelquist, Cheng, and Dobrescu [66] will be considered, which means that all the SM fields are placed in the bulk.

The UED models have some specific features worth noting, as, for example, conservation of momentum in the extra dimensions. This results in a selection rule called Kaluza Klein number conservation. As authors in [66] pointed out

> "... *extra dimensions accessible to all the standard model fields, referred to here as universal dimensions, may be significantly larger. The key element is the conservation of momentum in the universal dimensions. In the equivalent*

---

[12]There are also the UED models where only a subset of SM fields (for example, gauge bosons) propagate in the bulk.

> *four-dimensional theory this implies KK number conservation. In particular there are no vertices involving only one non-zero KK mode, and consequently there are no tree-level contributions to the electroweak observables. Furthermore, non-zero KK modes may be produced at colliders only in groups of two or more. Thus, none of the known bounds on extra dimensions from single KK production at colliders or from electroweak constraints applies for universal extra dimensions."*

This UED model, where all of the SM fields propagate into one or more extra dimensions could look as a generalization of the usual SM wall to a $3 + n$ wall, and also it may look more natural then fields selective, ADD and RS, scenarios. One may think that the collider bounds on the compactification scale would be significantly strengthened as more SM fields are free to propagate into the extra dimensions. However, the UED scenario has much weaker collider bounds due to the KK number conservation.

In the case of a single extra dimension, the electroweak observables were estimated to allow a compactification scale as low as 300 GeV[13] [66]. The Tevatron Run I mass bound is about 350-400 GeV and Run II could push this limit up to 450-550 GeV. The Large Hadron Collider (LHC) will either discover the UED KK excitations of the quarks and gluons or extend the mass limit to about 3 TeV [67]. For the case of two extra dimensions the electroweak observables become more sensitive to the cut-off on the effective six-dimensional theory and for more then two extra dimensions this sensitivity is more severe.

Now let one have a look at the signal in detectors. In this UED scenario, the tree level masses of the first level KK excitations of SM particles are almost degenerated. This would imply that the most first level KK paticles are stable, and therefore very hard to see at colliders. However, with radiative corrections this degeneracy is lifted and these corrections allow the first level KK excitations to decay[14] to the lightest KK particle (LKP), which is the γ^* (an excellent candidate for dark matter). This LKP is stable and observation of such a KK excitations production and decay in collider experiments will be difficult because the radiations of the SM particles during these decays to γ^* are rather soft. The phenomenology of this model, where the missing energy is carried away by the γ^*'s, and the soft SM particles radiated away in the process of the decay has been studied in [71].

Consider now an alternative model. Macesanu, McMullen, and Nandi proposed to add to this model KK number conservation violating interactions mediated by gravity [72]. The experimental consequences of this model could be quite interesting, because (with some presumptions, of course) the γ^* will decay to a photon and a KK graviton. The experimental signal will be then a striking two photon + missing energy event (due to

---

[13]Newer analysis of electroweak precision data [75] sets a limit on the masses of first level KK excitations as high as 700 GeV.

[14]It should be noted that the decay of the KK excitations of massive gauge bosons and heavier fermions to lighter KK states and SM fields depends on the final state. If there is a massless final state after SM decay, such as $Z \to \nu\bar{\nu}$ there are corresponding decays involving their KK excitations, such as $Z^* \to \nu^*\bar{\nu}$. However, massive decay depends on compactification scale and, for example, $t^* \to W^+b^*$ is forbidden for a 400 GeV compactification scale (but decay to $W^{+*}b$ is allowed).

escaping gravitons). Moreover, since the photons are coming from the decay of a heavy particle (the γ^*), their transverse momentum will be large, and the signal will be easy to separate from the SM background. Studies for this model have been already done and the results with all cuts and detailed analysis could be found in [72] and referencies therein. The recent searches with the LHC could be found in [73], [74].

3.4.2 Pair Production of Kaluza-Klein Excitations

As it was already mentioned the main way of obtaining Kaluza-Klein (KK) matter excitations will be the pair production at hadron colliders. Therefore, since one has to produce two massive particles in the final state, one needs a large centre-of-mass energy. The processes could be classified as follows:

- two quark KK excitations

- one quark excitation and one gluon excitation

- two KK gluons

Let one take into account radiative corrections to the masses of KK excitations. These corrections could play an important role in the phenomenology of extra-dimensional theories. The reason is that the KK states of a given level are all nearly degenerated, and so these small corrections could determine which states decay and which are stable. Taking these corrections into account introduces a new parameter: the cut-off scale Λ. This scale presents the energy scale up to which the effective description of the theory in terms of four-dimensional KK excitations works. This cut-off scale Λ cannot be much bigger than $1/R$ [76].

The gluon excitations g^* will decay to a quark pair as

$$g^* \rightarrow q^* q, \tag{3.49}$$

where q is a SM particle and q^* is a first level KK excitation. The quark excitations (either produced directly or through the decay of a g^*) will decay through electroweak interactions as

$$
\begin{aligned}
q^* &\rightarrow qZ^* \rightarrow q\bar{l}l^*, \ q\bar{\nu}\nu^* \tag{3.50} \\
q^* &\rightarrow qW^* \rightarrow q\bar{\nu}l^*, \ q\bar{l}\nu^* \tag{3.51} \\
q^* &\rightarrow q\gamma^* \tag{3.52}
\end{aligned}
$$

(and the charge conjugate ones), with the branching ratio 33%, 65%, and 2% respectively. The branching ratios for the Z^* decay to neutrinos versus leptons are roughly equal. Finally, the KK excitations of leptons and neutrinos will decay to the lightest KK particle (LKP) γ^* as

$$
\begin{aligned}
l^* &\rightarrow l\gamma^* \tag{3.53} \\
\nu^* &\rightarrow \nu\gamma^*. \tag{3.54}
\end{aligned}
$$

The production of KK excitations of SM matter is also possible at the e^+e^- colliders as well. However, there are some things worth to note. First, one would need the centre-of-mass energy to be higher than two times the mass of the first KK excitation. Secondly, in the e^*e^- collider there will be productions of KK excitation of weakly interacting particles rather than strongly interacting ones. Also, the next-generation linear collider will have centre-of-mass energy ~ 3 TeV or bellow, so that these KK excitations should be accessible at the LHC too. Therefore, linear collider will not present a discovery machine, however, thanks to the cleanest environment in e^+e^- collisions, it will be possible to measure the properties of the particles in more detail [77].

3.4.3 Gravity-Mediated Decays of Kaluza-Klein Particles

Now consider a scenario in which all extra dimensions are large (order inverse eV), gravity propagates all the way in this space (bulk), the matter fields, however, are restricted to a small region in the fifth dimension. One would see in this scenario an extension of the ADD model, where matter is confined on a four-dimensional brane with zero width in extra dimensions. One could modify this scenario with an assumption that this brane has a finite width (of order inverse TeV)[15] in the fifth dimension.

Phenomenological consequences of such a scenario are quite interesting. There is no longer a momentum conservation in the fifth dimension and, therefore, the Kaluza-Klein (KK) number conservation does not hold anymore for matter-gravity interactions, as it was already mentioned above. The result is that the first level KK excitations of matter could decay by radiating gravitons.

There are three separate scenarios for the phenomenological signal depending on the relative strength of the decay channels of the KK excitations:

- the gravitational decay dominates

- the decay due to mass splitting between the first level KK excitations takes place first

- the gravitational and strong/electroweak decay widths are of comparable magnitude

In the first case the KK excitations of gluons and quarks decay to SM gluons and quarks plus gravitons. In the second one the KK excitations of quarks and gluons will decay to the lightest KK particle (LKP) radiating low-p_T quarks and leptons in the process. The LKP will then decay gravitationally, leaving behind high-p_T photons and gravitons which will appear as missing energy. The last case allows for a q^* to follow just several steps in the decay chains (3.51) and (3.52), for example, to a l^*, and the KK excitation of the lepton will then decay gravitationally, leaving behind a high-p_T lepton.

First type scenario has been studied in some detail in [67]. In this case the signal will be two jets plus missing energy. Authors in [67] showed that the cross-section decreases faster as a function of p_T cut for more extra dimensions and also the missing energy is

---

[15]that is why it is sometimes called "fat brane"

typically smaller. The reason is that the larger the number of extra dimensions is, the higher is the mass of the gravitons one needs. Therefore, the smaller the energy available for the SM quarks and gluons rests.

The second scenario was discussed in [72]. Here, the KK excitations of gluons and quarks pair-produced will first decay to the LKP radiating low-p_T quarks and leptons in the process. Then, the LKP will decay gravitationally. The observed signal for this case will be two high-p_T photons accompanied by several jets and leptons with low p_T, and large missing energy.

Finally, in the third case, one of the KK excitations of quarks and gluons could decay gravitationally, while the other may decay first to the LKP. Taking a look at the signal, one observes jet + photon + missing energy. Moreover, it is also possible that one (or both) of the initial KK excitations will decay to a KK excitation of a lepton, which in turn will decay gravitationally, leading to signals with jet + lepton, photon + lepton and two leptons in the final state.

3.5   Living in Higher-Dimensional Space-time

The possibility of living in a higher-dimensional space-time opens many new ways in particle physics and cosmology towards understanding unsolved mysteries of today's physics. Mainly the unification of gravity with the other fundamental forces. In addition, they also provide a new way to look at the puzzles of the Standard Model such as the explanation of the observed fermion number of generations [78] or a different view at the electroweak symmetry breaking [79]. There is also a cosmological impact, namely the fact that it rather naturally gives rise to a viable dark matter candidate [80].

Nevertheless, in spite of their attractivity, they have to resolve two fundamental problems in order to be taken seriously: (i) they provide no simple way of understanding small neutrino masses; and (ii) no simple way of suppressing proton decay. As perhaps all new subjects in physics, the models with extra dimensions may seem to open a way for new problems rather than completely solving any of them.

Every theory or model has to be experimentally tested to be taken seriously and to be accepted. Particle physicists have a great opportunity to confirm or reject these "higher-dimensional ideas", nowadays, at the Large Hadron Collider (LHC). As mentioned before, one way to verify the existence of extra dimensions is to observe the production of microscopic black holes. These microscopic black holes will not be created if only four-dimensional Universe does exist.

Therefore, it is obvious that detailed studies of data taken by the LHC detectors will be needed to observe any signs of production of microscopic black holes via their Hawking radiation decays to all spectrum of Standard Model particles. In the next Chapter, production, decay and other properties of these microscopic black holes will be reviewed. The main analysis of simulated data samples, influence of pile-up, and the first results from data collected in 2010 will be presented in the last Chapter.

Chapter 4

Microscopic Black Holes at Colliders

In recent theories with extra dimensions, described in previous Chapter 3, the fundamental Planck mass, M_{PL}, can be as low as the TeV scale. In these theories microscopic black holes could be produced at energies higher than the Planck mass at the Large Hadron Collider (LHC) which would have a centre-of-mass energy of 14 TeV. Once produced, microscopic black holes would decay very rapidly to a spectrum of particles by Hawking radiation. The production and decay of microscopic black holes in high-energy collisions became one of the most actively studied and rapidly evolving subjects in the phenomenology of models with extra dimensions over the past years. The observation of such a radiation in particle detectors would prove the existence of extra dimensions[1]. Therefore, well working analysis framework would be needed to observe the Hawking radiation in produced data at LHC and to distinguish it from ordinary particle collisions.

The object of this Chapter is to review the creation of microscopic black holes during particle collisions in a ground-based accelerator, such as LHC, in the context of a higher-dimensional theory. Also, the main assumptions, criteria and estimates for microscopic black holes creation, as well as their properties after their formation will be discussed. Finally, review of the current results for the emission of particles via the Hawking radiation both on the brane and in the bulk will be briefly presented.

4.1 Astronomical Black Holes

4.1.1 Not Even Light Can Escape

The concept of a black hole dates back to the eighteenth century. The British astronomer and geologist John Mitchell advanced the idea of the existence of a body "so massive that the escape velocity at its surface would be equal to the speed of light". In a paper he wrote to the Royal Society in 1783 he concludes that [85]:

---

[1]It should be stress that microscopic black holes in no way constitute any threat, being distinguished from the more familiar astronomical four-dimensional black holes.

> *"If the semi-diameter of a sphere of the same density as the Sun were to exceed that of the Sun in the proportion of 500 to 1, a body falling from an infinite height towards it would have acquired at its surface greater velocity than that of light, and consequently supposing light to be attracted by the same force in proportion to its vis inertiae, with other bodies, all light emitted from such a body would be made to return towards it by its own proper gravity."*

A few months later, after Albert Einstein developed his theory of General relativity in 1915, Karl Schwarzschild gave a solution to the gravitational field of a point mass and a spherical mass [86]. In 1931, Subrahmanyan Chandrasekhar calculated, using general relativity, that a non-rotating body of electron-degenerate matter above 1.44 solar masses (the so-called Chandrasekhar limit) would collapse [87]. A white dwarf slightly more massive than the Chandrasekhar limit will collapse into a neutron star, which is itself stable because of the Pauli exclusion principle. But in 1939, Robert Oppenheimer and others predicted [88] that neutron stars above approximately three solar masses (the so-called Tolman–Oppenheimer–Volkoff limit) would collapse into black holes[2] for the reasons presented by Chandrasekhar, and concluded that no law of physics was likely to intervene and stop at least some stars from collapsing to black holes.

Schwarzschild's solution of Einstein's equations of the General relativity describes the simplest non-rotating and neutral black hole. In 1963, Roy Kerr found the exact solution for a rotating black hole [89]. Two years later Ezra T. Newman found the solution for a black hole which is both rotating and electrically charged [90].

The term "black hole" was first publicly used by John Wheeler during a lecture in 1967. Although he is usually credited with coining the phrase, he always insisted that it was suggested to him by somebody else. It was Ann E. Ewing, a journalist who specialized in writing about science, who is thought to be the first to report on so-called black holes. As it was mentioned in the article in *The Washington Post* News [91]:

> *"Wheeler reportedly first used the term at a 1967 conference. However, Ms. Ewing used the term as early as 1964 in her story "Black Hole in Space" after apparently hearing it at a meeting of the American Association for the Advancement of Science. She did not identify the source of the quote."*

4.1.2 Looking at Sky

Although it may seem that the objects such as neutron stars or black holes may present only some theoretical results or science fiction, it turned out, that such objects do really exist. The first pulsar was discovered in 1967[3], which was within a few years shown to

---

[2]The collapsed stars were called "frozen stars" because an outside observer would see the surface of the star frozen in time at the instant where its collapse takes it inside the Schwarzschild radius.

[3]The first pulsar was discovered in November 1967 by Jocelyn Bell. Bell and Anthony Hewish investigated further and found out that the repeating signal had a period of 1.3373 seconds and originated from the same spot in the sky, night after night (Hewish won the 1974 Nobel Prize in physics for this discovery).

be rapidly rotating neutron star. Until that time, neutron stars were regarded as just theoretical curiosities. However, the discovery of pulsars showed their physical relevance.

In April–May 1971, Luc Braes and George Miley, and independently Robert M. Hjellming and Campbell Wade, detected radio emission from Cygnus X-1, and their accurate radio position pinpointed the X-ray source to the star Cygnus X-1. On the celestial sphere, this star lies about half a degree from the 4th magnitude star Eta Cygni (see Fig. 4.1). It is a supergiant star that is, by itself, incapable of emitting the observed quantities of X-rays. Hence, the star must have a companion that could heat the gas to the millions of degrees needed to produce the radiation source for Cygnus X-1.
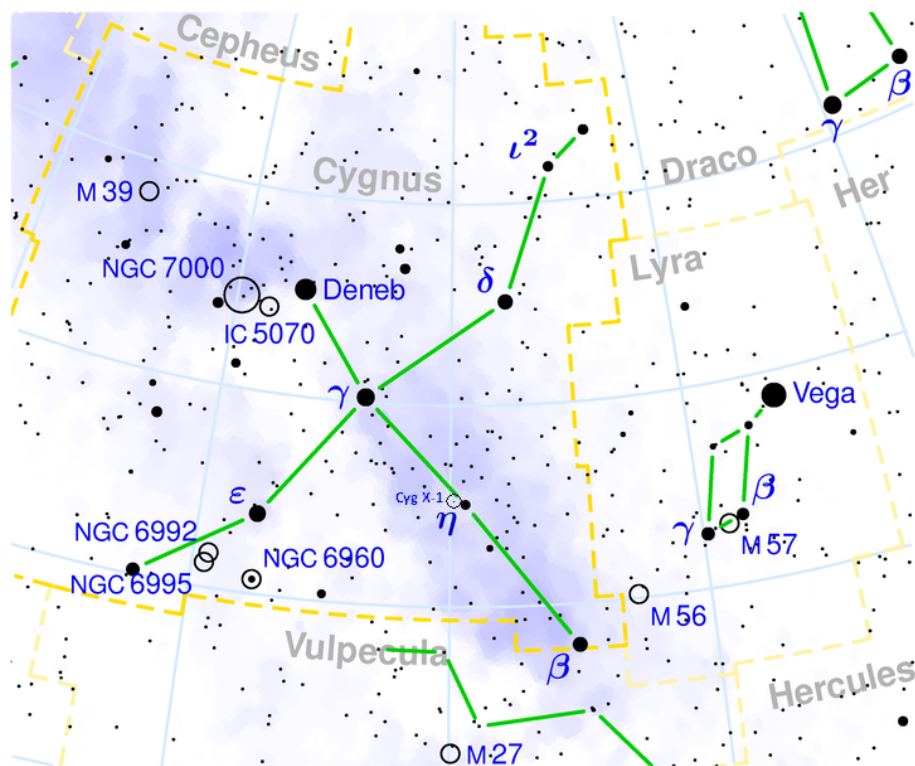
Figure 4.1: Cygnus constellation map with approximate position of Cygnus X-1 [92].

Louise Webster and Paul Murdin, and independently Charles Thomas Bolton, announced the discovery of a massive hidden companion to Cygnus X-1 in 1971. Measurements of the Doppler shift of the star's spectrum demonstrated the companion's presence and allowed its mass to be estimated from the orbital parameters. Based on the high predicted mass of the object, they surmised that it may be a black hole as the largest possible neutron star cannot exceed three times the mass of the Sun. With further observations strengthening the evidence, by the end of 1973 the astronomical community generally conceded that Cygnus X-1 was most likely a black hole.

Another example of the black hole one can find in the centre of the Milky Way galaxy. The Sagittarius A* radio source has been known for decades, since the very first radio

telescopes of the 1950's, but it was not until the 1970's that astronomers realised how compact the Sagittarius A* radio source was.

Towards the end of the 70's other evidence emerged. The movement of gas clouds near Sagittarius A* indicated that they must be circling a compact mass several million times greater than the Sun. Then astronomers proved that the radio source and the gravitational mass were centred at the same point. Other evidence of a weak infrared source at the same point also turned up. And the clincher was that Sagittarius A* is motionless relative to the rest of the Milky Way. In other words, the entire galaxy revolves around this object.

By tracking individual stars orbiting a common point, European Southern Observatory researchers have derived the best empirical evidence yet for the existence of a 4 million solar mass black hole. All the stars are moving rapidly, one star even completed a full orbit within those 16 years [93], [94] (see Fig. 4.2), allowing astronomers to indirectly study the mysterious beast driving Milky Way. Reinhard Genzel, team leader of this research, said [95]:

> *"Undoubtedly the most spectacular aspect of our 16-year study, is that it has delivered what is now considered to be the best empirical evidence that supermassive black holes do really exist. The stellar orbits in the galactic centre show that the central mass concentration of four million solar masses must be a black hole, beyond any reasonable doubt."*

Quite simply, the object influencing these stars must be a supermassive black hole, there is no other explanation out there. Does this mean that black holes have an even firmer standing as a cosmological "fact" rather than "theory"? It would appear so.

4.1.3 Are Black Holes Really Black?

For a long time it was suspected that black holes are really black and nothing can escape from them. Work of James Bardeen, Brandon Carter, and Stephen Hawking in the early 1970s led to the formulation of the laws of black hole mechanics [96].

The Zeroth Law: *The surface gravity, κ, of a stationary black hole is constant over the event horizon.*

The First Law: *Any two neighbouring stationary axisymmetric solutions containing a perfect fluid with circular flow and a central black hole are related by*

$$dM = \frac{\kappa}{8\pi}A + \Omega dJ + \Phi dQ, \tag{4.1}$$

where M and A are the mass and the area of the event horizon of the black hole, and Ω, J, Q and Φ are the angular frequency, the angular momentum, the conserved charge and its potential respectively. It can be seen that $\frac{\kappa}{8\pi}$ is analogous to temperature in the same way that A is analogous to entropy. However, $\frac{\kappa}{8\pi}$ and A are distinct from the temperature and entropy of the black hole.
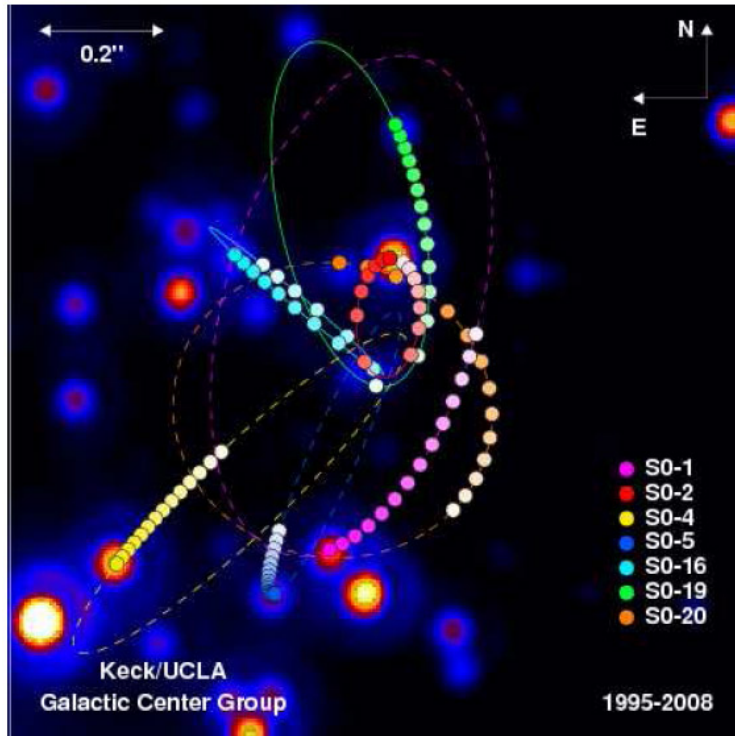
Figure 4.2: Stars within the 0.02 parsecs of the Galactic center orbiting an unseen mass. Yearly positions of seven stars are indicated with filled colored circles. Both curved paths and accelerations (note the non-uniform spacings between yearly points) are evident. Partial and complete elliptical orbital fits for these stars are indicated with lines. All orbital fits require the same central mass of $\approx 4 \times 10^6$ $M_\odot$ and common focus at the center of the image, the position of the radio source Sagittarius A* [93].

Interesting question could be what is the effective temperature of a black hole. Authors in [96] explained why it should be absolute zero:

> "... a black hole cannot be in equilibrium with black body radiation at any non-zero temperature, because no radiation could be emitted from the hole whereas some radiation would always cross the horizon into the black hole. If the wavelength of the radiation were very long, corresponding to a low black body temperature, the rate of absorption of radiation would be very slow, but true equilibrium would be possible only if there were no radiation present at all, i.e. if the external black body radiation temperature were zero."

Another way of seeing what they propose is that *"the red shifted effective temperature θ of any matter orbiting the black hole must tend to zero as the horizon is approached, because the time dilatation factor tends to zero on the horizon"*

The Second Law: *The area A of the event horizon of each black hole does not decrease with time, i.e.*

$$\delta A \geq 0. \tag{4.2}$$

If two black holes coalesce, the area of the final event horizon is greater than the sum of the areas of the initial horizons, i.e.

$$A_3 > A_1 + A_2. \tag{4.3}$$

This establishes the analogy between the area of the event horizon and entropy. Thing worth noting is that the second law of black hole mechanics is slightly stronger than the corresponding thermodynamic law. This comes from the fact that black holes cannot bifurcate, therefore one cannot transfer area from one black hole to another[4]. Thus the second law of black hole mechanics requires that the area of each individual black hole should not decrease.

The Third Law: *It is impossible by any procedure, no matter how idealized, to reduce κ to zero by a finite sequence of operations.*

These laws describe the behaviour of a black hole in close analogy to the laws of thermodynamics by relating mass to energy, area to entropy, and surface gravity to temperature. In 1974 Stephen Hawking then showed [97] that quantum field theory predicts that black holes should radiate like a black body with a temperature proportional to the surface gravity of the black hole.

Although these quantum effects violate the classical law that the area of the event horizon of a black hole cannot decrease (see eq. (4.2)), a *Generalized Second Law* remains $S + \frac{1}{4}A$ never decreases, where S is the entropy of matter outside black holes and A is the sum of the surface areas of the event horizons.

Unfortunately, the most prominent feature of a black hole - its Hawking radiation - has not been observed yet and is very unlikely to be ever observed by astronomical means. The reason is that even if one supposes the smallest (and therefore the hottest) astronomical black holes with mass close to the Tolman–Oppenheimer–Volkoff limit (about three solar masses), these black holes would have the Hawking temperature only[5] ~ 100 nK which corresponds to the wavelength of Hawking radiation of ~ 100 km.

Moreover, the black hole dissipating power corresponds to only ~ 100 photons per second emitted by its entire event horizon. So that even taking the closest known black hole candidate, which is still over a thousand of light years away from Earth, not a single

---

[4]In contrast to thermodynamics, where one can transfer entropy from one system to another requiring only that the total entropy does not decrease.

[5]Note that the event horizon temperature of these black holes is much lower than the temperature of the cosmic microwave background radiation. Therefore, at the present time the black holes are growing due to the accretion of relic radiation much faster than they are evaporating.

Hawking radiation photon ever hit Earth since it has been formed![6] Thus, if the astronomical black holes were the only ones to exist, the Hawking radiation would be always just a theoretical concept, never testable experimentally.

Besides the Hawking radiation there is another evidence for the existence of astronomical black holes. LIGO and VIRGO detectors are looking for an observation of gravitational waves created in the collisions of two black holes. However, current sensitivity of these interferometers is still short of the expected signal, even in optimistic cosmological scenarios.

This leads one to other places to look for black holes that are much smaller and consequently much hotter and easier to detect than their astronomical counterparts - the microscopic black holes produced at particle colliders within extra-dimensional scenarios.

4.2 Microscopic Black Holes within Extra Dimensions

It is now generally accepted that the scale of quantum gravity could be as low as a TeV. Taking this to be true then particle physics stands on the threshold of an exciting revolution in understanding of quantum gravity and perhaps even string theory. Production of microscopic black holes at particle accelerators would be the first window into the extra-dimensional world predicted by string theory, and required by several brane-world scenarios that provide for a low energy Planck scale.

4.2.1 Production of Black Holes

If the impact parameter b is larger than the Schwarzschild radius r_H, that corresponds to the center-of-mass energy of the two particles, elastic and inelastic processes will in general take place accompanied by the exchange of gravitons. However, if $b < r_H$ then strong gravitational effect will dominate and a black hole will be formed. The production cross-section is given by

$$\sigma_{BH} \sim \pi b^2 \sim \pi r_H^2, \tag{4.4}$$

where the Schwarzschild radius r_H is given as

$$r_H = \frac{1}{\sqrt{\pi} M_*} \left[\frac{M_{BH}}{M_*} \left(\frac{8\Gamma\left(\frac{n+3}{2}\right)}{n+2} \right) \right]^{\frac{1}{n+1}}. \tag{4.5}$$

The geometrical cross-section (4.4) is sometimes written in the form $\sigma_{BH} = F(s)\pi r_S^2$, where $F(s)$ is a dimensionless form factor. Even though $F(s)$ is usually chosen equal to one, possible corrections have been done to the cross-section, which effectively reduce it [99], [100]. For the trapped-surface approach and other corrections to black hole cross-section see [101] and [102].

---

[6]In fact, one would have to wait $\sim 10^{14}$ years to observe a single photon from such a black hole to hit the Earth.

4.2.2 Black Hole Properties

To be able to ignore quantum corrections and therefore study the produced black holes by using semi-classical methods, one has to assume that the mass of the black hole must be, at least, a few time larger than the scale of quantum gravity M_*. If one assumes that $M_* = 1$ TeV, a safe limit for the mass of the produced black hole would be $M_{BH} = 5$ TeV [103]. Keeping the mass of the produced black hole fixed, one can calculate the value of the horizon radius (4.5) as a function of n (see Tab. 4.1).

n	1	2	3	4	5	6	7
$r_H [10^{-4} \text{ fm}]$	4.06	2.63	2.22	2.07	2.00	1.99	1.99

Table 4.1: Black hole horizon radii for different values of n, $M_{BH} = 5$ TeV.

As one can observe from the Table above during the collision of two particles with a centre-of-mass energy $\sqrt{s} \geq 5$ TeV, a black hole may be formed if the particles pass within an area of radius 10^{-4} fm. This distance is attainable at today's particle physics experiments.

Now look at a case without extra dimensions. The lightest semi-classical black hole would have a mass, at least, several times the four-dimensional Planck mass, $M_{Pl} \simeq 10^{16}$ TeV. Such an energy needed for the creation of a black hole from a high-energy collision is a requirement far beyond the reach of any present or future accelerator. Moreover, overlooking for the moment the fact that a four-dimensional black hole with $M_{BH} < M_{Pl}$ would not be a classical object, one may ask, just for comparison, what would be the value of the Schwarzschild radius for an object with mass $M = 5$ TeV. Using the Schwarzschild relation in four dimensions, one gets the extraordinary value of $r_H = 1.3 \times 10^{-50}$ m, i.e. 35 orders of magnitude smaller than the radius of the proton.

Return back to extra dimensions. As it was already mentioned, black hole has a non-zero temperature and emits thermal radiation, the so-called Hawking radiation. The temperature of a $(4 + n)$-dimensional black hole is given by

$$T_H = \frac{(n+1)}{4\pi r_H},\qquad(4.6)$$

where r_H is the Schwarzschild radius given in (4.5). Taking again that $M_* = 1$ TeV and $M_{BH} = 5$ TeV then, using the entries of Tab. 4.1, one may easily calculate the temperature of the produced black hole for different values of n (see Tab. 4.2).

n	1	2	3	4	5	6	7
T_H [GeV]	77	179	282	379	470	553	629

Table 4.2: Black hole temperatures for different values of n, $M_{BH} = 5$ TeV.

All temperature values displayed in Tab. 4.2 lie in the GeV regime, which is the energy range that present experiments can probe. Therefore, the presence of extra dimensions not only facilitates the creation of a black hole at a high-energy collision, but also renders more likely the detection of their most prominent feature, the emitted Hawking radiation. Without this extra-dimensional tool, the experimental observation of the Hawking radiation from a four-dimensional black hole would be quite impossible, as it was mentioned above.

Looking at eqs. (4.5) and (4.6), one may conclude that a $(4 + n)$-dimensional black hole would have a horizon radius much larger that a four-dimensional one with the same mass. Furthermore, it would have in $n > 0$ a temperature much lower than the one in $n = 0$. Supposing that a black hole with $M_{BH} = 5$ TeV is allowed to exist in nature in $n = 0$, its temperature would have been 30 orders of magnitude larger than the entries in Tab. 4.2.

Moreover, the larger the temperature of the black hole is, the faster its decay rate is (through the emission of Hawking radiation) and, therefore, the shorter is its lifetime. Now take a look at an astronomical black holes with mass $M_{BH} \geq 3M_\odot$. They emit radiation with extremely small rate (if any[7]) and their lifetime is given by the four-dimensional relation

$$\tau \sim \frac{1}{M_{Pl}} \left(\frac{M_{BH}}{M_{Pl}} \right)^3 . \tag{4.7}$$

The lifetime of such black holes is much larger that the age of the Universe. However, for black holes within extra dimensions, the relation (4.7) is modified as

$$\tau \sim \frac{1}{M_*} \left(\frac{M_{BH}}{M_*} \right)^{(n+3)/(n+1)} . \tag{4.8}$$

At first guess it may seem that lowering energy scale from M_{Pl} to M_* leads to black holes lifetime much longer than the one in four dimensions. That is correct. Nevertheless, one has to keep in mind that in a particle high-energy collisions a black hole masses would be in the area of a few TeV. Therefore, the lifetime is only a tiny fraction of a second. For a black hole of mass $M_{BH} = 5$ TeV the lifetime ranges from $\tau = 1.7 \times 10^{-26}$ s (for $n = 1$) to $\tau = 0.5 \times 10^{-26}$ s ($n = 7$). In the case of 10 TeV black hole the corresponding life time interval is from $\tau = 1.6 \times 10^{-26}$ s ($n = 1$) to $\tau = 1.2 \times 10^{-26}$ s ($n = 7$).

4.3   Evaporation of Black Holes

Having discussed the properties of the microscopic black holes that may be created during a high-energy particle collisions, let one now proceed to discuss in more detail the spectra of the Hawking radiation emitted by these black holes and the information on particle and spacetime properties that one may deduce from them.

---

[7]As already mentioned, these black holes have a temperature much smaller than the one of the Cosmic Microwave Background Radiation, therefore, they actually absorb radiation from their environment instead of emitting.

4.3.1 Black Hole Decay

It is well known from General relativity that nothing can escape from inside the horizon of a black hole. The emission of Hawking radiation is in fact compatible with this result, because the Hawking radiation can be conceived as the creation of a virtual pair of particles just outside the horizon of the black hole. After the creation one particle may escapes to infinity while the second falls into the black hole. The spectrum of the Hawking radiation coming from a black hole with temperature T_H is a thermal one with almost blackbody profile.

The flux spectrum, the number of particles emitted per unit time, from a spherically-symmetric microscopic black hole could be found by generalizing the corresponding four-dimensional expression [97] for a higher number of dimensions. It is given by

$$\frac{dN^{(s)}(\omega)}{dt} = \sum_j \sigma_{j,n}^{(s)}(\omega) \frac{1}{\exp[\omega/T_H] \pm 1} \frac{d^{n+3}k}{(2\pi)^{n+3}}, \tag{4.9}$$

where s is the spin of the emitted degree of freedom, j its angular momentum quantum number and T_H is a black hole temperature. The spin statistics factor in the denominator is -1 for bosons and $+1$ for fermions and k depends on the mass of the particle. For massless particles, $|k| = \omega$ and the phase-space integral reduces to an integral over the energy of the emitted particle ω. For massive particles, $|k|^2 = \omega^2 - m^2$, and the energy in the denominator now includes the rest mass of the particle: this means that a black hole temperature $T_H > m$ is necessary for the emission of a particle with mass m. As the decay progresses, the black hole mass decreases and the Hawking temperature rises[8].

The power spectrum, the energy emitted per unit time by the black hole, can be found by combining the number of particles emitted with the amount of energy they carry. It is given as

$$\frac{dE^{(s)}(\omega)}{dt} = \sum_j \sigma_{j,n}^{(s)}(\omega) \frac{\omega}{\exp[\omega/T_H] \pm 1} \frac{d^{n+3}k}{(2\pi)^{n+3}}. \tag{4.10}$$

Both expressions, (4.9) and (4.10), contain additional factor, $\sigma_{j,n}^{(s)}(\omega)$, which does not usually exist in a typical blackbody spectrum. This factor depends on the energy of the emitted particle, its spin and its angular momentum number. It may therefore significantly modify the spectrum of the emitted radiation and that is why it is called the *greybody* factor. Equally important is its dependence on the number of extra dimensions and therefore it encodes valuable information for the structure of the spacetime around the black hole, including the dimensionality of spacetime.

Now let one briefly look at what greybody factor stands for. It should be clear that any particle emitted by a black hole has to traverse a strong gravitational background before reaching an observer at infinity, unlike to what happens with a blackbody in flat

---

[8]It is usually assumed that a quasi-stationary approach to the decay is valid - that is, the black hole has time to come into equilibrium at each new temperature before the next particle is emitted.

spacetime. Therefore, the radiation spectrum is bound to depend on the energy of the propagating particle and the shape of the gravitational barriers. So that these are the parameters that will determine the number of particles that manage to reach infinity.

The greybody factor $\sigma_{j,n}^{(s)}(\omega)$ thus stands for corresponding transmission cross-section for a particle propagating in the strong gravitational background. This quantity can be determined by solving the equation of motion of a given particle and computing the corresponding absorption coeficient $\mathcal{A}_j^{(s)}$. The derivation will not be reviewed here and could be found in [104]. Let one just give the result to see the dependencies.

$$\sigma_{j,n}^{(s)}(\omega) = \frac{2^n}{\pi}\Gamma\left(\frac{n+3}{2}\right)^2 \frac{A_H}{(\omega r_H)^{n+2}}N_j|\mathcal{A}_j^s|^2, \tag{4.11}$$

where N_j is the multiplicity of states corresponding to the same partial wave j, given for a $(4+n)$-dimensional spacetime by

$$N_j = \frac{(2j+n+1)(j+n)!}{j!(n+1)!} \tag{4.12}$$

and A_H is the horizon area of the $(4+n)$-dimensional black hole defined as

$$A_H = r_H^{n+2}(2\pi)\pi^{(n+1)/2}\Gamma\left(\frac{n+3}{2}\right)^{-1}. \tag{4.13}$$

One may see from eq. (4.11) that the greybody factor is indeed proportional to the area of the emitting body, as in the case of blackbody emission, nevertheless additional factors change, in principle, this simple relation by adding an explicit dependence on ω, r_H, j and number of extra dimensions, n.

Four-dimensional analyses [105] for Schwarzschild and Kerr black holes have been done to determine the greybody factors for particles of different spin. Taking the simplest case of non-rotating Schwarzchild black hole, it was shown [106] that in the limit of high energy ω, $\sum_j \sigma_{j,n}^{(s)}(\omega)$ is a constant independent of ω. The low-energy behaviour, on the other hand, is strongly spin-dependent and energy-dependent, and the greybody factors are significantly different. The spin dependence of the greybody factors means that they are necessary to determine the relative emissivities of different particle types from a black hole.

Authors in [107] showed that the charged black hole will quickly discharge through a Schwinger-type pair-production process. Charge of the black hole could affect the geometry of spacetime and thus the emission of particles, but that would happen only for black holes with masses larger than $10^5 M_\odot$.

In the General relativity, black hole evaporation is expected to occur in three distinct phases: balding, spin-down, and Schwarzschild phase.

- The *balding phase*: the black hole emits mainly gravitational radiation and sheds the "hair" inherited from the original particles, and the asymmetry due to the violent production process.

- The *spin-down phase*: the typically non-zero impact parameter of the colliding partons leads to black holes with some angular momentum around an axis perpendicular to the plane. During this phase, the black hole loses its angular momentum through the emission of Hawking radiation.

- The *Schwarzschild phase*: a spherically-symmetric black hole loses energy due to the emission of Hawking radiation. This results in the gradual decrease of its mass and the increase of its temperature.

4.3.2 Information Loss Paradox

In quantum gravity, it is expected that there is a fourth, Planck phase of black hole evaporation. Once the black hole has reached a mass close to effective Planck scale, it falls into regime of quantum gravity and predictions become increasingly difficult. Some authors speculate that the Planck phase terminates with a formation of a stable or semi-stable black hole remnant. Others argue that the evaporation proceeds until the entire mass of the black hole is radiated. The truth is that no predictions about the Planckian regime are possible, given one's lack of knowledge of quantum gravity. Beside the fact that black hole remnant could be a candidate for dark matter [108] it may also solve the so-called *information loss paradox* [109].

Hawking's conclusion that the information that entered a black hole can be forever lost comes directly from his consideration that black hole radiation is featureless thermal black body radiation, which loses information about its source. His position implies that black hole evolution is non-unitary, violating one of the most basic principles of quantum theory. He argued that as the black hole radiates, it will eventually completely evaporate away. The resulting radiation state would be principally thermal so there would be no way to retrieve the initial state. The time-reversal symmetry would be violated if the information is lost.

The emitted radiation is thermal (uncorrelated), therefore, the emitted radiation does not depend on the structure of the collapsed body that formed the radiating black hole. The radiation depends only on the geometry of the black hole outside the horizon and cannot depend or be correlated with the collapsed body.

If one waits long enough, the black hole will evaporate completely, leaving behind only the thermal radiation. The thermal radiation, which is a mixed state, is now the whole system. The consequence of such a process is the fact that beginning with a pure state does not allow one to predict with certainty, what will the final quantum state be (the final system is a mixed state so one can only assign probabilities to different final states).

Therefore, the evaporation of a black hole, as described above, results in a paradox. This paradox is known as the information loss paradox, since from an initially pure state, which has zero entropy, one ends up with a mixed state, which has non-vanishing entropy.

There are three main approaches to find a solution to the black hole information paradox: The first accepts the information loss. The second asserts that the information

is retrieved during the evaporation process or via effects, which occur around the Planck scale. The last relies on the possible existence of Planck scale black hole remnants.

4.4 Hawking Radiation on Brane

The emission of Hawking radiation, i.e. the evaporation of a microscopic black hole via the emission of elementary particles, takes place during the spin-down and Schwarzschild phase of its life. Although the emission during the Schwarzschild phase of a microscopic black hole was studied, both analytically and numerically, quite early, the complexity of the gravitational background around a similar, but rotating, microscopic black hole delayed the study of the spin-down phase.

During the last few years, several studies have derived results for the various spectra characterising the emission of elementary particles on the brane by a rotating microscopic black hole. In this and the next Section, studies of the emission of Hawking radiation during the spin-down and Schwarzschild phase on the brane as well as in the bulk will be reviewed. These results are important to study microscopic black hole events in particle collisions and separate them from other events.

4.4.1 Hawking Radiation During Spin-down Phase

First let one have a look at the spin-down phase during which the black hole has a non-vanishing angular momentum - this is the most generic situation for a black hole created by a non-head-on particle collision. Assuming that the produced black hole has an angular-momentum component only along an axis in three-dimensional space, the line-element that describes the gravitational background around such a microscopic black hole is given by the Myers-Perry solution [110]

$$ds^2 = \left(1 - \frac{\mu}{\Sigma r^{n-1}}\right) dt^2 + \frac{2a\mu \sin^2\theta}{\Sigma r^{n-1}} dt d\varphi - \frac{\Sigma}{\Delta} dr^2 - \Sigma d\theta^2$$
$$- \left(r^2 + a^2 + \frac{a^2\mu \sin^2\theta}{\Sigma r^{n-1}}\right) \sin^2\theta d\varphi^2 - r^2 \cos^2\theta d\Omega_n, \qquad (4.14)$$

where

$$\Delta = r^2 + a^2 - \frac{\mu}{r^{n-1}}, \qquad \Sigma = r^2 + a^2 \cos^2\theta, \qquad (4.15)$$

and $d\Omega_n$ is the line-element on a unit n-sphere and $0 < \varphi < 2\pi$, $0 < \theta < \pi$. The parameters μ and a are related to the mass and angular momentum, respectively, of the black hole through the definitions

$$M_{BH} = \frac{(n+2)A_{n+2}}{16\pi G}\mu, \qquad J = \frac{2}{n+2}M_{BH}a, \qquad (4.16)$$

with G being the $(4+n)$-dimensional Newton's constant, and A_{n+2} the area of a $(n+2)$-dimensional unit sphere given by

$$A_{n+2} = \frac{2\pi^{(n+3)/2}}{\Gamma[(n+3)/2]}. \tag{4.17}$$

Since the creation of the black hole depends crucially on the value of the impact parameter between the two highly-energetic particles, and that in return defines the angular momentum of the black hole, an upper bound can be imposed on the angular momentum parameter a of the black hole by demanding the creation of the black hole itself during the collision. The maximum value of the impact parameter between the two particles that can lead to the creation of a black hole is

$$b_{max} = 2\left[1 + \left(\frac{n+2}{2}\right)^2\right]^{-\frac{1}{n+1}} \mu^{\frac{1}{n+1}}. \tag{4.18}$$

Authors in [112] put an upper bound to the value of the black hole angular momentum parameter

$$a_*^{max} = \frac{n+2}{2}. \tag{4.19}$$

In the above, the quantity $a_* \equiv a/r_H$ has been defined. One may see that for $n > 1$ it would have been unrestricted, contrary to the cases of $n = 0$ and $n = 1$, where a maximum value of a exists that guarantees the existence of a real solution for the black hole horizon.

Since there is now an interest in the emission of the brane-localised modes by the black hole, one should first determine the line-element on the brane by fixing the values of "extra" angular coordinates. This results in a disappearance of the $d\Omega_n^2$ part of the metric (4.14) leaving the remaining unaltered. To study the emission of scalars, fermions and gauge bosons by the aforementioned projected black hole background one assumes that the emitted particle modes couple only minimally to the gravitational background and have no other interactions.

The absorption coefficient $|\mathcal{A}|^2$ for the propagation of the field on a specific gravitational background is given as

$$|\mathcal{A}|^2 \equiv 1 - |\mathcal{R}|^2 \equiv \frac{\mathcal{F}_{horizon}}{\mathcal{F}_{infinity}}, \tag{4.20}$$

where $\mathcal{R}$ is the reflection coefficient and $\mathcal{F}$ the flux of energy towards the black hole.

This quantity is needed to compute the Hawking radiation of the black hole on the brane. For example, the differential energy emission rate is given by

$$\frac{d^2 E}{dt d\omega} = \frac{1}{2\pi} \sum \frac{\omega}{\exp[\tilde{\omega}/T_H] \pm 1} |\mathcal{A}|^2, \tag{4.21}$$

and similarly for the particle flux, i.e. the number of particles emitted per unit time and unit frequency, and also for angular momentum emission rates as

$$\frac{d^2N}{dtd\omega} = \frac{1}{2\pi}\sum \frac{1}{\exp[\tilde{\omega}/T_H] \pm 1}|\mathcal{A}|^2, \qquad \frac{d^2J}{dtd\omega} = \frac{1}{2\pi}\sum \frac{m}{\exp[\tilde{\omega}/T_H] \pm 1}|\mathcal{A}|^2, \qquad (4.22)$$

where ± 1 factor is a statistic factor for fermions and bosons and the parameter $\tilde{\omega}$ and T_H are defined as

$$\tilde{\omega} \equiv \omega - m\Omega_H = \omega - m\frac{a}{r_H^2 + a^2}, \qquad T_H = \frac{(n+1) + (n-1)a_*^2}{4\pi(1 + a_*^2)r_H}, \qquad (4.23)$$

with Ω_H the angular velocity, T_H the temperature of the black hole and r_H the black hole horizon radius.

Despite the complexity of the gravitational background, the absorption probability $|\mathcal{A}|^2$ can be found analytically in the low-energy and low-angular-momentum regime. Fig. B.1 depicts the behaviour of $|\mathcal{A}|^2$ in terms of the angular momentum parameter a_* and number of extra dimensions n for the scalar case, and Figs. B.2 and B.3 for fermions and gauge bosons, respectively. Fig. B.4 plots the energy emission rates for the indicative cases of brane-localised scalars and gauge bosons in terms again of the angular-momentum parameter and number of extra dimensions. It should be clear that an increase in any of these two parameters results in the significant enhancement of the energy emission rate (all in Appendix B). Detailed analysis and other results could be found in [111] and [112].

Let one finally comment on a particular feature that the radiation spectra from the spin-down phase in the life of the black hole have. The spin-down line-element that describes background around the black hole phase possesses a preferred axis in space - the rotation axis of the black hole. As a result, the radiation spectra of all emitted particles have a non-trivial angular dependence. Fig. 4.3 shows the energy emission rates for scalars, fermions and gauge bosons, from a 6-dimensional, rotating black hole with $a_* = 1$, as a function of the energy parameter ωr_H and the $\cos(\theta)$ of the angle measured from the rotation axis of the black hole. In all spectra, one observes that most of the energy is emitted along the equatorial plane ($\theta = \pi/2$) as a result of the centrifugal force that is exerted on all species of fields. Moreover, as Fig. 4.3(c) reveals, a significantly larger amount of energy (by, at least, an order of magnitude) is spent by the black hole in the emission of gauge bosons the above result holds for all values of n.

4.4.2 Hawking Radiation During Schwarzschild Phase

Let one start with the form of the gravitational background around a non-rotating, uncharged $(4+n)$-dimensional Schwarzschild black hole. The line-element described by the Schwarzschild-Tangherlini [113] is given by

$$ds^2 = -\left[1 - \left(\frac{r_H}{r}\right)^{n+1}\right]dt^2 + \left[1 - \left(\frac{r_H}{r}\right)^{n+1}\right]^{-1}dr^2 + r^2d\Omega_{2+n}^2, \qquad (4.24)$$
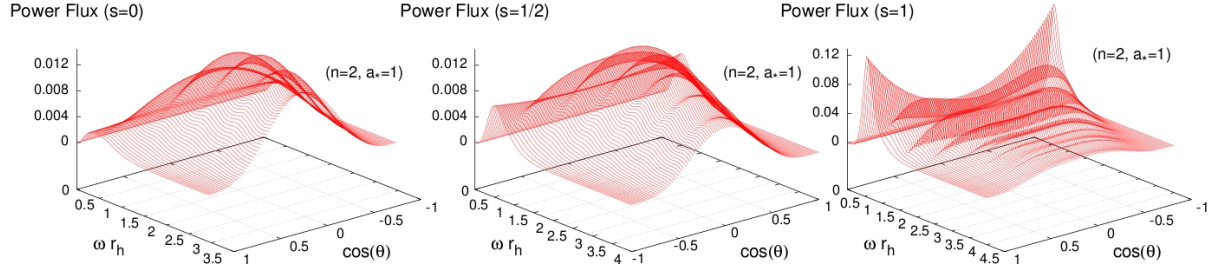
Figure 4.3: Angular distribution of the energy emission spectra for scalars (left), fermions (middle) and gauge bosons (right plot) for a 6-dimensional black hole with $a_* = 1$ [112].

where $d\Omega^2_{2+n}$ is the line-element of a $(2+n)$-dimensional unit sphere.

As in the spin-down case, for the purpose of studying the emission of Hawking radiation directly on the brane, one fixes the values of all additional coordinates introduced to describe the additional spacelike dimensions. The resulting brane background assumes the form of

$$ds^2_4 = -\left[1 - \left(\frac{r_H}{r}\right)^{n+1}\right]dt^2 + \left[1 - \left(\frac{r_H}{r}\right)^{n+1}\right]^{-1}dr^2 + r^2 d\Omega^2_2. \tag{4.25}$$

The above line-element describes a four-dimensional black hole background on the brane which, although resembling a Schwarzschild background, is distinctly different as it carries a non-trivial n-dependence. The horizon radius is given again by eq. (4.5) and its temperature by eq. (4.6).

As in the previous rotating case, one is able to compute the absorption probability defined by eq. (4.20). Whereas the absorption probability is a dimensionless quantity varying between 0 and 1 (in the non-rotating case), one may make out of it a dimensionful quantity, namely the absorption cross-section, that is measured in units of the horizon area (πr^2_H) and is defined as

$$\sigma_{abs}(\omega) = \sum_l \frac{\pi r^2_H}{(\omega r_H)^2}(2l+1)|\mathcal{A}|^2. \tag{4.26}$$

In the following, let one have a brief look at the greybody factors and energy emission rates for scalar, fermion, and gauge boson fields.

Scalar Fields

Fig. 4.4 (left) shows the greybody factors for the emission of scalar fields on the brane for different values of n. For $n = 0$ and $\omega r_H \to 0$, the greybody factor assumes a non-zero value which is equal to $4\pi r_H$. This means that the greybody factor for scalar fields with a very low energy is given exactly by the area of the black hole horizon. With increasing energy, the factor soon starts oscillating around the geometrical optics limit

$\sigma_g = 27\pi r_H/4$ which corresponds to the spectrum of a black-body with an absorbing area of radius $r_c = 3\sqrt{3}r_H/2$.

If extra dimensions are present, the greybody factor starts from the same asymptotic low-energy value, for any value of n, and it again starts oscillating around a limiting high-energy value, which is always lower than the four-dimensional one. This is because the effective radius r_c depends on the dimensionality of the bulk spacetime through the metric tensor of the projected spacetime in which the particle moves. For arbitrary n, it adopts the value

$$r_c = \left(\frac{n+3}{2}\right)^{1/(n+1)} \sqrt{\frac{n+3}{n+1}} r_H.$$
(4.27)

The above quantity keeps decreasing as n increases causing the asymptotic greybody factor, $\sigma_g = \pi r_c^2$, become more and more suppressed as the number of extra dimensions projected onto the brane gets larger.

Figure 4.4: Greybody factors (right) and energy emission rates (left) for scalar emission on the brane from a $(4+n)$-dimensional black hole [116].

Computing the energy emission rate for scalar fields on the brane, one finds that the suppression of the greybody factor with n does not necessarily lead to the suppression of the emission rate itself. Fig. 4.4 (right) plots the behaviour of the differential energy emission rate in time unit dt and energy interval $d\omega$. The increase in the temperature of the black hole, and thus in its emissivity power, as n increases, overcomes the decrease in the value of the greybody factor and leads to a substantial enhancement of the energy emission rate.

Tab. 4.3 shows the total flux and power emissivities for various values of n. The relevant emissivities for different values of n have been normalized in terms of those for $n = 0$. From the entries of Tab. 4.3, one may easily see that both the flux of particles produced and the amount of energy radiated per unit time by the black hole on the brane are substantially enhanced, by orders of magnitude, as the number of extra dimensions increases.

	$n=0$	$n=1$	$n=2$	$n=3$	$n=4$	$n=5$	$n=6$	$n=7$
Flux	1.0	4.75	13.0	27.4	49.3	79.9	121	172
Power	1.0	8.94	36.0	99.8	222.0	429.0	749	1220

Table 4.3: Flux and power emissivities for scalar fields on the brane [116].

Fermion Fields

Now let one have a look at the fermion case. Computing absorption probability $|\mathcal{A}|^2$, one obtains the behaviour of the greybody factor in terms of the energy parameter ωr_H and number of extra dimensions n. The results are depicted in Fig. 4.5 (left).

At low energies, the greybody factor assumes, as in the case of scalar fields, a non-zero asymptotic value. This depends on the dimensionality of spacetime and raises with increasing n. The enhancement of $\sigma_{abs}(\omega)$ with n in the low-energy regime persists up to intermediate values of ωr_H, after which the situation is reversed: as n takes on larger values, the greybody factor becomes more and more suppressed. Fig. 4.5 (left) shows that at high energies the greybody factors for fermion fields oscillate around the same asymptotic values as for scalar fields.
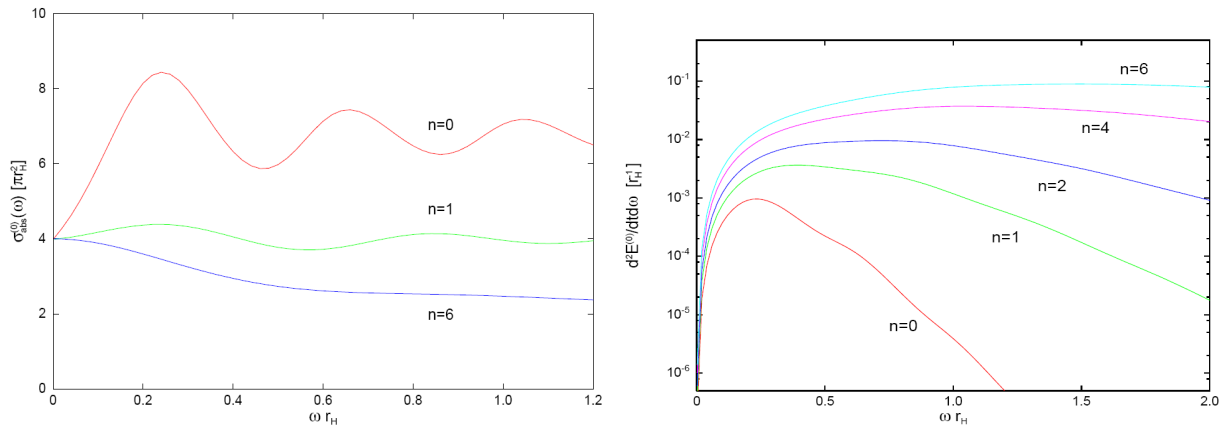

Figure 4.5: Greybody factors (right) and energy emission rates (left) for fermion emission on the brane from a $(4+n)$-dimensional black hole [116].

Fig. 4.5 (right) plots the energy emission rate for fermion fields on the brane for various values of n. As n increases, it is found to be significantly enhanced, both at low and high energies, mainly due to an increase in the temperature of the black hole. The emission curves exhibit the same features as for the emission of scalar fields, i.e. increase of the height of the peak by orders of magnitude and shift of the peak towards higher energies. Some quantitative results regarding the enhancement of both the flux and power spectra for the emission of fermions, as n increases, are given in Tab. 4.4. Once again,

the enhancement in both spectra with n is indeed substantial, and even more important compared to the one for scalar emission given in Tab. 4.3.

	$n=0$	$n=1$	$n=2$	$n=3$	$n=4$	$n=5$	$n=6$	$n=7$
Flux	1.0	9.05	27.6	58.2	103	163	240	335
Power	1.0	14.20	59.5	162.0	352	664	1140	1830

Table 4.4: Flux and power emissivities for fermions on the brane [116].

Gauge Boson Fields

Finally, the exact results for the greybody factors and energy emission rates for gauge boson fields are given in Fig. 4.6. A distinct feature of the greybody factor gauge fields is that it vanishes when $\omega r_H \to 0$. The same behaviour is observed for every value of the number of extra dimensions. This result leads to the suppression of the energy emission rate, in the low-energy regime, compared to the ones for scalar and fermion fields.
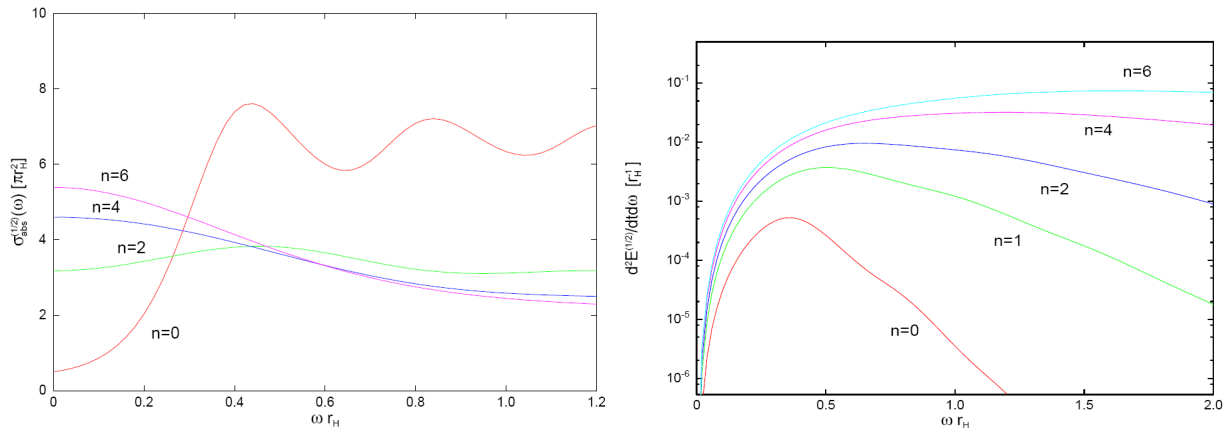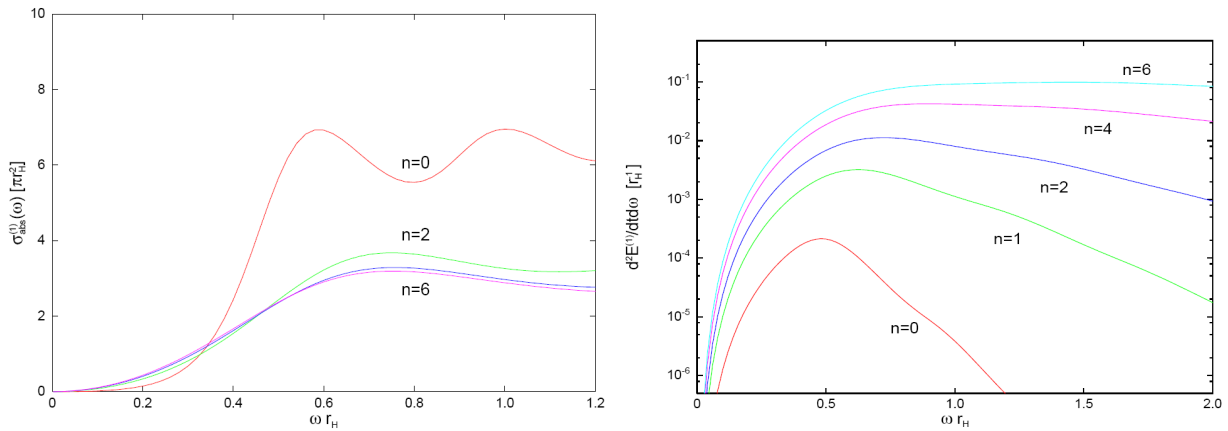

Figure 4.6: Greybody factors (right) and energy emission rates (left) for gauge boson emission on the brane from a $(4+n)$-dimensional black hole [116].

Up to intermediate energies the greybody factors exhibit the same enhancement with increasing n as in the case of fermion fields. A similar asymptotic behaviour, as in the previous cases, is observed in the high-energy regime with each greybody factor assuming, after oscillation, the geometrical optics value which decreases with increasing n. This result establishes the existence of a universal behaviour of all types of particles emitted by the black hole at high energies. This behaviour is independent of the particle spin but strongly dependent on a number of extra dimensions projected onto the brane.

Tab. 4.5 shows the total flux and power emissivities for the emission of gauge fields on the brane, in terms of the number of extra dimensions n.

	$n=0$	$n=1$	$n=2$	$n=3$	$n=4$	$n=5$	$n=6$	$n=7$
Flux	1.0	19.2	80.6	204	403	689	1070	1560
Power	1.0	27.1	144.0	441	1020	2000	3530	5740

Table 4.5: Flux and power emissivities for gauge fields on the brane [116].

Relative Emissivities for Different Species

To conclude, it would be interesting to investigate how the relative number of scalars, fermions and gauge bosons, emitted by the black hole on the brane, change as the number of extra dimensions projected onto the brane varies. In other words, to know what type of particles the black hole prefers to emit, for different values of n, and what part of the total energy each particular type of particle carries away during emission.

Fig. 4.7 shows the energy emission rates compared for different types of particles and for fixed n. As one can clearly see from Fig. 4.7 (left), in the absence of any extra dimensions, most of the energy of the black hole emitted on the brane is in the form of scalar particles, the next most important are the fermion fields, and less significant are the gauge bosons. With n increasing, the emission rates for all species are enhanced but not at the same rate. This could be seen from Fig. 4.7 (right); for a large number of extra dimensions, the most effective "channel" during the emission of brane localized modes is that of gauge bosons, the scalar and fermion fields follow second and third respectively. The change in the flux spectra, i.e. in the number of particles produced by the black hole on the brane is similar, for each species as n increases.
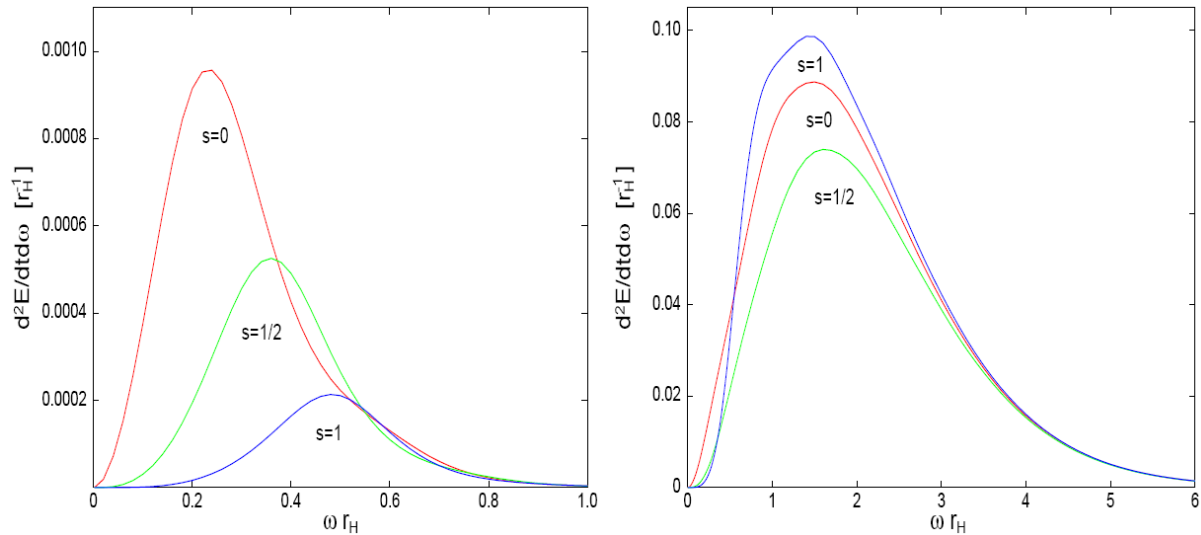
Figure 4.7: Energy emission rates for the emission of scalars, fermions and gauge bosons on the brane for $n=0$ (left) and $n=6$ (right) [116].

In order to quantify the above behaviour, Tab. 4.7 and Tab. 4.8 show the relative emissivities for scalars, fermions and gauge bosons emitted on the brane for different types of particles, over all energies. They are normalised to the scalar values.

One may thus conclude that not only the magnitude but also the type of flux and power spectra produced by a microscopic black hole strongly depends on the number of extra dimensions projected onto the brane. Therefore, upon detecting the Hawking radiation from such objects, the above distinctive feature could serve as an alternative way to determine the number of extra dimensions that exist in nature.

4.5   Hawking Radiation on Bulk

An important question would be how much energy of the emission of particles by a microscopic black hole is radiated onto the brane and how much is lost in the bulk. In the latter case all energy is in the form of gravitons and, possibly, scalar fields [114]. In the following, the emission of scalar fields and gravitons into the bulk will be briefly discussed.

4.5.1   Scalar Emission in Bulk

In this part the results for emission of scalars by non-rotating and rotating microscopic black hole will be reviewed. Detailed study for the Schwarzschild (non-rotating) phase have been done in [115] and for the rotating phase in [116] and [117].

Fig. 4.8 shows the power spectrum on the brane (left) and in the bulk (right) of non-rotating black hole for $n = 1, 2, \ldots, 6$. The total emission depends strongly on the number of bulk dimensions n. For all n, the total emission on the brane exceeds that emitted into the bulk (note the y-scales in Fig. 4.8). This happens despite the fact that particles emitted into the bulk are, on average, more energetic than those emitted on the brane.

The behaviour of energy emission rates in the bulk is shown in Fig. 4.9. According to this Figure, the emission rate of scalar fields in the bulk is enhanced as the number of extra dimensions increases. As with the emission on the brane, this is caused by the increase in the temperature of the black hole, which eventually overcomes the decrease in the value of the greybody factor and causes the enhancement of the emission rate with n at high energies.

A definite conclusion regarding the relative amount of energy which is emitted in the two "channels" - bulk and brane - can only be drawn if the corresponding total energy emissivities can be computed. The results obtained for values of n from 1 to 7 are given in Tab. 4.6. From these entries, it becomes clear that the emission of brane-localized scalar modes is indeed dominant, in terms of the energy emitted, for all values of n greater than zero and up to 7.

The key question that one seeks to address in the following is: how does the proportion of energy lost into the bulk change when the black hole is rotating? In other words, is the standard claim that black holes radiate mainly on the brane still correct in the spin-down phase of black hole evolution?
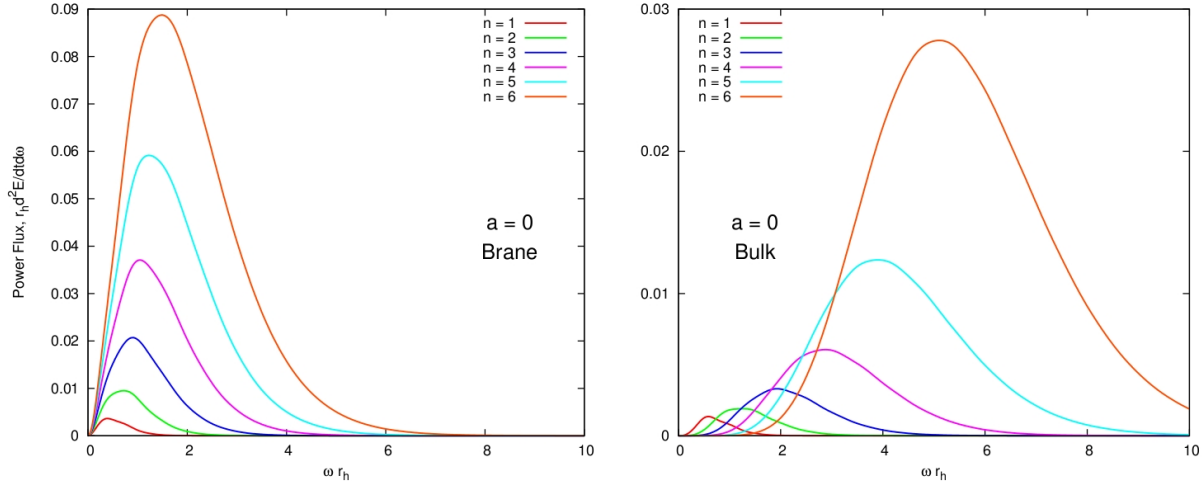
Figure 4.8: Brane and bulk emission from a non-rotating black hole. The left plot shows the power emitted on the brane, for various numbers of space-time dimensions ($n = 1, 2, \ldots, 6$). The right plot shows the power emitted into the bulk. Note the factor of 3 difference in the scales on the y-axis [115].

	$n = 0$	$n = 1$	$n = 2$	$n = 3$	$n = 4$	$n = 5$	$n = 6$	$n = 7$
Bulk/Brane	1.00	0.40	0.24	0.22	0.24	0.33	0.52	0.93

Table 4.6: Bulk-to-brane relative emissivities ratio for scalar fields in terms on n [115].

Authors in [115] tried to answer this question and several their results are shown in Fig. B.5 and Fig. B.6 (in Appendix B). The first Figure shows how rotation changes the emission spectrum of a 6-dimensional black hole both on the brane and in the bulk. The second Figure compares the emission on the brane and in the bulk at fixed $a_d = 1.0$ and for various number of extra dimensions, $n = 1, 2, \ldots, 6$.

Since the Hawking temperature decreases monotonically with $a_d = a/r_H$, and thus a rotating black hole is cooler than a non-rotating black hole, one may observe the reduction in the bulk emission. Comparing these spectra with the non-rotating cases one can conclude that the rotation reduces the proportion of the overall emission which enters the bulk. Hence, the majority of angular momentum is emitted on the brane.

4.5.2   Graviton Emission in Bulk

Graviton emissivity is highly enhanced as the spacetime dimensionality increases. Therefore, a black hole loses a significant fraction of its mass in the bulk [119], [120]. This result has important consequences for the phenomenology of black holes in models with extra dimensions and black hole detection in particle colliders.

The relative emissivities of a four-dimensional non-rotating black hole are 1, 0.37, 0.11
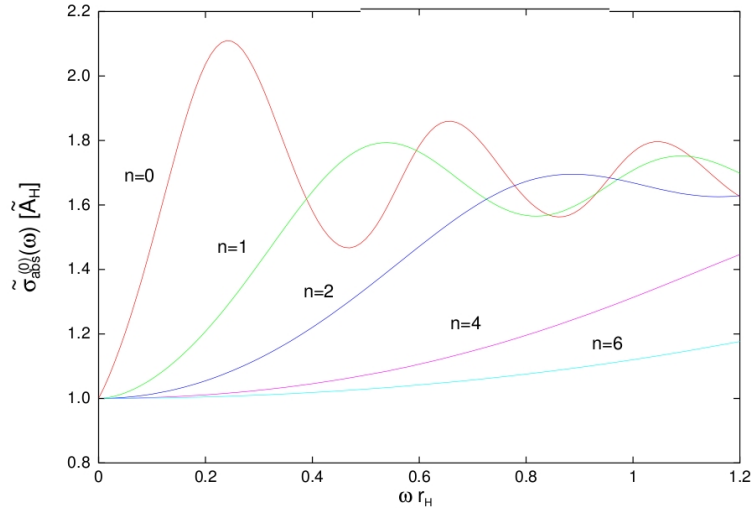
Figure 4.9: Energy emission rates for the scalar fields in the bulk from a non-rotating black hole [115].

and 0.01 for spin-0, -1/2, -1 and -2, respectively [105]. Therefore, the gravitation power loss is negligible compared to the loss on other Standard Model channels. However, in the context of additional extra dimensions, the relative graviton emission is expected to be larger.

The fraction of radiated power normalized to the scalar field is shown in Tab. 4.7 and the particle emission rates in Tab. 4.8. In four dimensions, the power loss in gravitons is negligible compared to the power loss in lower-spin fields. The graviton channel is only about 5% of the scalar channel. This conclusion is, however, reversed in higher dimensions. For instance, the gravitation loss is about 35 times higher than the scalar loss in $n = 7$. Since about 1/4 of the initial black hole mass is lost in the 11-dimensional bulk, power loss in the bulk is significant and cannot be neglected at high n.

	$n = 0$	$n = 1$	$n = 2$	$n = 3$	$n = 4$	$n = 5$	$n = 6$	$n = 7$
Scalars	1.00	1.00	1.00	1.00	1.00	1.00	1.00	1.00
Fermions	0.55	0.87	0.91	0.89	0.87	0.85	0.84	0.82
Gauge Bosons	0.23	0.69	0.91	1.00	1.04	1.06	1.06	1.07
Gravitons	0.05	0.61	1.50	2.70	4.80	8.80	17.70	34.70

Table 4.7: Fraction of radiated power normalized to the scalar field [118].

Moreover, the effect of gravitons emission may be even more dramatic when one includes rotation. Consider a rotating four-dimensional black hole studied in [105], one may conclude that graviton emission, which is suppressed for small rotation, rapidly increases

	$n=0$	$n=1$	$n=2$	$n=3$	$n=4$	$n=5$	$n=6$	$n=7$
Scalars	1.00	1.00	1.00	1.00	1.00	1.00	1.00	1.00
Fermions	0.37	0.70	0.77	0.78	0.76	0.74	0.73	0.71
Gauge Bosons	0.11	0.45	0.69	0.83	0.91	0.96	0.96	1.01
Gravitons	0.02	0.20	0.60	0.91	1.90	2.50	5.10	7.60

Table 4.8: Fraction of emission rates normalized to the scalar field [118].

with the angular momentum J. As J grows from 0 to 0.7 M^2 gravitation emissivity grows 3 orders of magnitude, while the emissivities of fermion and gauge bosons grow less than one order of magnitude. A similar behaviour is expected in higher dimensions, where for $n > 1$ there is no upper bound on J, implying that graviton emission dominates the evaporation process.

Although the emission of scalars in the bulk has been studied in detail [115], [116], [117], the emission of gravitons has received little attention. Recent studies of graviton emission in the bulk within Schwarzschild and spin-down phase could be found in [119] and [120]. It may seem from the above mentioned that the bulk graviton emission rate is sub-dominant to the one for a bulk scalar field, which in return is sub-dominant to the one for a brane scalar field. However, the exact form of the complete gravitational spectrum counting both, Schwarzschild and spin-down phase, is still pending. Therefore, a definite answer for the graviton effect on the bulk-to-brane balance remains still open.

4.6 Deducing Basic Information

The emission of particle modes on the brane is the most interesting effect since it involves Standard Model particles that can be easily detected during experiments. Nevertheless, a microscopic black hole emits also bulk modes and inevitably a proportion of the total energy is lost into the bulk.

In the above, some of black hole properties, namely, the horizon radius, temperature and lifetime were discussed. As one could see, the horizon radius of a microscopic black hole is many orders of magnitude larger than the one of a four-dimensional black hole with the same mass, which simply means that a mass needs to be compacted less in a higher-dimensional spacetime to create a microscopic black hole. On the other hand, the temperature of these microscopic black holes comes out to be lower than in four dimensions, which means that the emission rate of Hawking radiation is smaller and, therefore their lifetime is longer.

These microscopic black holes, upon implementation of quantum effects, emit Hawking radiation into the higher-dimensional spacetime in the form of both bulk and brane modes. The greybody factors encode valuable information for the background around the emitting black hole and depend on the energy of the emitted particle, its spin and the dimensionality of spacetime. This means that the presence of the greybody factor in the

radiation spectrum will cause the modification of the low-energy emission rate from the high-energy one, and will lead to different emissivities for particles with different spin.

It is expected that $\sim 75\%$ of decay products are quarks, anti quarks and gluons, while only $\sim 12\%$ are charged leptons and photons, each particle carrying hundreds GeV of energy. Therefore, the black hole decay is dominated by partons. A relatively large fraction of prompt and energetic photons, electrons, and muons expected in the high-multiplicity black hole decays would make it possible to select pure samples of black hole events, which are also easy to trigger on.

Although the possibility of the production and evaporation of microscopic black holes at the Large Hadron Collider (LHC) is an exciting prospect, this will only be possible in the cases where the fundamental scale of gravity M_* is very close to 1 TeV. Nevertheless, there is absolutely no guarantee for that, and the only argument in favour of this particular value is the possible resolution of the hierarchy problem. If M_* is larger than 1 TeV, even by one order of magnitude, the probability of the production of microscopic black holes at the LHC vanishes.

Taking into account the possibility of production of such microscopic black holes at the LHC, it should be clear that at the designed centre-of-mass energy of 14 TeV and luminosity of 10^{34} cm^{-2}s^{-1} the huge amount of data collected by the ATLAS detector has to be precisely triggered and then analysed with more than adequate software framework. Also, several additional soft collisions (pile-up) causing serious background to observed physical event are expected and, therefore, detailed analysis tools are needed to suppress these unwanted effects. In the following Chapter, the simulation of microscopic black holes within the ATLAS detector is presented. After that, the influence of pile-up will be discussed and along with previous simulated results the first data collected in 2010 are analysed.

Chapter 5

Influence of Pile-up on Microscopic Black Hole Searches

The production of microscopic black holes and their decay via the Hawking radiation at particle colliders was described in the previous Chapter. The Large Hadron Collider (LHC) has a potential of being the first experiment observing these microscopic black holes, one of the consequences of several extra-dimensional scenarios. The LHC initial physics program as well as the ultimate luminosities expected contain events with multiple simultaneous proton-proton interactions, or *pile-up*. These additional soft collisions are uncorrelated with the hard-scattering process that typically triggers the event, and therefore they present a serious background of soft diffuse radiation that not only offsets the energy measurement of jets but can impact jet shape and structure measurements.

The aim of this Chapter is to study in more detail the discovery reach for microscopic black holes at the LHC. First, ATLAS analysis tools and jet finding algorithms are briefly presented. After describing the simulation of the search for microscopic black holes in the first 100 pb^{-1} of LHC data with the ATLAS detector and software framework, pile-up events are taken into account. Optimal way to reduce pile-up or even to be able to neglect its existence is searched for and results of this along with the previous simulation are then used in the following analysis of the first LHC data collected in 2010.

5.1 ATLAS Analysis Tools

This Section briefly describes the ATLAS software framework. This framework presents a huge keystone of all physics analysis and its whole description could be found in [122]. In the following, only basics of this tool are discussed.

5.1.1 Athena Framework

In order to find interesting signals to search for new physics in the ATLAS experiment, the ATLAS software must be able to support analysis of recorded events (real data) from

the experiment as well as simulated events from a Monte Carlo event generator throughout the experiment operational lifetime. Event simulation and analysis are important to develop computer software and to tune the detector response for searches of interesting signals at ATLAS.

The ATLAS software groups provide and develop a common event processing framework, the so-called *Athena Framework*, which is based primarily on the C++ programming language with various supporting components and interfaces via Python scripts. The Athena framework is being used by the ATLAS collaboration as the main tool for data analysis.

The Athena framework has been developed from the GAUDI framework [121], which is originally developed at the LHCb experiment. The various applications and components run in the Athena framework providing flexible software to analyse all event data. The Athena framework is comprised of the algorithms (the event data processing applications), system services, and data stores. The main components of the Athena framework are shown in Fig 5.1 and their detailed description could be found in [122].
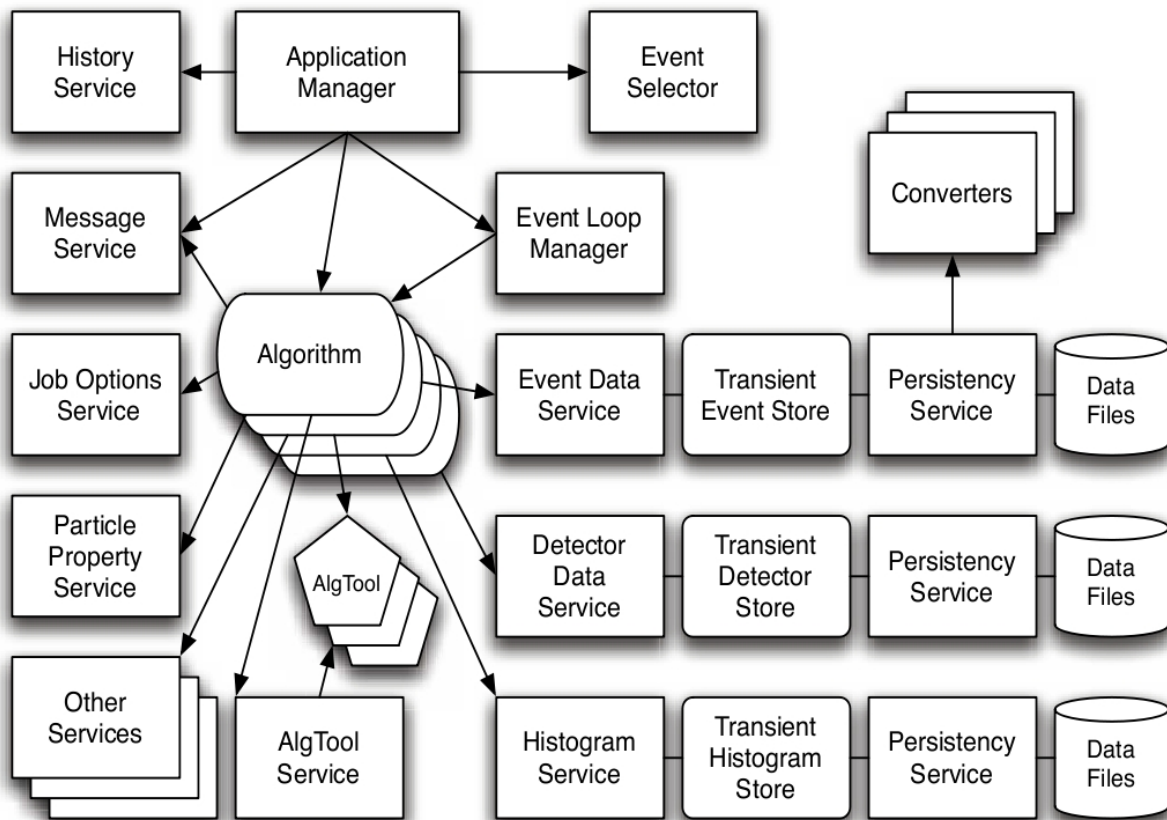

Figure 5.1: The architecture of the ATHENA framework [122].

5.1.2 Simulation Data Flow

Out of the above mentioned structure of the Athena framework, one can generate, simulate, and digitize Monte Carlo events or analyse real data from experiments. Fig. 5.2 shows the full chain of steps from generation of Monte Carlo events to production of Analysis Object Data (AOD) for further physics analysis [121], [122].
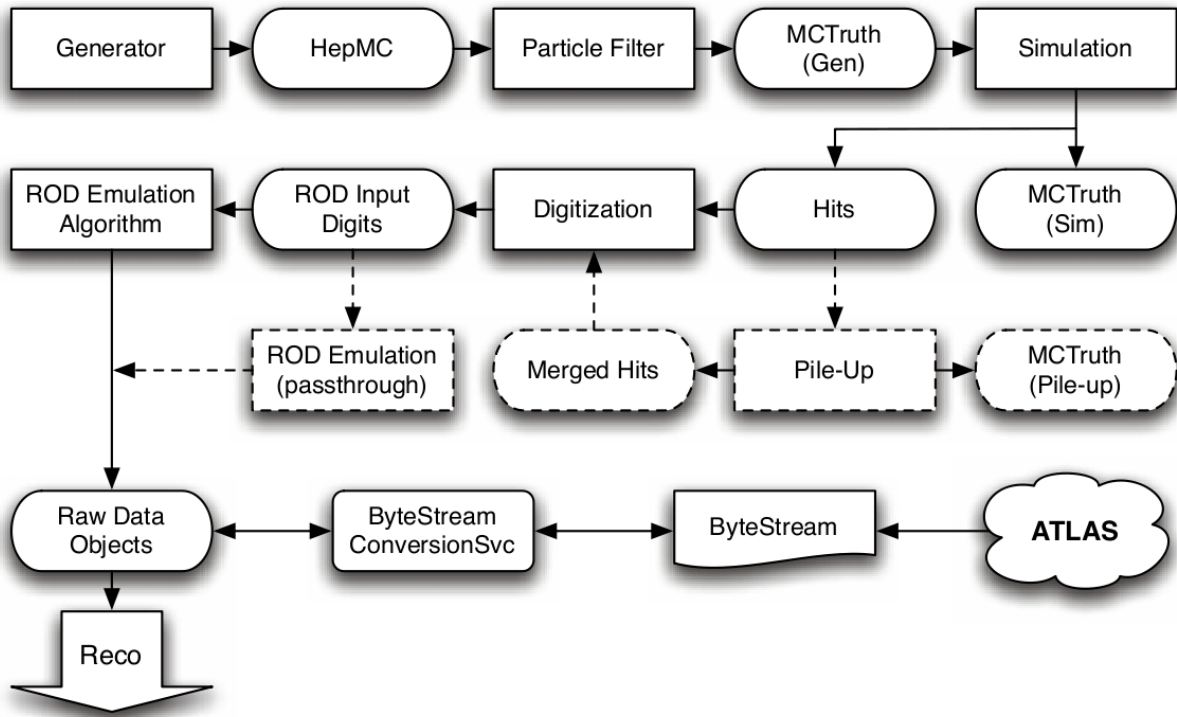

Figure 5.2: The simulation data flow. Rectangles represent processing stages and rounded rectangles represent objects within the event data model. Pile-up and ROD emulation are optional processing stages [124].

Event Generation

The generation of events is the first step of the event simulation and reconstruction in the Athena framework. Till the LHC start-up, all of the physics analysis has been done by generated events of proton-proton collision. At present, there are several popular event generators e.g., HERWIG, Pythia, Isajet, AcerMC, ComHep, AlpGen, and so on. Those generators can be run inside of Athena individually. For black hole event generation, the event generator CHARYBDIS [125] was interfaced to the HERWIG library, and then the event generator HERWIG was run in Athena to produce the black hole events. Nowadays, another black hole event generator BlackMax [126] is developed.

HepMC (High energy physics Monte Carlo)

HepMC is an object-oriented event record written in C++ for Monte Carlo event genera-
tors. Generated event data from event generation are mapped into HepMC as a common
format in the StoreGate (the ATLAS transient data store) and persistent representation.
Now the recorded events are for G4ATLAS simulation (ATLAS detector simulation pro-
grams based on Geant4) after a particle filtering.

Simulation

In recent years, efforts are being made on improving the Geant4 simulation in order to
provide the modeling of hadronic physics processes. Geant4 toolkits allow physicists to
build the virtual ATLAS detector with specific description of materials and to demonstrate
the propagation of the particles in a framework environment. The G4ATLAS counts out
hits, which have energy deposition, position, identifier, and active elements information.
It has also been embodied in Athena for detector simulation since 2003.

Digitization

G4ATLAS simulates physics processes in the ATLAS detector, so it reads out the hits which
include energy, position, and interaction information. The produced hits will response to
the readout electronics and the propagation of charges or light into the media. Thus, the
stage of digitization requires detailed detector knowledge to build up. At the end of this
step, the digitization step will produce Raw Data Objects (RDOs) which pass the event
filter of the high-level trigger for reconstruction. The RDOs are similar to the real detector
data. The most important role of this step is that one can compare the RDO output to
real data to test the detector's response for the real experiment.

Reconstruction

Reconstruction from simulated data is an important process. Reconstruction plays the
role of deriving particle parameter and information for physical objects such as muons,
electrons, photons, tau-leptons, jets, missing transverse energy, and primary vertex.

Several different types of datasets, corresponding to different stages of reconstruction,
are produced. Besides *Byte-stream Data* which is a persistent presentation of the event
data flowing from the HLT, and above mentioned RDO, the following datasets are also
available [122], [123]:

- *Event Summary Data* (ESD) which contains the detailed output of the detector
  reconstruction and is produced from the raw data. ESD presents a perfect tool for
  tuning of reconstruction algorithms and calibrations of the ATLAS experiment for
  real data.

- *Analysis Object Data* (AOD) which is a summary of the reconstructed event, and
  contains sufficient information for common analyses. The size of the AOD is much

smaller than the ESD files. The black hole analysis is performed on standard AOD files. From the AOD files, one can process the additional step for the event tags on the AOD.

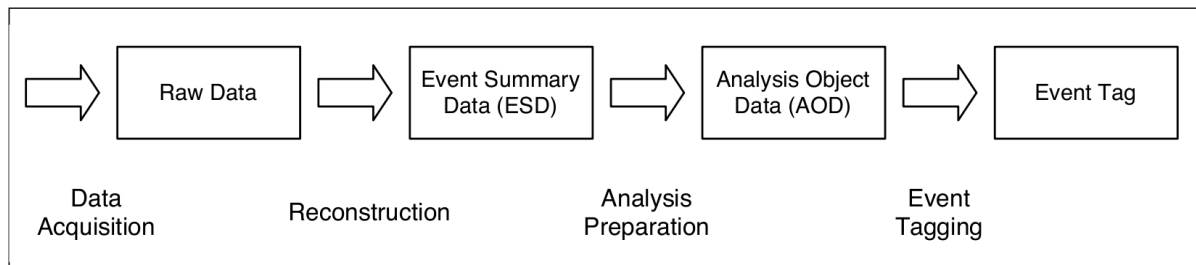The reconstruction processing pipeline is summarized in Fig. 5.3.

Figure 5.3: The reconstruction processing pipeline [122].

5.2   Jet Reconstruction Performance

Almost all physics analyses performed with the ATLAS experiment require high quality and highly efficient jet reconstruction. Microscopic black hole analysis presents no exception since the final decay state consists of about 75 % of quarks and gluons. The principal part of the ATLAS detector for jet reconstruction is the ATLAS calorimeter system, which provides near hermetic coverage in a pseudorapidity range $-4.9 < \eta < 4.9$. Its basic components are depicted in Fig. 2.4 with a brief description in Section 2.3.

Jet Algorithms in ATLAS

Relevant jet finding algorithms currently in use within the ATLAS experiment include fixed sized cone algorithms as well as sequential recombination algorithms and an algorithm based on event shape analysis. In fact, there is no universal jet finder for the hadronic final state in all topologies of interest since different final states prefer different, narrower or wider, jets to capture all particle signs needed.

Nevertheless, in spite of different technique within jet finding, the common feature of all jet finder implementations in ATLAS is full four-momentum recombination whenever the constituents of a jet change, either through adding a new constituent, or by removing one, or by changing the kinematic contribution of a given constituent to the jet. Moreover, the same jet finder code can be run on objects like calorimeter signal towers, topological cell clusters in the calorimeters, reconstructed tracks, and generated particles and partons in the ATLAS reconstruction framework software Athena.

The major guidelines for jet reconstruction in ATLAS also reflecting the concept of *jet definition* discussed in [128] are:

Infrared safety: The presence of additional soft particles between two particles belonging to the same jet should not affect the recombination of these two particles into a jet. In the same way, the absence of additional particles between these two should not disturb the correct reconstruction of the jet. Generally, any soft particles not coming from the fragmentation of a hard scattered parton should not effect the number of jets produced.

Collinear safety: A jet should be reconstructed independently from the fact that a certain amount of transverse momentum is carried by one particle, or if a particle is split into two collinear particles. An example of collinear safety is shown in Fig. 5.4.
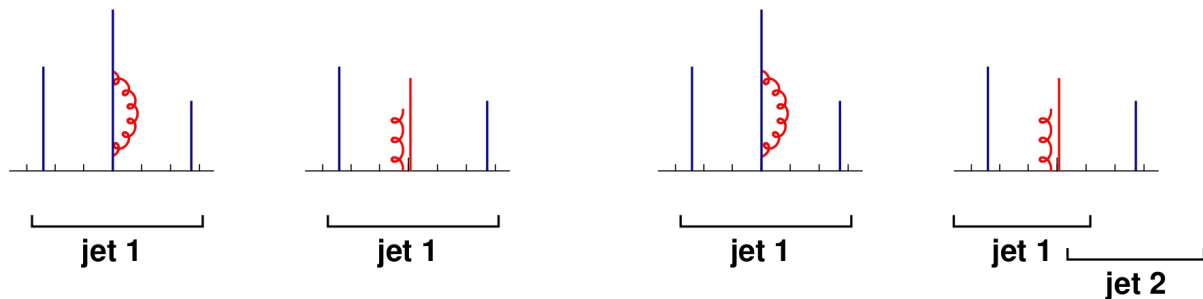
Figure 5.4: Collinear safe (on the left) and collinear unsafe (on the right) example of jet reconstruction [129].

Also, the reconstructed jet and its kinematics should not depend on the signal source. This means that all detector specific signal characteristics and inefficiencies must be calibrated out or corrected as much as possible. Moreover, one has to keep in mind that the jet reconstruction environment is characterized by the additional activity in the collision event due to multiple interactions and pile-up, the source of the jet, the underlying event activity, and other features of the pp collisions at the Large Hadron Collider.

A seeded fixed cone finder with split and merge, and a k_T algorithm present the most commonly used jet finder implementation in ATLAS.

Fixed Cone Jet Finder in ATLAS

The seeded cone algorithm uses two parameters, the transverse momentum, p_T, for a seed, and the cone size $\Delta R = \sqrt{\Delta\eta^2 + \Delta\phi^2}$, with η as pseudorapidity and ϕ azimuth.

The algorithm method is as follows: first, all input is ordered in decreasing order on transverse momentum p_T. If the object with the highest p_T is above the seed threshold, all objects within a cone $\Delta R < R_{cone}$, where R_{cone} is the fixed radius, are combined with the seed. Taking the four-momenta inside the initial cone a new direction is calculated and, therefore, a new cone is centered around it. After that, objects are recollected in this new cone and the direction is updated again. These iteration steps continue till the direction of the cone does not change anymore after recombination, at which point the cone is

considered stable and is called a *jet*. The iterative process above mentioned is then applied at the next seed taken from the input list and a new cone jet is formed. This continues until no more seeds are available.

Nevertheless, a disadvantage of this method is that jets found this way may share constituents, and signal objects contributing to the cone at some iteration maybe lost again due to the recalculation of the direction at a later iteration. Even though this algorithm is not infrared safe, it can be (at least) partly recovered by introducing a split an merge step after the jet formation is done. If jets share constituents with more than certain fraction of the p_T (~ 50 %) of the less energetic jet they are merged. On the other hand, they are split if the amount of shared p_T is below this fraction. To conclude, the parameters of the ATLAS cone jet finder are a seed threshold of $p_T > 1$ GeV, and narrow ($R_{cone} = 0.4$) and a wide ($R_{cone} = 0.7$) cone jet option.

Sequential Recombination Algorithms

A sequential recombination jet finder in ATLAS is the k_T algorithm. Taking ij as pairs of input objects (partons, particles, reconstructed detector objects with four-momentum representation) they are analysed with respect to their relative transverse momentum squared, given by

$$d_{ij} = \min(p_{T,i}^2, p_{T,j}^2)\frac{\Delta R_{ij}^2}{R^2} = \min(p_{T,i}^2, p_{T,j}^2)\frac{\Delta \eta_{ij}^2 + \Delta \phi_{ij}^2}{R^2}, \qquad (5.1)$$

and the squared p_T of object i relative to the beam $d_i = p_{T,i}^2$. Taking the minimum d_{min} of all d_{ij} and d_i to be found, two possibilities follow. If d_{min} is a d_{ij}, then the corresponding objects i and j are combined into a new object k using four-momentum recombination. After that, both objects are removed from the list and the new object k is added to it. On the other hand, if d_{ij} is a d_i, the object i is considered to be a jet by itself and removed from the list.

At the end of this repeating procedure all objects are removed from the list and all original input objects end up to be either part of a jet or to be jets themselves. Contrary to the cone algorithm, no objects are shared between jets. The k_T procedure is infrared and also collinear safe. Default configurations of the distance parameter R in ATLAS are $R = 0.4$ for narrow and $R = 0.6$ for wide jets.

Fig. 5.5 and Fig. 5.6 show the difficulties of choosing the best jet radius. For example, in Fig. 5.5 the large jet radius is better for the case of non-perturbative and perturbative fragmentation, whereas the smaller radius is more useful in the case of underlying events and pile-up noise. Fig. 5.6 shows an example of multi-hard-parton events.

It should be pointed out that finding jets in reconstructed inner detector tracks could be useful to recover possible inefficiencies of the calorimeter signals. As already mentioned, jet finders usually cluster four-momentum in two dimensions, η and ϕ. With inner detector, the z coordinate can be added as a third dimension to jet finding. Jet clustering in η, ϕ, and
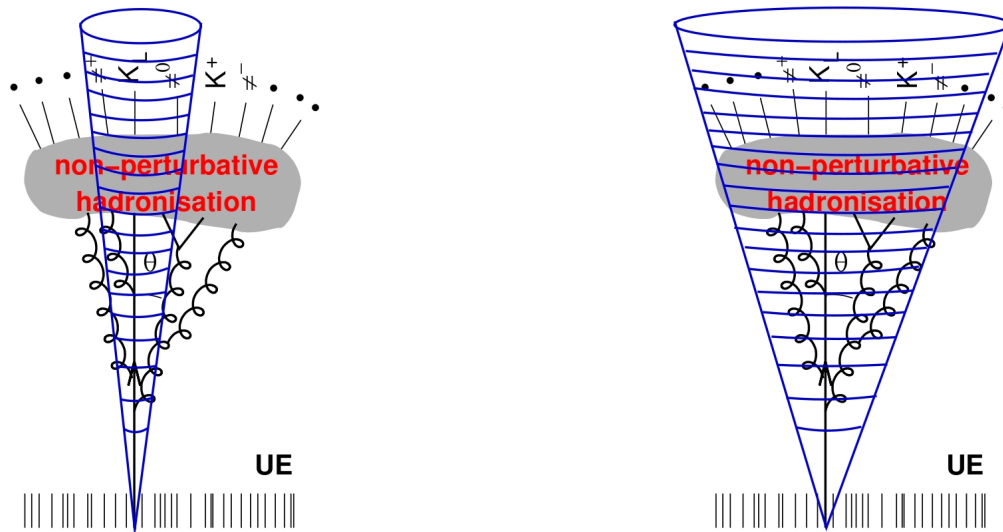
Figure 5.5: Small (on the left) and large (on the right) jet radius in the case of of non-perturbative and perturbative fragmentation (the larger jet radius is better) and, contrary, in the case of underlying events and pile-up noise, where the smaller jet radius is more useful [129].

z then allows the assignment of a vertex to a matching calorimeter jet, which is especially of interest in events with multiple interactions from pile-up.

5.3   Discovery Reach for Microscopic Black Holes

In the following analysis of microscopic black hole simulation, the details of horizon formation, and the balding and spin-down phases had been ignored. The effects of angular momentum in the production and decay of the microscopic black hole in extra dimensions are not accounted for in the Monte Carlo event generator. Only the Hawking evaporation phase is generated by the simulation.

Gravitons have not been included in the simulation, which is another drawback of this analysis. The microscopic black hole may lose a significant fraction of its mass into the bulk, resulting in missing transverse energy. Moreover, the decay is performed totally to Standard Model particles and no stable exotic remnants survive. Another suggestion is that the baryon number, colour and electric charge are conserved in the microscopic black hole production and decay.

The aim of this part is to simulate the search for microscopic black holes in the first 100 pb^{-1} of Large Hadron Collider data with the ATLAS detector and software framework. An example of a simulated microscopic black hole event viewed in ATLAS detector is shown in Fig. 5.7.
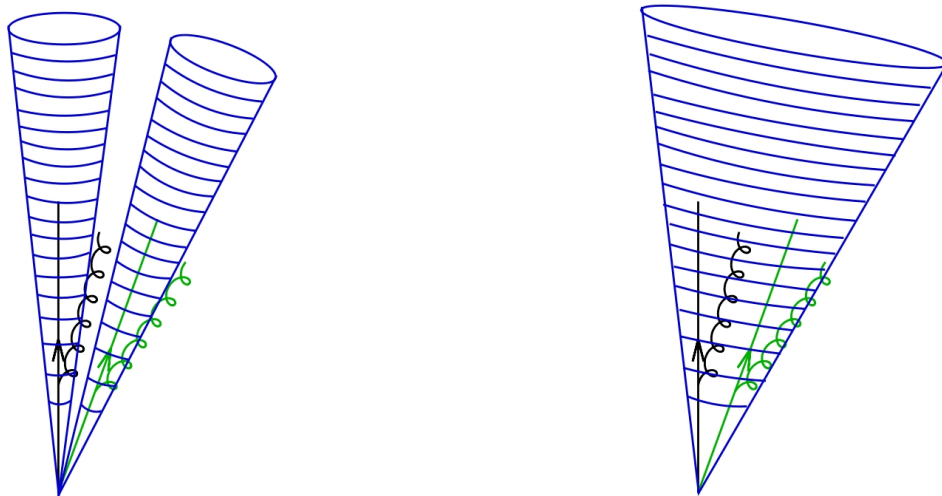
Figure 5.6: An example of multi-hard-parton events with a small (on the left) and large (on the right) jet radius [129].

5.3.1 Production of Signal and Background Events

The event generator CHARYBDIS [125] is used within the ATLAS software framework to generate Monte Carlo signal samples. CHARYBDIS is an event generator simulating the production and decay of black holes at hadronic colliders. It interfaces via the Les Houches accord [127] to general purpose Monte Carlo programs like Herwig and Pythia which then perform the parton evolution and hadronization.

Most notable feature of the CHARYBDIS generator is that unlike other generators the greybody effects are fully included. Also, it allows the black hole temperature to vary as the decay progresses and is designed for simulation with either pp or $p\bar{p}$ collisions.

Since the balding phase of the black hole decay is difficult to model and due to the lack of the full theory of quantum gravity to explain the Planck phase of the decay, the generator only attempts to model the Hawking evaporation phase. Also, only non-spinning black holes are considered and modelled and, as mentioned above, even though black hole decay may not conserve baryon number, CHARYBDIS conserves it during black hole production and decay. The default CHARYBDIS parameters used are summarized in Tab. C.1 (in Appendix C).

It is supposed that black holes decay democratically to all particles of the Standard Model. Therefore, few Standard Model processes should produce the same particle spectrum. Black hole decays are characterised by a number of high energy and transverse momentum objects, so the primary Standard Model backgrounds are states with high multiplicity or high energy jets. The predominant backgrounds to simulated signal and their cross-sections are listed in Tab. 5.1.
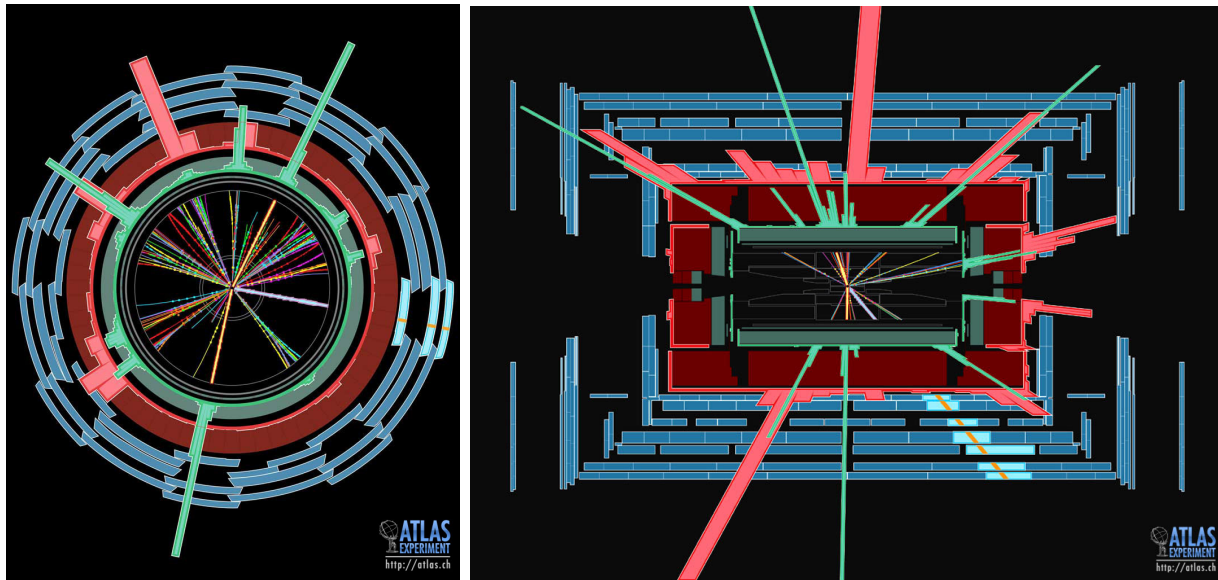
Figure 5.7: A simulated microscopic black hole event viewed in ATLAS detector along the beampipe (on the left) and from the side (on the right). The black area in the center with many particle tracks represents the inner detector, which has been enormously magnified relative to the rest of the detector (in this view). The green area is the electromagnetic calorimeter, while the red area is the hadronic calorimeter. The green and red histograms show the energy deposits by particles in the electromagnetic and hadronic calorimeters. The blue area presents muon chambers [130].

5.3.2   Event Properties

Black hole events are characterized by large number of high-p_T final state particles, including all Standard Model fields. Even though the graviton emission is also expected, it is not simulated in CHARYBDIS. Final decay state consisting of jets, electrons, muons, photos, and the W and Z bosons as well can be detected. The missing energy due to the neutrino escaping and graviton emission can be also measured.

Fig. 5.8 shows the types of particles produced directly by black hole decay. On the vertical axis the average number of particles per black hole decay is shown. It could be seen that a heavier black hole has more decay products[1].

Fig. 5.9 shows p_T and pseudorapidity (η) distributions of particles produced directly from black hole decays. As can be seen, many particles emitted in black hole decay have high p_T. This allows reliable trigger of such events. The Hawking temperature is higher for larger number of extra dimensions n (see eq. (4.6) or Tab. 4.2 in Chapter 4). This fact plays a key feature of the black hole decays. Higher temperature produces higher energy

---

[1]The particle-antiparticle balance is broken by the initial state of two protons colliding. Moreover, due to conservation of energy and momentum, colour connection etc., a perfect democratic decay cannot be achieved, e.g., the number of top quarks is smaller than that of lighter quarks.

Process	σ [pb]
Semi/Fully Leptonic $t\bar{t}$	463
Hadronic $t\bar{t}$	370
QCD di-jets	12.84×10^3
$W \rightarrow e\nu_e$ + jets	281
$W \rightarrow \mu\nu_\mu$ + jets	279
$Z \rightarrow ee$ + jets	25.8
$Z \rightarrow \mu\mu$ + jets	26.0
γ + jets	5.00×10^3
$\gamma\gamma$ + jets	67.6

Table 5.1: Background Monte Carlo datasets and their cross-sections [131].

emission, with the consequence that the energy is shared between fewer particles. This has a significant effect on the multiplicity and event shape distributions (see Fig. 5.10).

One may expect that black hole events would be very different from the background in event shape variables such as sphericity, because of the high multiplicity thermal decay. Nevertheless, such variables are less useful than one could hope for since the event shape of the black hole events varies considerably with n. Moreover, an ignorance of the decay modes of the final black hole remnant introduces a significant systematic.

5.3.3 Signal Selection and Background Rejection

As mentioned before, black hole decay consists of all Standard Model particles. Identification of objects (electrons, muons, photons and jets) might be sometimes ambiguous, for example, an electron could be simultaneously reconstructed as a jet. Therefore, to resolve this, an application of particle identification information (PID) to every object, selecting muons, electrons, photons and jets in that order of priority is used. The objects selection criteria are, among others, as follows: muons with $|\eta| < 2.5$ and $p_T > 15$ GeV, electrons with $|\eta| < 2.5$ (except for $1.00 < |\eta| < 1.15$, $1.37 < |\eta| < 1.52$) and $p_T > 15$ GeV, photons with $|\eta| < 2.5$ and $p_T > 15$ GeV, and, finally, jets with cone algorithm ($R = 0.4$) with $|\eta| < 2.5$ and $p_T > 20$ GeV.

Next step is to select black hole events using these objects and then a black hole reconstruction from all the selected objects for the selected event. Using the four-momenta of the reconstructed final state objects and missing E_T one may finally calculate the mass of the black hole in the event. Two methods to select black hole can be used: based on the scalar summation of p_T or on the multiplicity of high-p_T objects. Furthermore, a high-p_T lepton are required to reject backgrounds.

Fig. 5.11 shows the scalar summation of the p_T of each object, $\sum |p_T|$, which demonstrates good background discrimination and high signal efficiency for all black hole samples. Two event selections above mentioned are studied. In first, $\sum |p_T| > 2.5$ TeV and at least
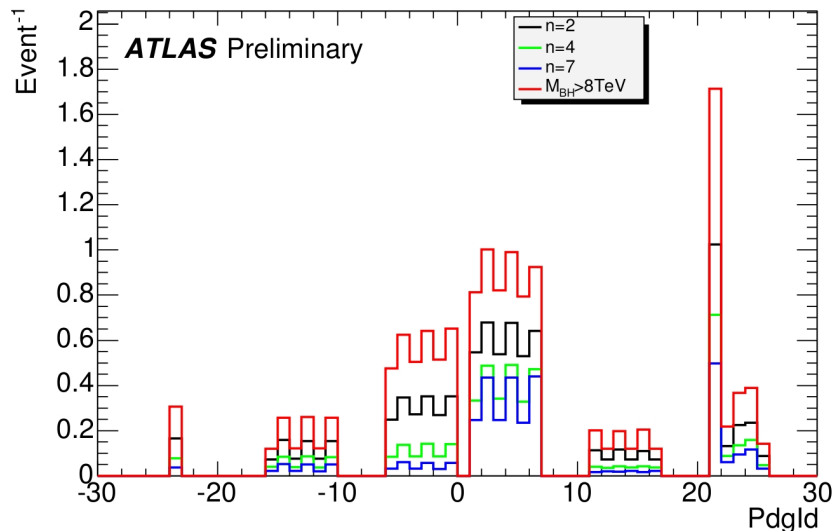
Figure 5.8: PDG code of particles emitted from black hole decay for a minimum black hole mass of 5 TeV with $n = 2$, 4 and 7, and for a minimum black hole mass of 8 TeV and $n = 2$ ($|\text{PdgId}| = 1 - 6$ are quarks, $11 - 16$ leptons, and $21 - 25$ gauge and Higgs bosons). The vertical axis shows multiplicity per black hole decay [131].

one of 50 GeV lepton (electron or muon) are required. The requirement of high-p_T lepton especially suppresses QCD multi-jet processes by a factor greater than 10^6. Second event selection requires at least four objects with $p_T > 200$ GeV, of which one or more is a lepton. The two event selections result in approximately the same efficiency and suppression of background. The first one is shown in Fig. 5.12, the second is plotted on Fig. 5.13.

5.3.4 Search Reach for Microscopic Black Holes Production

To conclude this part, above simulation shows that the ATLAS detector is capable of discovering the production of black holes up to kinematic limit of the Large Hadron Collider (LHC), in the case that the signal is correctly simulated. 5 TeV black holes would then be discovered with only a few pb^{-1} of data, while a 1 fb^{-1} of data would allow the discovery of black holes with a threshold of 8 TeV. The discovery potential of black holes for two methods above considered is shown in Fig. D.1 and Fig. D.2 (in Appendix D).

Nevertheless, several assumptions done in the above simulation may have a crucial effect on systematic uncertainties and, therefore, on detailed search reach limits too. An example could be a temperature variation, which is normally allowed to increase as the black hole mass decreases, as expected if the black hole has time to equilibrate between the decays. However, another point of view could be to keep the temperature fixed at the initial value, as would be the case if the black hole decays very quickly or "suddenly". Another effect may results from the Planck scale, which could be different. The question of final remnant decay is still open as well, etc.
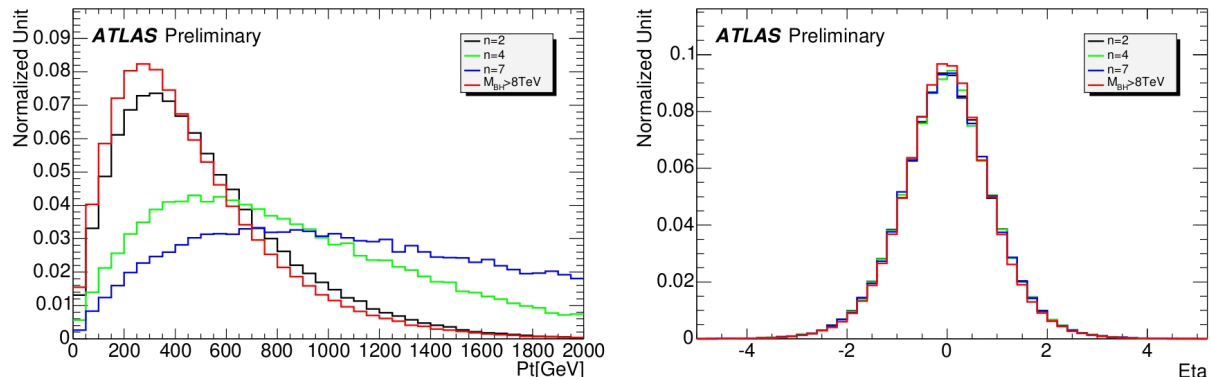
Figure 5.9: Generator p_T distributions (on the left) and η spectra (on the right) for all particles emitted from the black hole [131].
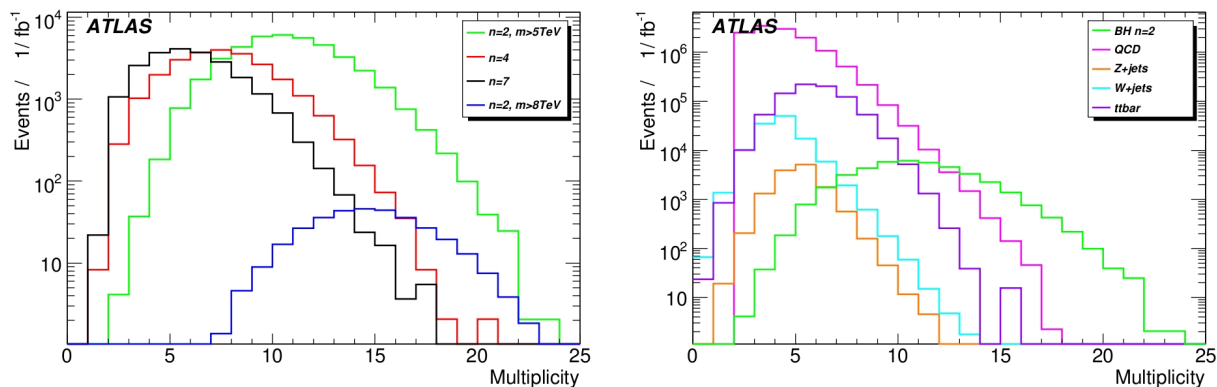

Figure 5.10: Multiplicities of reconstructed objects for the black hole samples (on the left) and backgrounds (on the right) [131].

Also, in this simulation no pile-up effects have been taken into account. The LHC will produce several relevant pile-up events, which may significantly modify results from physics analyses. These effects are discussed in the following Section.

5.4   Pile-up Studies on Jet Production

As mentioned before, hard-scattering events containing jets from additional interactions pose challenges for jet and missing transverse energy reconstruction, scale, and resolution. At the designed luminosity of 10^{34} cm^{-2}s^{-1} of the Large Hadron Collider (LHC), the average number of minimum-bias events is about 23 per bunch crossing. Therefore, any collision recorded in the ATLAS detector contains a superposition of particles coming from several events. The hits from other uninteresting interactions are not related to the physics event and present a serious background.
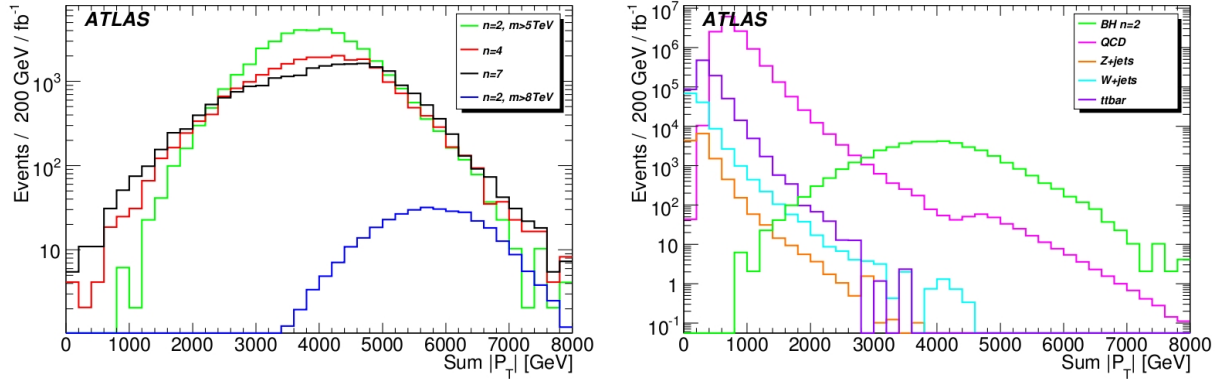
Figure 5.11: $\sum |p_T|$ distributions for the black hole samples (on the left) and backgrounds (on the right) along with one signal sample for reference [131].
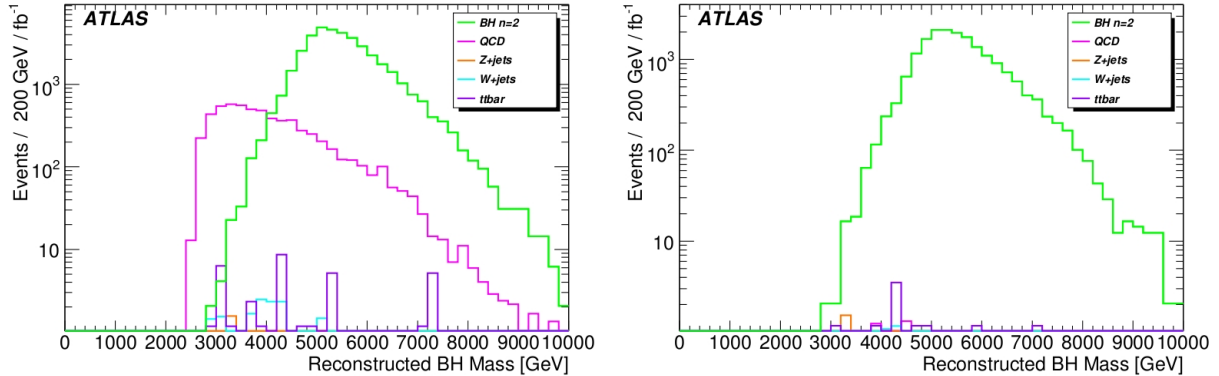

Figure 5.12: Black hole mass distribution with a requirement $\sum |p_T| > 2.5$ TeV (on the left), and black hole mass distribution with an additional requirement on the lepton with $p_T > 50$ GeV (on the right) [131].

5.4.1   Pile-up Events at ATLAS

Since pile-up originates from an interaction other than the hard-scattering event which triggers the readout, it consists primarily of two components: in-time pile-up and out-of-time pile-up. The first one refers to multiple pp interactions occurring simultaneously within a single event. On the other hand, the second one refers to contributions of previous bunch-crossings due to relatively large calorimeter integration time. With the LHC luminosity increasing or the bunch charge raising (even for low luminosities), both of these effects influence the detector response.

An example of a QCD di-jet hard-scattering assuming the LHC center-of-mass energy of $\sqrt{s} = 14$ TeV and a bunch spacing of 25 ns is shown in Fig. 5.14 both with and without additional overlaid pile-up interactions. As can be seen, not only the number of calorimeter energy depositions increases but the jet topology of the event changes. After adding pile-up, the second leading jet in the case of no pile-up becomes the leading jet.
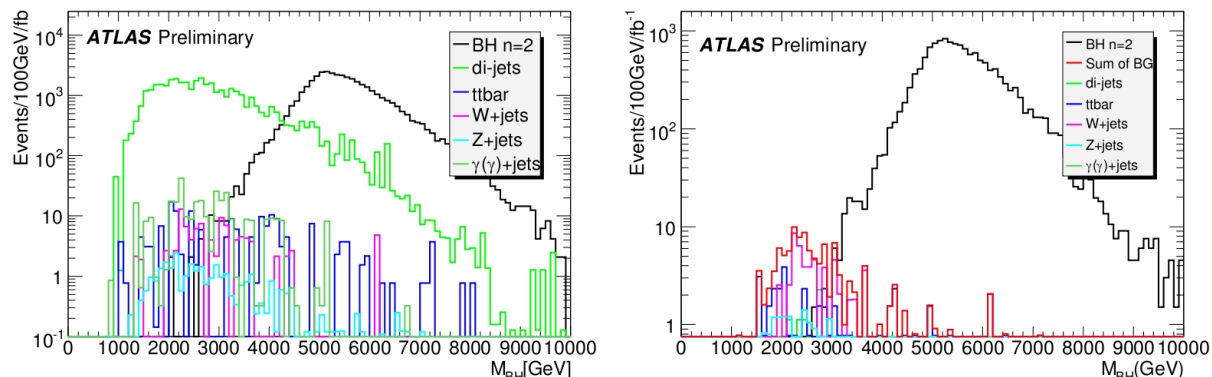
Figure 5.13: Black hole mass distribution after multiplicity cut of at least four objects with $p_T > 200$ GeV (on the left) and an additional requirement of a lepton (electron or muon) with $p_T > 200$ GeV (on the right) [131].

To simulate the effect of pile-up, one has to overlay additional interactions into a given signal event during the simulation of the digitization. These events may be simulated independently, but necessarily with the same detector geometry. The overlaid events may include minimum bias interactions as well as cavern background with a configurable bunch spacing.

As pointed out before, the ATLAS inner detector provides a precise tool for understanding the composition of calorimeter jets and for reducing this background. Instead of usual η and ϕ coordinates, one has a three-dimensional information (η, ϕ and z) on the jet origin and direction as a result of the vertexing provided by the tracks. This combination of inner detector and calorimeter may therefore greatly enhance the identification and selection of jets.

The above tool on the jet selection is introduced in the so-called *jet-vertex fraction* method [132]. This method presents a new algorithm for jet-identification and jet-energy scale correction in events with multiple interactions and one can differentiate between jets from minimum bias interactions and from the hard-scattering interaction.

5.4.2 Monte Carlo Samples and Event Topology

From the above mentioned, one can summarise the influence of pile-up, secondary interactions in the collision event, into two main effects:

- Pile-up adds additional energy to jets. The primary collision may produce (for example) two primary jets, but there are additional interactions with low energy tracks and energy deposits. If they are in the same place as one of the primary jets, it will have a slightly higher energy.

- Additional interactions may produce soft (low-p_T) jets. If the jet p_T cut is low enough,
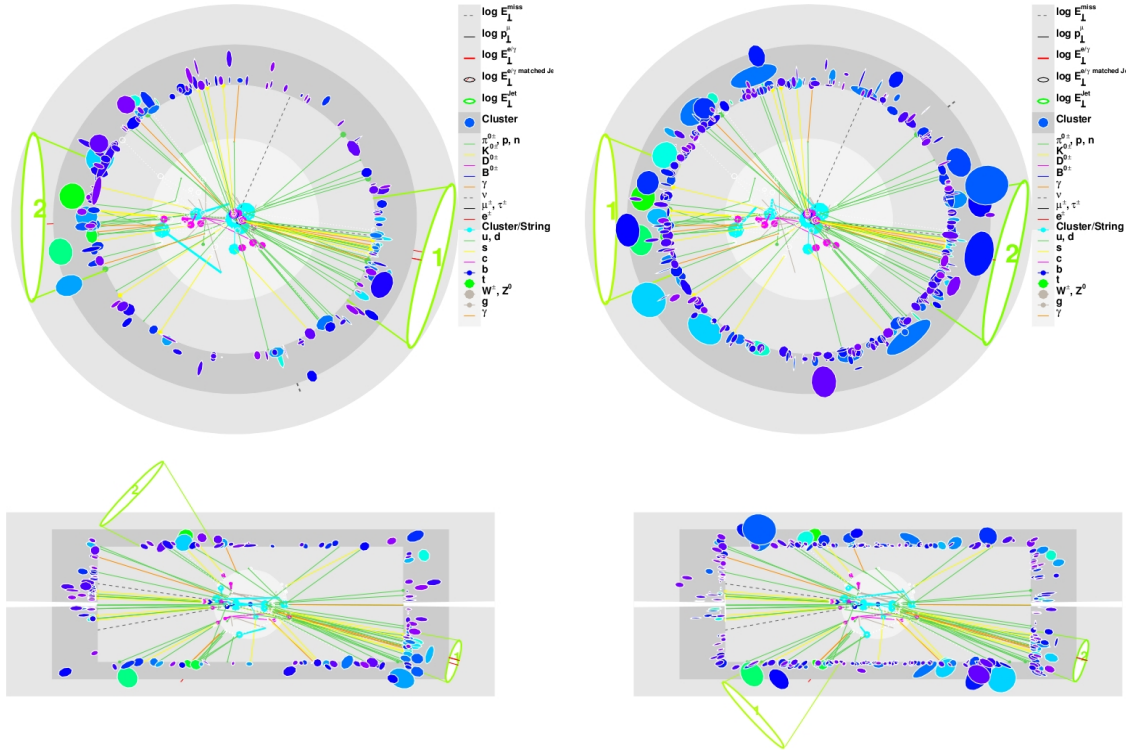
Figure 5.14: Event display of a single simulated QCD di-jet event with and without accompanying pile-up. $(R - \varphi)$ view on the top row and $(R - z)$ view on the bottom of di-jet event without pile-up (left) and with pile-up at 2×10^{33} cm^{-1}s^{-1} (right) [132].

one may see more jets in pile-up events, because these secondary jets are also counted for in the analysis.

To study the influence of pile-up events several 7 TeV and 14 TeV datasets are analysed. These datasets have all been centrally produced in the ATLAS production system and reconstructed using different Athena Releases with details listed in Tab. E.1 (in Appendix E). The aim of this study is to find optimal jet η and p_T cuts to reduce pile-up effects.

The 7 TeV datasets are a di-jet samples - events consisting primarily of two back-to-back jets (in the $x - y$ plane perpendicular to the beam pipe) - with a particular p_T range of $70 - 140$ GeV. One can see this in the jet p_T distribution (Fig. 5.15), there are some soft jets, then the distribution falls a little, and after that there is a small peak at 70 GeV, due to the requirements for an event to fall into this sample. The 14 TeV datasets contain $t\bar{t}$ events. All following histograms are normalized to unity (NU).

After the first preselection, several cuts on jets are estimated for jet η 2.8 and 5.0, and for jet p_T 20, 40 and 60 GeV cuts. First, let one have a look at jet η cut. Fig. 5.15 shows several distributions with different jet η cut ($|\eta| < 2.8$ and $|\eta| < 5.0$) and jet $p_T > 20$ GeV

Figure 5.15: Histograms of 7 TeV data samples to find optimal jet η cut. The top row: the invariant mass of all objects (on the left) and the number of jets distribution (on the right). On the bottom: the jet p_T (on the left) and the $\sum p_T$ distribution of all objects (on the right). Cuts applied for all histograms are jet $p_T > 20$ GeV and jet $|\eta| < 2.8$ (blue) or $|\eta| < 5.0$ (red).

for the 7 TeV data samples. The first histogram shows the distribution of the invariant mass of all objects in data samples used. The second one plots the number of jets in events passing through the above selection, the jet p_T distribution is shown in the third plot and the last one depicts $\sum p_T$ of all objects.

Fig. 5.16 shows the same but for the 14 TeV samples. Comparing both Figures, one can note that in the case of centre-of-mass energy of 7 TeV the difference of the distribution shape among events with and without pile-up is not as significant as in the case of 14 TeV. One can also see the influence of additional interactions producing low-p_T jets on the jet distributions, especially clearly seen in the number of jets distribution in Fig. 5.16. In the case of pile-up events, additional low-p_T jets occur and cause a long tail of distribution to the large number of jets. These additional low-p_T jets could be clearly seen in the p_T distribution of the same Figure as well.

These distributions in the cases of jet $p_T > 40$ GeV and $p_T > 60$ GeV are plotted on Fig. F.1 and Fig. F.2 for the 7 TeV samples and for the 14 TeV samples in Fig. F.3 and
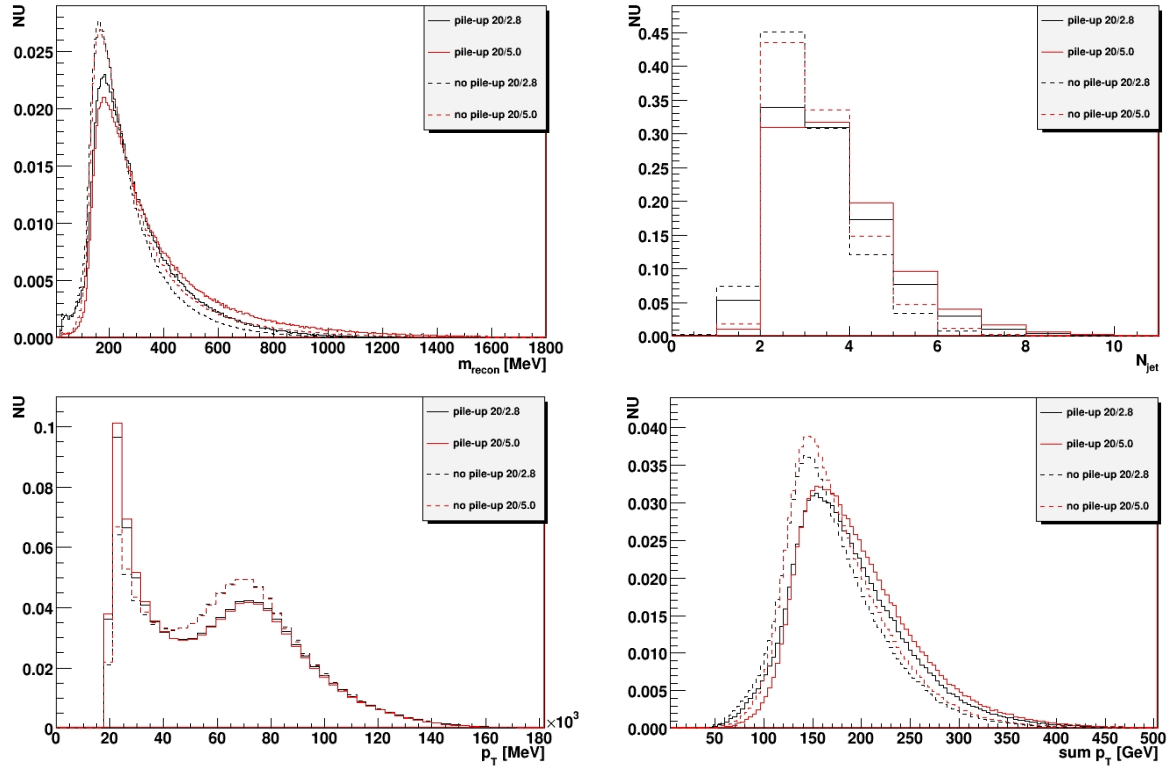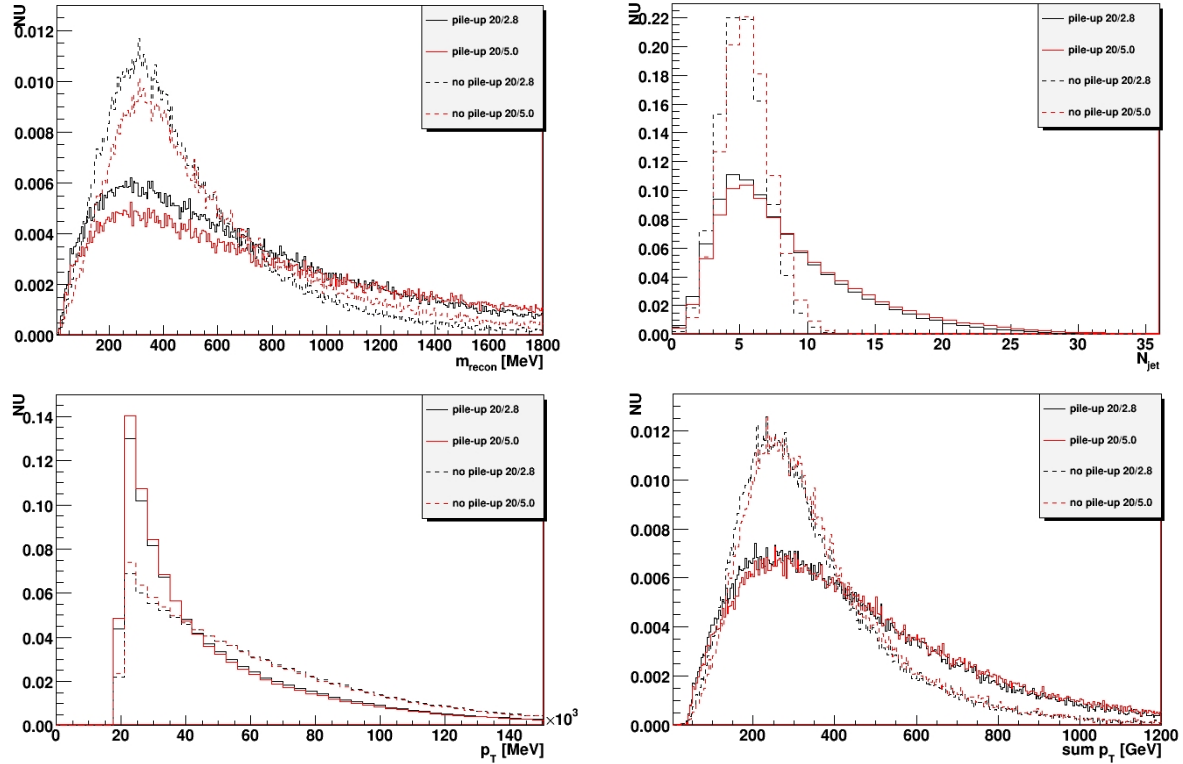
Figure 5.16: Histograms of 14 TeV data samples to find optimal jet η cut. The top row: the invariant mass of all objects (on the left) and the number of jets distribution (on the right). On the bottom: the jet p_T (on the left) and the $\sum p_T$ distribution of all objects (on the right). Cuts applied for all histograms are jet $p_T > 20$ GeV and jet $|\eta| < 2.8$ (blue) or $|\eta| < 5.0$ (red).

Fig. F.4 (in Appendix F).

As one can see in Fig. 5.15 and Fig. 5.16, the shape of the distributions of events with pile-up does not change significantly while changing the jet η cut, nor does it change in the case without pile-up. Therefore, jet η cut with $|\eta| < 2.8$ is taken to be optimal and sufficient for further studies.

The next step is to find optimal jet p_T cut. Fig. 5.17 shows the number of jets distribution with jet $|\eta| < 2.8$ and different jet p_T cuts, 20 GeV (black line), 40 GeV (red line), and 60 GeV (green line), respectively, for 7 TeV data samples (on the left) and 14 TeV ones (on the right). As one could observe, the tail of these distributions gets suppressed with jet p_T cut increasing, which is more apparent for the case of 14 TeV data samples. The important conclusion from these plots is that a 20 GeV cut is too low and allows many additional jets from pile-up interactions into the selection. One can see that because the number of jets distributions in the case of $p_T > 40$ GeV and $p_T > 60$ GeV are more similar to each other than compared with $p_T > 20$ GeV distribution.
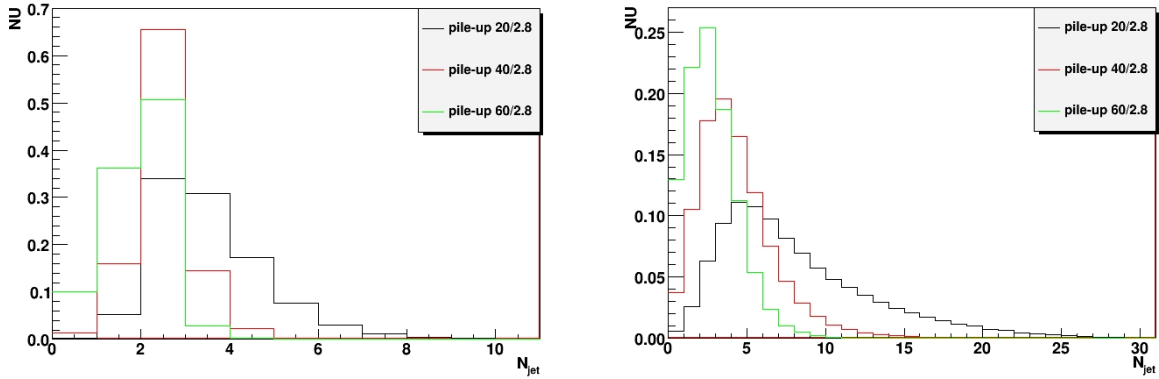
Figure 5.17: The number of jets distributions for different jet p_T cuts with jet $|\eta| < 2.8$ for 7 TeV (on the left) and 14 TeV data samples (on the right) with pile-up.
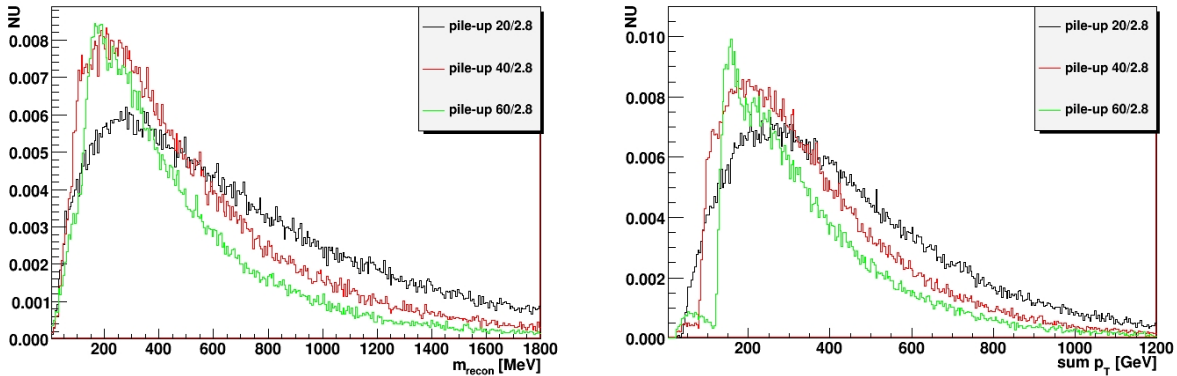

Figure 5.18: The invariant mass (on the left) and the $\sum p_T$ distribution (on the right) of all objects for 14 TeV data samples with pile-up.

Similarly, especially for the 14 TeV data samples in Fig. 5.18, one can note that the $\sum p_T$ and invariant mass distributions of all objects are much more similar for the higher-p_T cuts. Therefore, jet p_T cut with $p_T > 60$ GeV seems to be the most suitable.

Having established the jet η and p_T cuts, one can finally compare data samples with pile-up and without it including these jets cuts. As could be seen in Fig. 5.19 for the 7 TeV data samples and in Fig. 5.20 for the 14 TeV ones, since the distribution shapes look almost the same one can use these jet η and p_T cuts to reduce the influence of pile-up.

Tab. 5.2 shows the emission probabilities with the different cuts on jet p_T. By requiring only $p_T > 50$ GeV (instead of 60 GeV), the probability of observing a jet in minimum bias collisions is already low as 0.0367%. Even if there are more than five pile-up collisions, the probability of observing pile-up jets is estimated to be less than 0.2%. Consequently, the pile-up effect could be negligible by requiring a threshold of $p_T > 50$ GeV on jets. In the analysis hereafter, jets which have $p_T > 50$ GeV and $|\eta| < 2.8$ are used.

Figure 5.19: Final comparison of 7 TeV data samples with and without pile-up for jets with $p_T > 60$ GeV and $|\eta| < 2.8$. Top: the invariant mass of all objects (on the left) and the number of jets distribution (on the right); bottom: the jet p_T (on the left) and the $\sum p_T$ of all objects (on the right) distributions.

5.5 Search for Microscopic Black Holes in Multi-jet Final State in pp Collisions at $\sqrt{s} = 7$ TeV

After the simulation, a microscopic black holes events are searched for in the multi-jet final state in pp collisions at centre-of-mass energy of 7 TeV. In the following, the collision data collected by the ATLAS detector in 2010, corresponding to the integrated luminosity of ~ 35 pb^{-1} are used.

jet p_T cut	20 GeV	30 GeV	40 GeV	50 GeV
Probability [%]	1.41	0.284	0.0902	0.0357

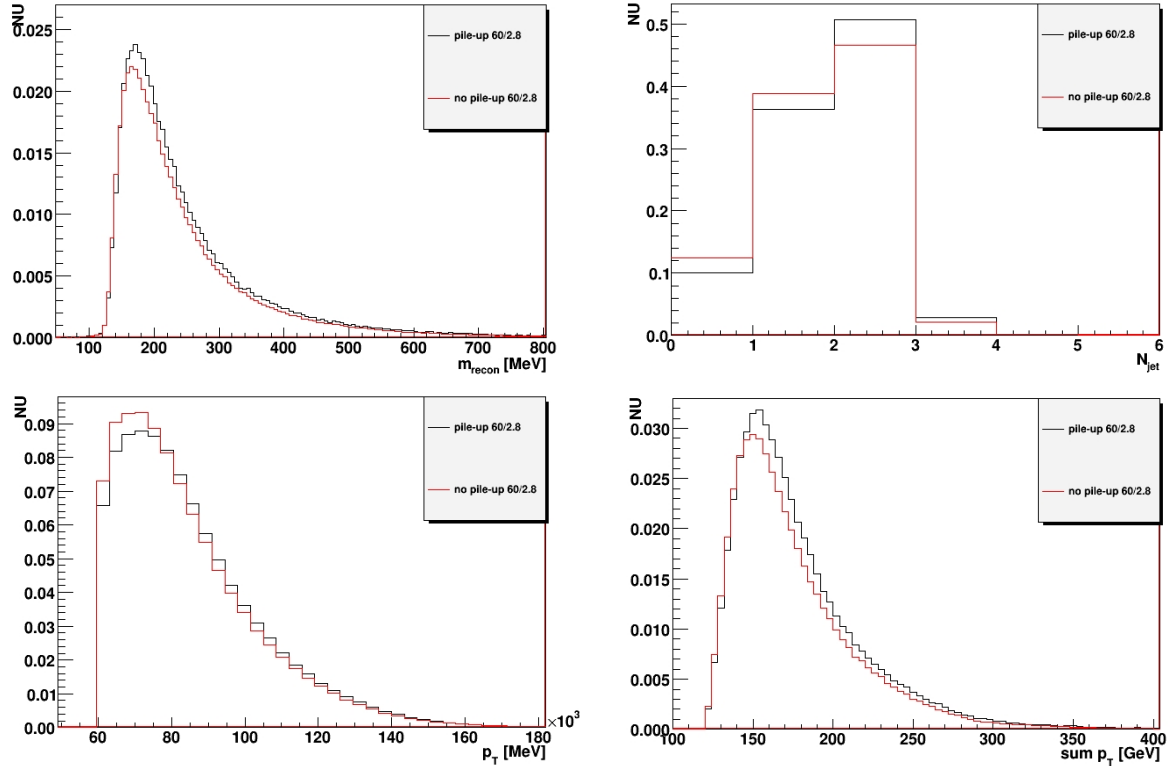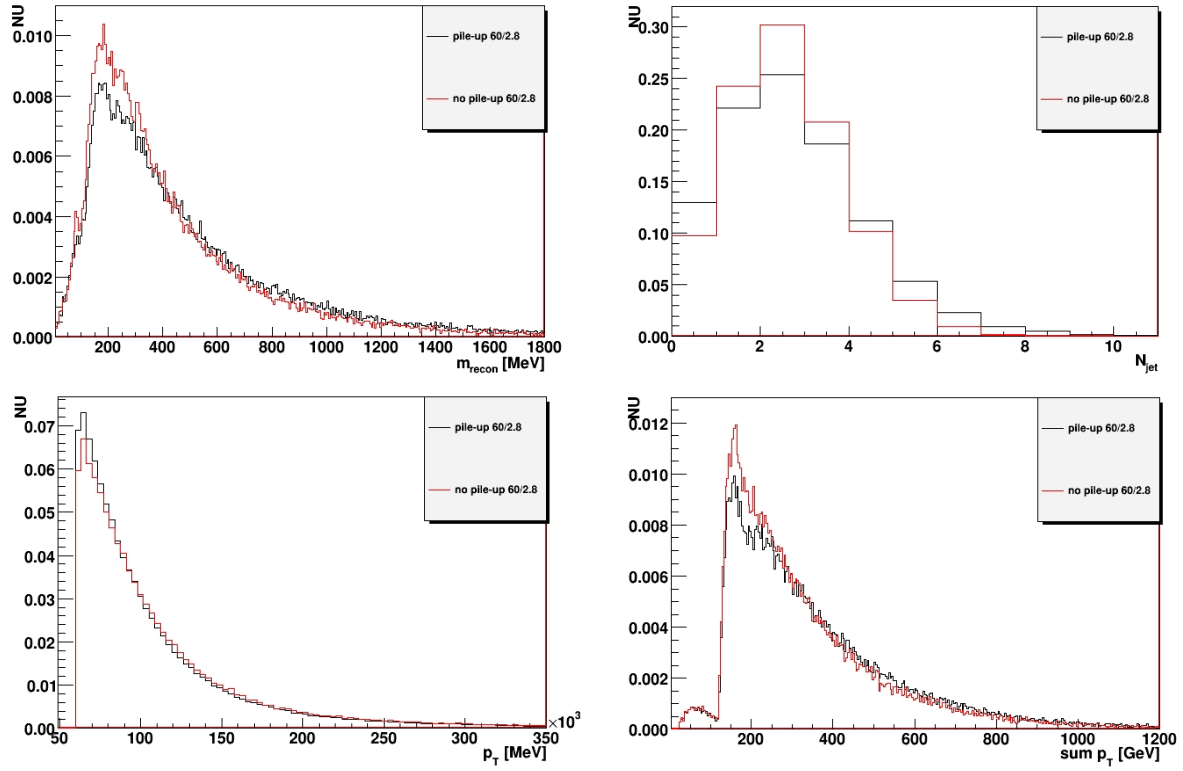Table 5.2: Emission probability of jets in pile-up events.

Figure 5.20: Final comparison of 14 TeV data samples with and without pile-up for jets with $p_T > 60$ GeV and $|\eta| < 2.8$. Top: the invariant mass of all objects (on the left) and the number of jets distribution (on the right); bottom: the jet p_T (on the left) and the $\sum p_T$ of all objects (on the right) distributions.

5.5.1 Working Model and Data Samples

As mentioned in the previous Chapter, a black hole is produced when an impact parameter, b of two colliding particles is smaller than the horizon radius, r_h, of the $n + 4$ spacetime:

$$b < 2r_h(n, M_{BH}, J), \tag{5.2}$$

where M_{BH} and J are the mass and the angular momentum of the black hole, respectively. The Schwarzschild radius, r_s, which is the horizon radius for a non-rotating black hole, is related to r_h as

$$r_h = \frac{r_s}{\left[1 + \left(\frac{(n+2)J}{2r_h M_{BH}}\right)^2\right]^{\frac{1}{n-1}}}. \tag{5.3}$$

The black hole is produced with the continuous mass distribution above a threshold, M_{BHth}. This threshold is one of the parameters of the black hole events and for the

simulated black holes in the following, assumptions listed below are used to determine M_{BHth}:

- The black hole is formed when the Compton wave length of the M_{BH}, λ, becomes smaller than the Schwarzschild radius with the centre-of-mass collision energy $E = M_{BH}$:

$$\lambda = \frac{2\pi}{E} = \frac{2\pi}{M_{BH}} < r_s. \tag{5.4}$$

- Another assumption based on r_h at $b = b_{max}$ instead of r_s is considered:

$$\lambda < r_h = \frac{b_{max}}{2}, \tag{5.5}$$

where b_{max} is given as:

$$b_{max} = 2 \frac{r_s}{\left[1 + \left(\frac{n+2}{2}\right)^2\right]^{\frac{2}{n+1}}}. \tag{5.6}$$

From the above conditions, M_{BHth} can be obtained as a function of the number of extra dimensions n and the fundamental Planck scale M_D. Fig. H.1 (top left) shows the first assumption and the second one is plotted on the top right (in Appendix H). On the assumption of (5.5), the higher number of extra dimensions shows the lower threshold. Fig. H.1 (bottom left) shows M_{BHth} calculated with (5.5) for each n, M_D. Corresponding cross-sections are shown in Fig. H.1 (bottom right) (in Appendix H).

The black hole Monte Carlo (MC) events are generated with BlackMax 2.01 [126]. The shower evolution and hadronization are simulated with Pythia 6.421 [133]. The main parameter settings of the model used are follows:

- The definition of Planck Scale follows the PDG definition [2].

- No form factor in the cross-section is used.

- CTEQ6.6 [134] parton distribution functions (PDF) are used.

- The QCD scale for the PDF is the mass of the black hole.

- Both baryon number and lepton number are conserved.

- Initial-state graviton radiation and graviton emission during the decay are not included.

- The burst model [126] is used when the black hole mass falls below the Planck scale.

- The number of extra dimension is varied from 2 to 7.

- The Planck scale is set as $M_D = 1.0. - 3.0$ TeV.

The main QCD MC sample is produced with Pythia. All background MC samples are listed in Tab. G.1 - G.5 (in Appendix G). The total amount of data used is ~ 35 pb^{-1} and 3610692 events.

5.5.2   Data Preselection and Jet Reconstruction

The events triggered by the single jet trigger are required to have at least one primary vertex which satisfies the following:

$$N_{\text{tracks}} \geq 5, \qquad |z_{\text{vertex}} - z_{\text{beamspot}}| < 15 \text{ cm}, \qquad (5.7)$$

where N_{tracks} is the number of tracks with $p_T > 150$ MeV associated to the primary vertex and z_{vertex} and z_{beamspot} are the positions of the vertex and the beam collision spot along the z-axis, respectively. This primary vertex requirement is applied to remove non-collision background events.

Additionally, quality criteria for jet are applied to remove fake jets such as spiky noise in the calorimeter and bremsstrahlung of muons in cosmic-rays. To ensure the full efficiency of the jet trigger, the leading jet is required to have p_T larger than 250 GeV. After all preselection cuts, 171902 events remain.

For jet reconstruction anti-k_T cluster algorithm with jet size parameter $R = 0.4$ is used. Finally, the results from the previous Section are adopted and, therefore, only jets with $p_T > 50$ GeV and $|\eta| < 2.8$ are used in the analysis, because the pile-up effects could be then negligible.

Fig. 5.21 shows the $\sum p_T$ distributions for signal and background. They are divided into two regions of $1 < N_J < 5$ and $N_J \geq 5$. Two things should be noted. First, the simulated QCD background falls steeply with increasing $\sum p_T$ whereas the signal distributions peak at large $\sum p_T$. Second, the ratio of signal to QCD is larger, at a fixed value of $\sum p_T$, for $N_J > 5$.
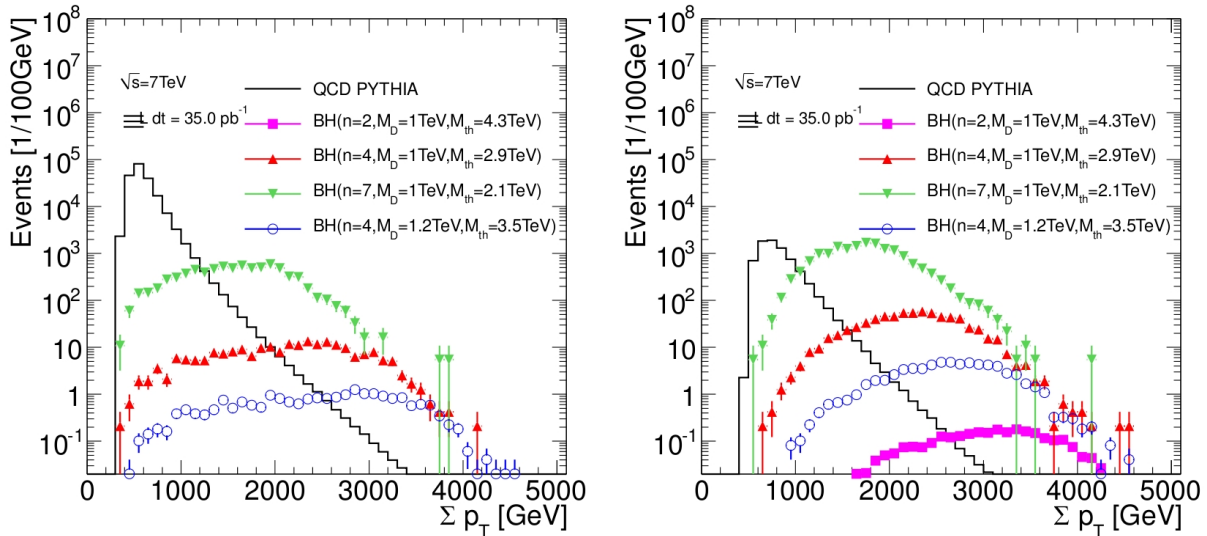

Figure 5.21: Scalar sum of jet transverse momenta ($\sum p_T$) distributions of simulated black hole signal and Pythia QCD background events with number of jets less than five (on the left) and greater than or equal to five (on the right) [135].

Tab. 5.3 summarizes the expected numbers of events in the region of $N_J \geq 5$ and $\sum p_T > 1500$ (2000) GeV for background and signal events. Signal events show high efficiencies even in the range of $\sum p_T > 2000$ GeV, while only a few events of QCD background events remain. Therefore, the signal region is set as follows:

$$N_J \geq 5, \qquad \sum p_T > 2000 \text{ GeV}. \tag{5.8}$$

Process	$\sum p_T > 1500$ GeV (acc [%])	$\sum p_T > 2000$ GeV (acc [%])
	Black Holes	
$n = 2$, $M_D = 1$ TeV, $M_{BHth} = 4.3$ TeV	2.72 (75.9)	2.58 (71.9)
$n = 4$, $M_D = 1$ TeV, $M_{BHth} = 2.9$ TeV	6.65×10^2 (63.4)	4.95×10^2 (42.9)
	Background	
QCD ($p_T > 8$ GeV)	57.9 ($\sim 10^{-8}$)	5.03 ($\sim 10^{-9}$)
$t\bar{t}$	0.626 (0.011)	0.095 (0.002)
Z + jets ($p_T > 250$ GeV)	0.082 (0.06)	0.014 (0.01)
W + jets ($p_T > 250$ GeV)	0.162 (0.05)	< 0.001 (-)
γ + jets ($p_T > 240$ GeV)	0.019 ($\sim 10^{-3}$)	0.002 ($\sim 10^{-4}$)

Table 5.3: Expected number of events and the acceptance (acc) for signal and background events with $N_J \geq 5$ and $p_T > 1500$ (2000) GeV. The p_T cuts for background MC events represent the cuts on the leading parton p_T. The numbers are normalized to 35 pb^{-1} [135].

Jets in Observed Events

The QCD multi-jet production constitutes the main Standard Model background for this search. The shapes of jet distributions in the observed events are compared to QCD MC events. All the histograms of QCD MC events are normalized to the numbers of observed events. Fig. H.2, Fig. H.3 and Fig. H.4 (in Appendix H) show the p_T distributions of the leading ten jets. Fig. H.5 (also in Appendix H) shows the N_J distributions (on the left) and the p_T distribution of data and QCD MC events in the region of $N_J < 5$ in which QCD background events are expected to dominate (on the right). All the shapes of the jet and p_T distributions in the observed events are consistent with the QCD background expectations within the statistical uncertainties and no significant excess of signal is found.

5.5.3 Systematic Uncertainties

The systematic uncertainties of background shape and signal normalization are evaluated as well. Tab. 5.4 shows the summary of the background shape uncertainties. In total, an uncertainty of 30.0% is quoted. For a typical signal case ($n = 4$, $M_D = 1$ TeV, and $M_{th} = 3$ TeV), the total uncertainty is 13.2%. The detailed discussion on all systematic uncertainties is given in [135].

Source of Systematic Uncertainty	Uncertainty [%]
$\sum p_T$-dependence of the ratio	11.3
Jet energy scale	2.0
Jet energy resolution	1.7
QCD physics model description	23.5
Parton density functions	14.6
Other background contribution	0.2

Table 5.4: Systematic uncertainties of the background shape [135].

5.5.4   Final Results

Fig. 5.22 shows the $\sum p_T$ distributions of data for $N_J \geq 5$ and $N_J < 5$. The distributions are normalized to the number of events in the range $1100 < \sum p_T < 1200$ GeV. The yellow error band includes the total uncertainty including statistical and systematic uncertainties.

The 95% confidence level (CL) upper limits on cross-section are calculated for each signal parameter point. These upper limits give the contour plot for the excluded region in $M_D - M_{th}$ space by comparison with the theoretical cross-sections. Fig. 5.23 (left) shows the 95% CL upper limits as a function of the fundamental scale M_D and of the mass threshold M_{th} for every number of extra dimensions n. The region below and to the left of the lines is excluded. The expected limits for the data set of the same size as the actual one are shown in Fig. 5.23 (right). Since the number of events observed from the data is greater than the background expectation, the observed limits are less stringent than the expected ones.

Fig. H.7 (Fig. H.8) (in Appendix H) shows the 95% CL upper limits on the signal cross-sections as a function of M_D for each signal point and n on the assumption of $\lambda < r_s$ (r_h). The observed limits, the theoretical cross-sections and the expected limits for no signal are shown by rectangles, solid lines and dashed lines, respectively. The uncertainties on the theoretical cross-sections and 1σ (2σ) counters of the expected limits are shown by green (yellow) error bands.

The lower limits on the Planck scale were obtained form these cross-section upper limits. On the assumption of $\lambda < r_s$ (r_h), a lower limit on the Planck scale at 95% CL was set as

$$M_D > 1.27 \ (1.06) \text{ TeV} \qquad \text{for} \qquad n = 4 \ (5), \qquad (5.9)$$

and more strict limits for larger n were obtained. The above analysis used the data collected in year 2010 with integrated luminosity of ~ 35 pb^{-1} and currently no evidence of the black holes signal is observed.
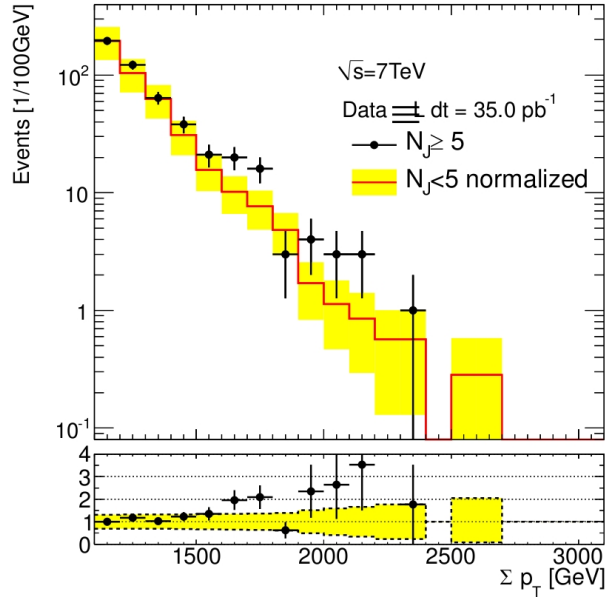
Figure 5.22: $\sum p_T$ distributions of observed events for $N_J \geq 5$ (filled circles) and $N_J < 5$ (histogram). The histogram is normalized to the number of events in the range $1100 < \sum p_T < 1200$ GeV. The yellow error band represents the total uncertainty including the statistical and the systematic uncertainties [135].
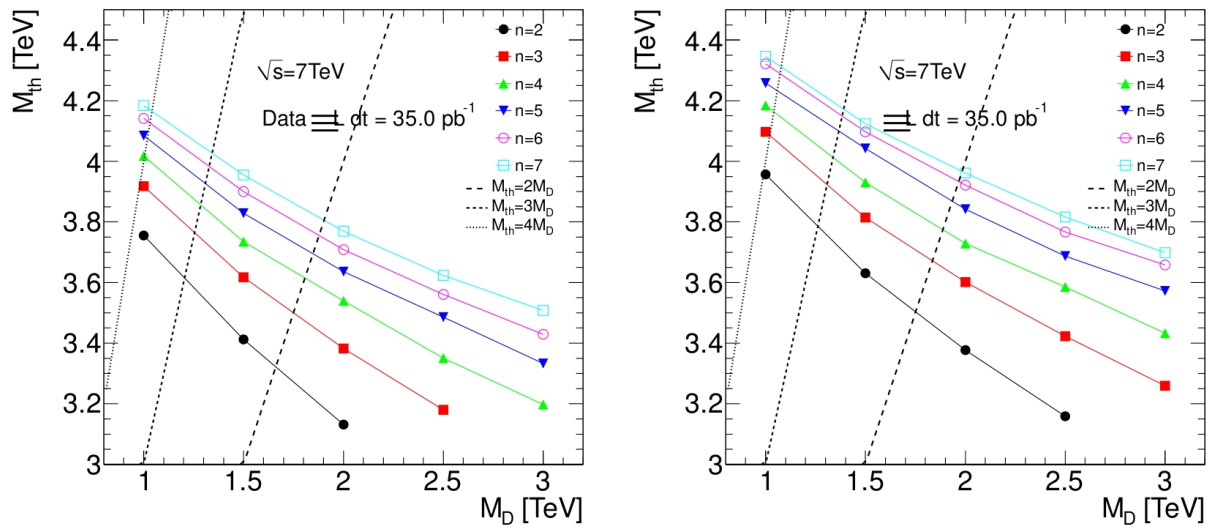

Figure 5.23: Contour plots of limits on the fundamental scale M_D versus the threshold mass M_{th}. Observed limits on the left and expected limits on the right plot. The curves are labelled by the number of extra dimensions n. CTEQ6.6 PDF is used for the signal contribution. Also shown are lines of fixed ratio M_{th}/M_D [135].

Conclusion

In this thesis the production of microscopic black holes at particle colliders within the extra-dimensional Universe was studied. The Large Hadron Collider is able to produce these microscopic black holes and the ATLAS detector has a great opportunity to observe them and study their decay products in detail.

At the Large Hadron Collider the additional soft collisions producing low-p_T jets should not be ignored. The influence of this pile-up events on jet production within microscopic black hole searches was analysed in this thesis. This study was done as one of the first parts of the multi-jet final state analysis. The simulated data samples with di-jet and $t\bar{t}$ events with centre-of-mass energy of $\sqrt{s} = 7$ TeV and 14 TeV where studied. Optimal criteria on produced jet events were found to be $p_T > 50$ GeV and $|\eta| < 2.8$ for both cases of centre-of-mass energy. Additionally, the pile-up influence were found not to have such significant effect in the case of 7 TeV as in the 14 TeV one, as had been expected.

Moreover, in this study the other objects such as electrons, muons and photons seem not to be really significantly affected by pile-up events and, therefore, the pile-up effects could be negligible in their case. These additional criteria to jet selection give an advantage to suppress the above mentioned pile-up events and, thus, make the signal clearer for further multi-jet analysis.

With all simulations of the discovery reach of microscopic black hole events within ATLAS detector done before and taking the above results of suppressing pile-up effects on jet production into account, the microscopic black holes were searched for in the multi-jet final state with the real data collected in 2010 with centre-of-mass energy of $\sqrt{s} = 7$ TeV and integrated luminosity of ~ 35 pb^{-1}. Nevertheless, till now no evidence of microscopic black holes signal has been observed. However, even though these microscopic black holes have not yet been discovered, the lower limits on the Planck scale were obtained to be $M_D > 1.27$ (1.06) TeV for the number of extra dimension $n = 4$ (5), respectively.

The multi-jet analysis is going to continue with the new data collected during the year 2011. Moreover, looking for microscopic black holes events within lepton plus jets final state analysis is now preparing. Till now, several simulations have been already done and in the following days this analysis tool will be prepared to look for microscopic black holes events in real data collected in 2010 and also in 2011.

Appendix A

Main Parameters of ATLAS Detector

Item		Radial extension [mm]	Length [mm]
Overall inner detector envelope		$0 < R < 1150$	$0 < |z| < 3512$
Beam-pipe		$29 < R < 36$	
Pixel	Overall envelope	$45.5 < R < 242$	$0 < |z| < 3092$
3 cylindrical layers	Sensitive barrel	$50.4 < R < 122.5$	$0 < |z| < 400.5$
2×3 discs	Sensitive end-cap	$88.8 < R < 149.6$	$495 < |z| < 650$
SCT	Overall envelope	$255 < R < 549$ (barrel)	$0 < |z| < 805$
		$251 < R < 610$ (end-cap)	$810 < |z| < 2797$
4 cylindrical layers	Sensitive barrel	$299 < R < 514$	$0 < |z| < 749$
2×9 discs	Sensitive end-cap	$275 < R < 560$	$839 < |z| < 2735$
TRT	Overall envelope	$554 < R < 1082$ (barrel)	$0 < |z| < 780$
		$617 < R < 1106$ (end-cap)	$827 < |z| < 2744$
73 straw planes	Sensitive barrel	$563 < R < 1066$	$0 < |z| < 712$
160 straw planes	Sensitive end-cap	$644 < R < 1004$	$848 < |z| < 2710$

Table A.1: Main parameters of the inner detector [17].

	Barrel		**End-cap**	
EM calorimeter				
Number of layers and $|\eta|$ coverage				
Presampler	1	$|\eta| < 1.52$	1	$1.5 < |\eta| < 1.8$
Calorimeter	3	$|\eta| < 1.35$	2	$1.375 < |\eta| < 1.5$
	2	$1.35 < |\eta| < 1.475$	3	$1.5 < |\eta| < 2.5$
			2	$2.5 < |\eta| < 3.2$
Number of readout channels				
Presampler	7808		1536 (both sides)	
Calorimeter	101760		62208 (both sides)	
LAr hadronic end-cap				
$|\eta|$ coverage			$1.5 < |\eta| < 3.2$	
Number of layers			4	
Readout channels			5632 (both sides)	
LAr forward calorimeter				
$|\eta|$ coverage			$3.1 < |\eta| < 4.9$	
Number of layers			3	
Readout channels			3524 (both sides)	
Scintillator tile calorimeter				
	Barrel		Extended barrel	
$|\eta|$ coverage	$|\eta| < 1.0$		$0.8 < |\eta| < 1.7$	
Number of layers	3		3	
Readout channels	5760		4092 (both sides)	

Table A.2: Main parameters of the calorimeter system [17].

Monitored drift tubes	MDT
- Coverage	$\|\eta\| < 2.7$ (innermost layer: $\|\eta\| < 2.0$)
- Number of chambers	1088 (1150)
- Number of channels	399 000 (354 000)
- Function	Precision tracking
Cathode strip chambers	**CSC**
- Coverage	$2.0 < \|\eta\| < 2.7$
- Number of chambers	32
- Number of channels	31 000
- Function	Precision tracking
Resistive plate chambers	**RPC**
- Coverage	$\|\eta\| < 1.05$
- Number of chambers	544 (606)
- Number of channels	359 000 (373 000)
- Function	Triggering, second coordinate
Thin gap chambers	**TGC**
- Coverage	$1.05 < \|\eta\| < 2.7$ (2.4 for triggering)
- Number of chambers	3588
- Number of channels	318 000
- Function	Triggering, second coordinate

Table A.3: Main parameters of the muon spectrometer [17].
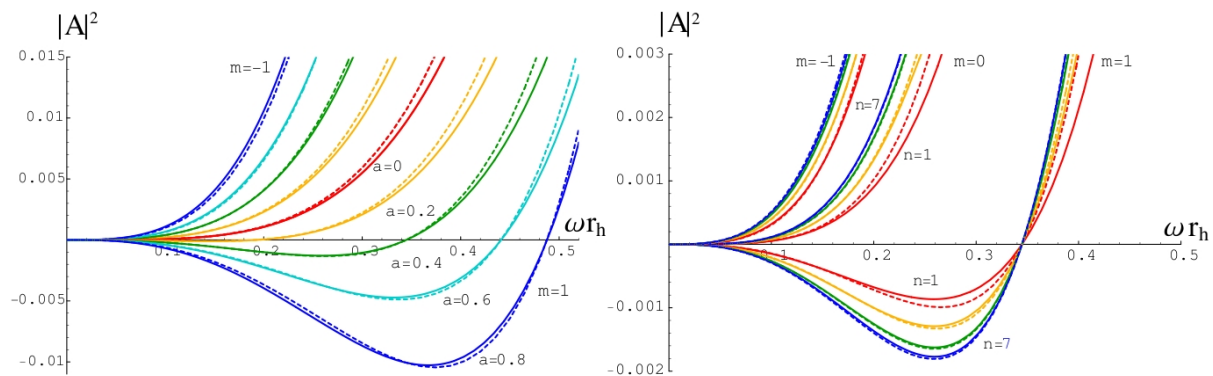
Appendix B

Additional Plots to Hawking Radiation

Figure B.1: Absorption probabilities for brane-localised scalar fields as a function of the angular-momentum parameter a (left plot) and number of extra dimensions n (right plot). The solid lines correspond to analytic results, and the dashed lines to the exact numerical ones [111].
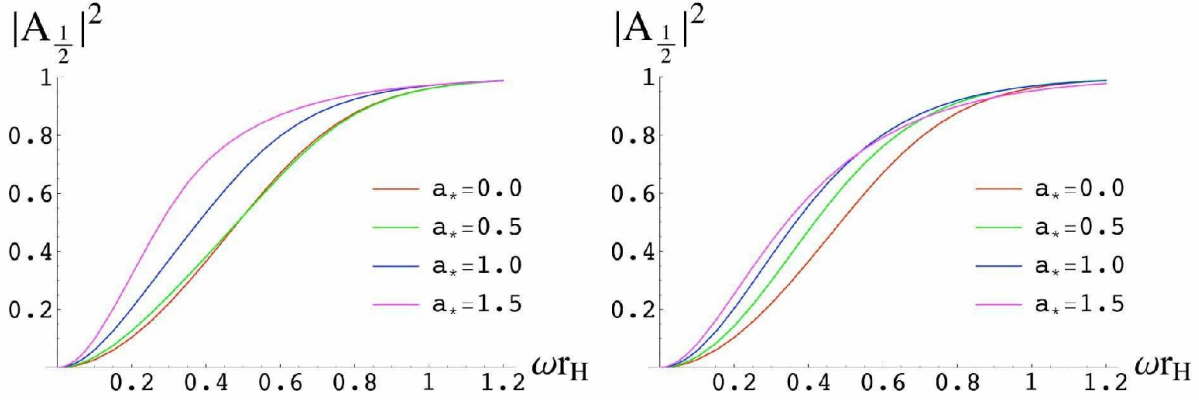
Figure B.2: Absorption probability $|\mathcal{A}_{1/2}|^2$ for brane spinor particles, for the modes $j = 1/2$ and $m = 1/2, -1/2$, from left to right, for $n = 6$ and $a_* = 0.0, 0.5, 1.0, 1.5$ [111].
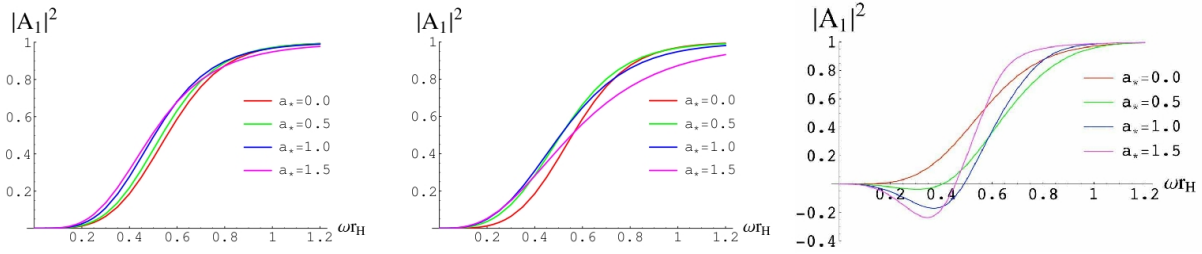

Figure B.3: Absorption probability $|\mathcal{A}_1|^2$ for brane boson particles, for the modes $j = 1$ and $m = 0, -1, 1$, from left to right, for $n = 6$ and $a_* = 0.0, 0.5, 1.0, 1.5$ [111].
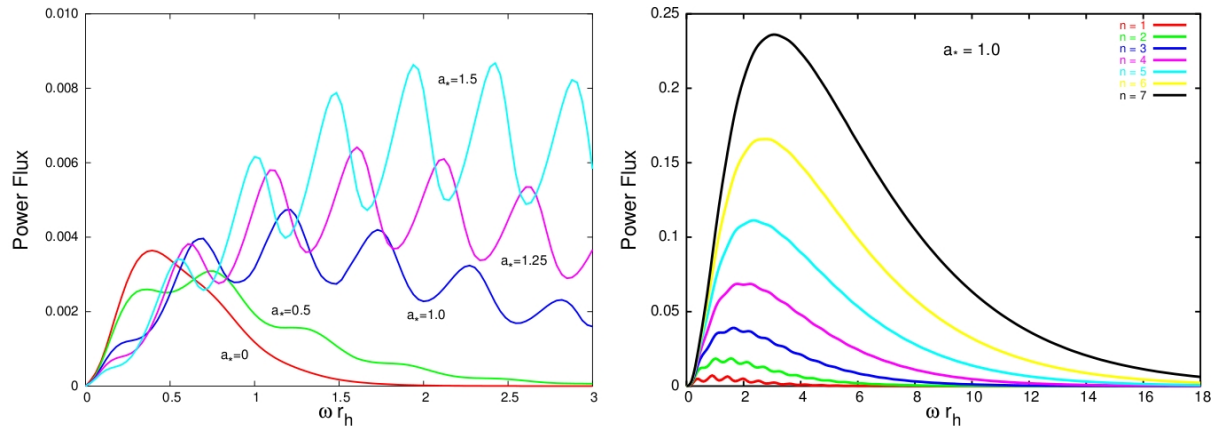

Figure B.4: Energy emission rates for brane-localised scalar fields in terms of the angular parameter (left plot) and gauge bosons in terms of the number of extra dimensions (right plot) [111].
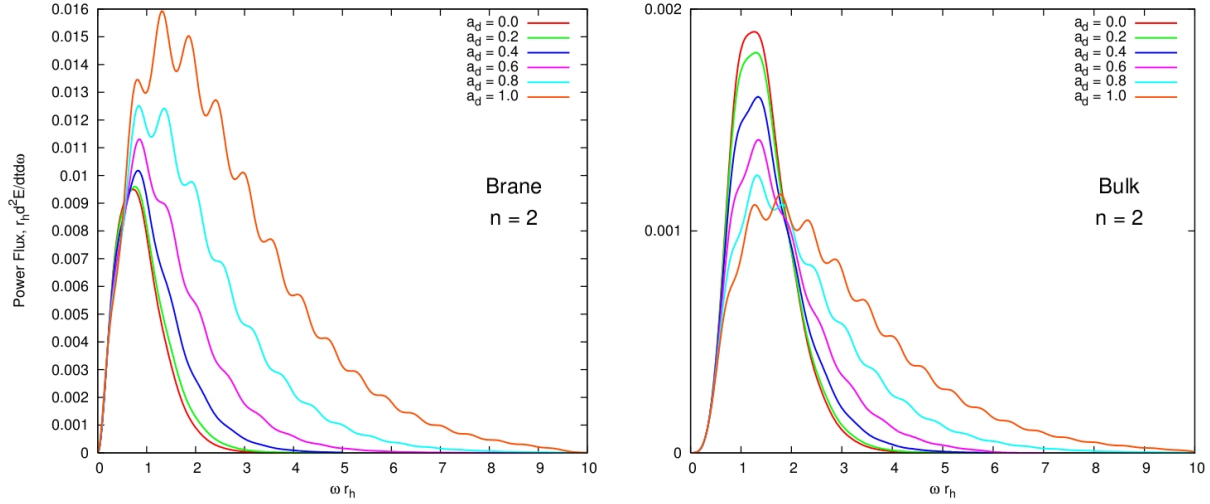
Figure B.5: Brane and bulk emission from a 6-dimensional rotating black hole. The left and right plots show the power emitted on the brane and in the bulk, respectively. Black hole rotation increases the proportion of the total flux that is emitted on the brane. Note the order-of-magnitude difference in the scales on the y-axis [115].
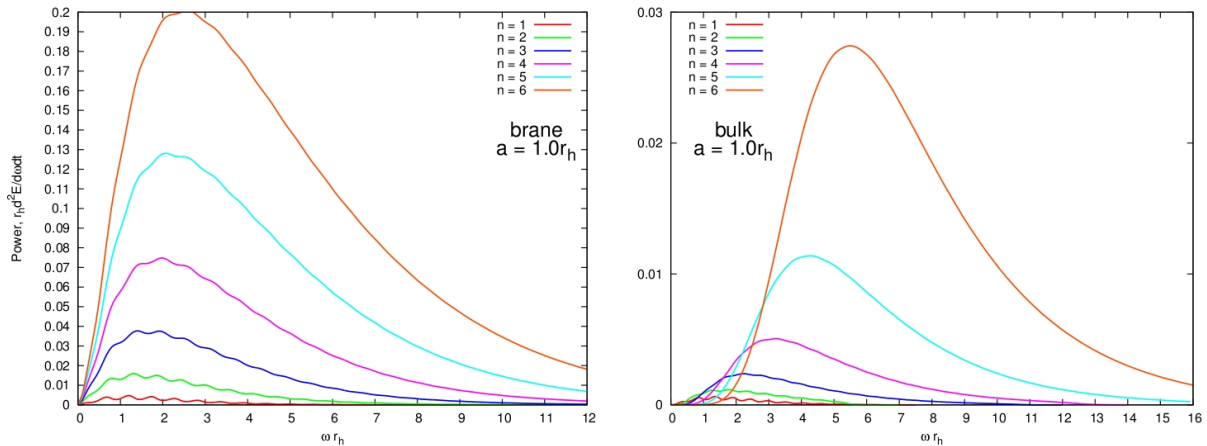

Figure B.6: Emission by a rotating black hole. These plots compare the power emitted on the brane (left) and in the bulk (right) at $a_d = 1.0$. Note the difference in the scales on the y-axis. [115].

Appendix C

CHARYBDIS Default Parameters

Name	Description	Value
MINMSS	Minimum mass of black holes	5 TeV
MAXMSS	Maximum mass of black holes	14 TeV
MPLNCK	Planck scale	1 TeV
MSSDEF	Convention for Planck scale	2
TOTDIM	Total number of dimensions	6
NBODY	Number of particles in remnant decay	2
GTSCA	Black hole mass used as PDF momentum scale	True
TIMVAR	Allow T_H to change with time	True
MSSDEC	Use all Standard Model particles as decay products	True
GRYBDY	Include greybody effects	True
KINCUT	Use a kinematic cut-off on the decay	True

Table C.1: Default parameters used in the CHARYBDIS generator.

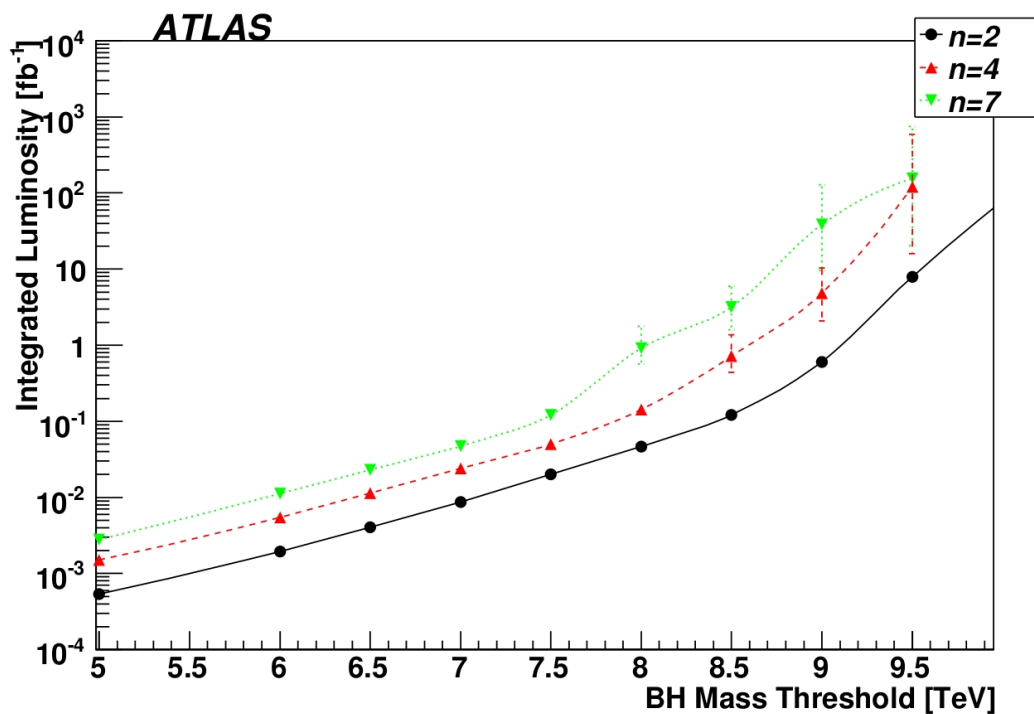# Appendix D

Additional Plots to Black Hole Simulation

Figure D.1: Discovery potential using $\sum p_T$ and lepton selections: required luminosity as a function of black hole mass threshold. Error bars reflect statistical uncertainties only [131].
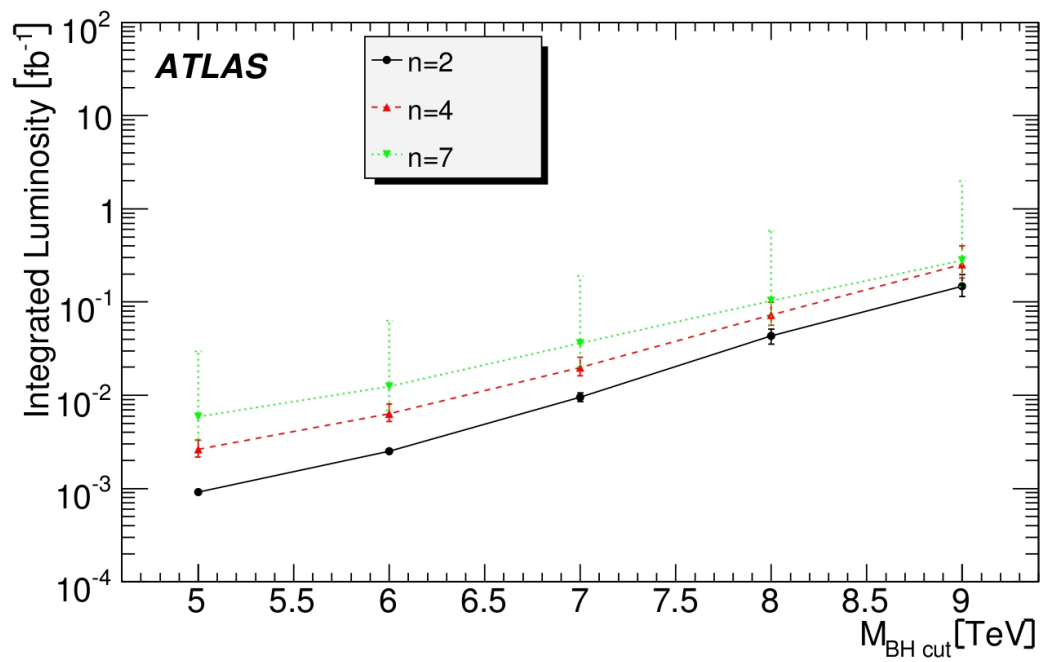
Figure D.2: Discovery potential for black holes using the four-objects and the lepton requirements. The required luminosity is shown as a function of the requirement on the reconstructed black hole mass. The error bars correspond to experimental systematic uncertainties [131].

Appendix E

Datasets for Pile-up Studies

7 TeV Samples			
mc09_7TeV.105012.J3_pythia_jetjet.merge.AOD.e468_s766_s767_r1425_r1429/			
mc09_7TeV.105012.J3_pythia_jetjet.merge.AOD.e468_s766_s767_r1303_r1306/			
Config Tag	Athena Release	ATLAS Geometry	Events
e468_s766_s767_r1425_r1429	15.6.12	ATLAS-GEO-10-00-00	399891
e468_s766_s767_r1303_r1306	15.6.12	ATLAS-GEO-10-00-00	1397430

14 TeV Samples			
mc09_14TeV.105568.ttbar_Pythia.recon.AOD.e478_s616_d280_r898/			
mc09_14TeV.105568.ttbar_Pythia.recon.AOD.e478_s616_d275_r1049/			
Config Tag	Athena Release	ATLAS Geometry	Events
e478_s616_d280_r898	15.3.1	ATLAS-GEO-08-00-01	99922
e478_s616_d275_r1049	15.3.1	ATLAS-GEO-08-00-01	99922

Table E.1: 7 TeV and 14 TeV data samples.

Appendix F

Additional Plots to Pile-up Studies

Figure F.1: Histograms of 7 TeV data samples to find optimal jet η cut. The top row: the invariant mass distribution of all objects for jets with $p_T > 40$ GeV (on the left) and $p_T > 60$ GeV (on the right). On the bottom: the number of jets distribution with $p_T > 40$ GeV (on the left) and $p_T > 60$ GeV (on the right).

Figure F.2: Histograms of 7 TeV data samples to find optimal jet η cut. The top row: the jet p_T distribution for jets with $p_T > 40$ GeV (on the left) and $p_T > 60$ GeV (on the right). On the bottom: the $\sum p_T$ distribution of all objects with $p_T > 40$ GeV (on the left) and $p_T > 60$ GeV (on the right).
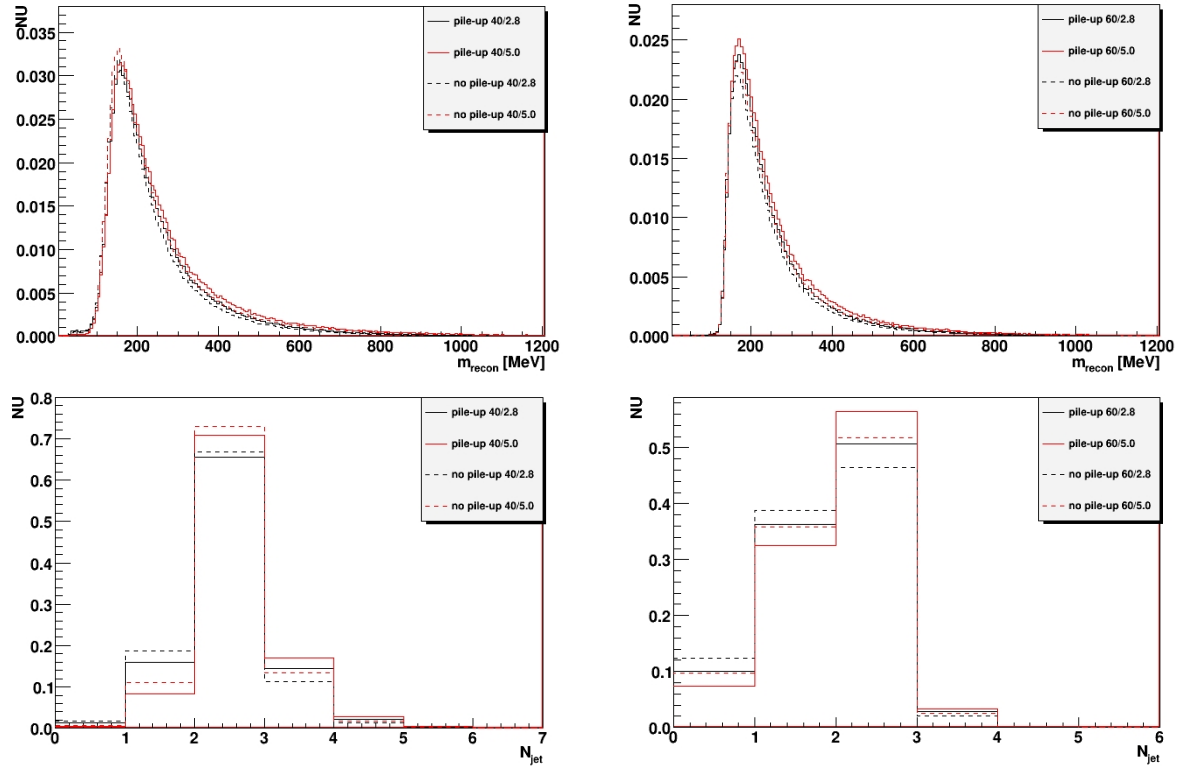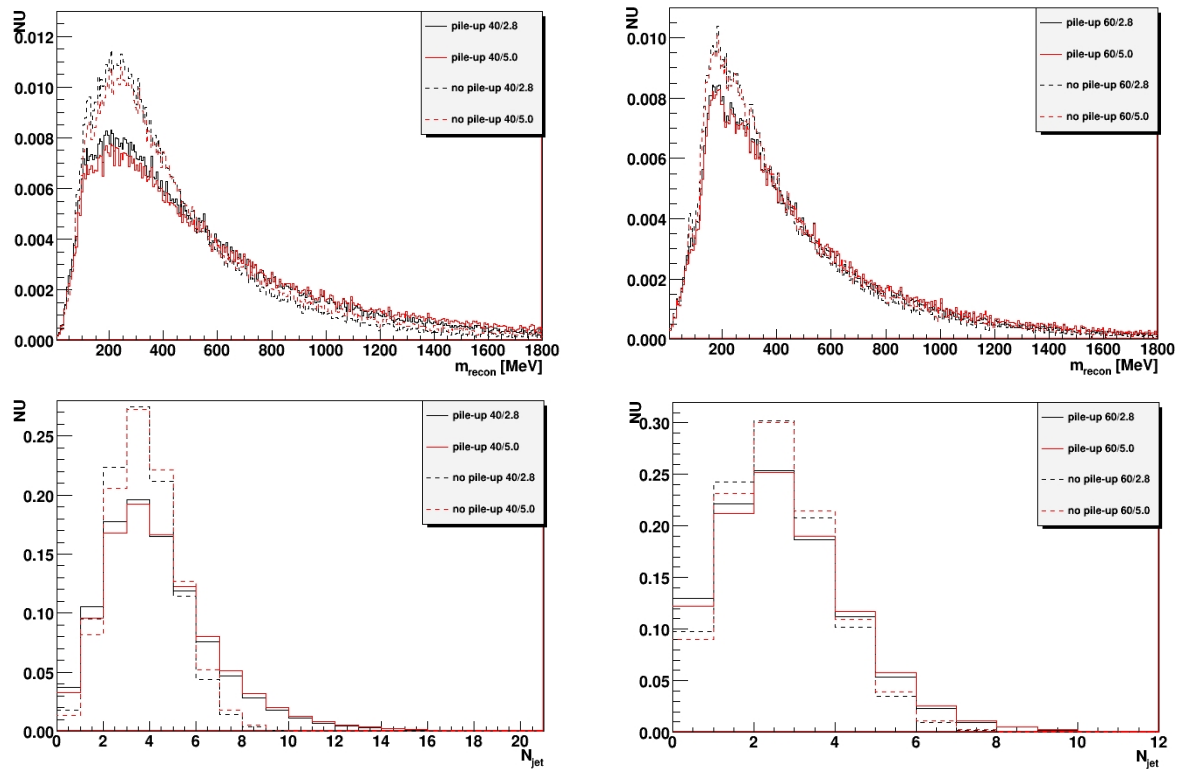
Figure F.3: Histograms of 14 TeV data samples to find optimal jet η cut. The top row: the invariant mass distribution of all objects for jets with $p_T > 40$ GeV (on the left) and $p_T > 60$ GeV (on the right). On the bottom: the number of jets distribution with $p_T > 40$ GeV (on the left) and $p_T > 60$ GeV (on the right).
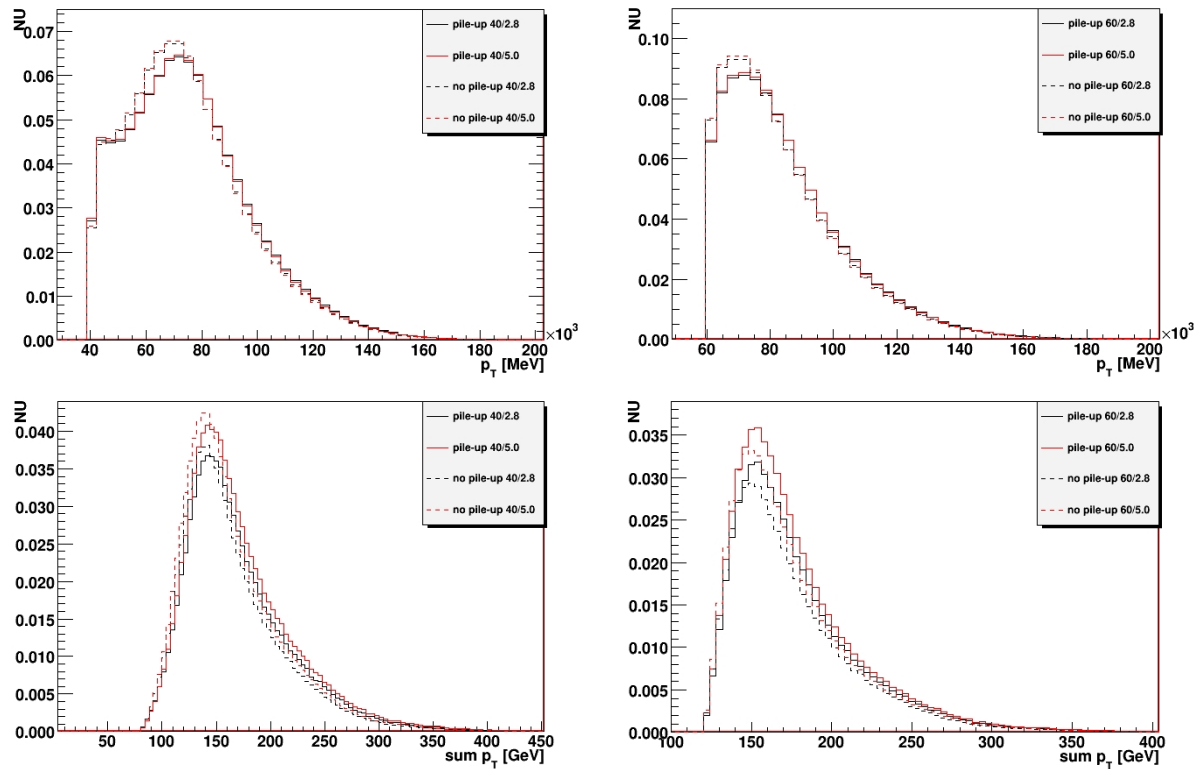
Figure F.4: Histograms of 14 TeV data samples to find optimal jet η cut. The top row: the jet p_T distribution for jets with $p_T > 40$ GeV (on the left) and $p_T > 60$ GeV (on the right). On the bottom: the $\sum p_T$ distribution of all objects with $p_T > 40$ GeV (on the left) and $p_T > 60$ GeV (on the right).
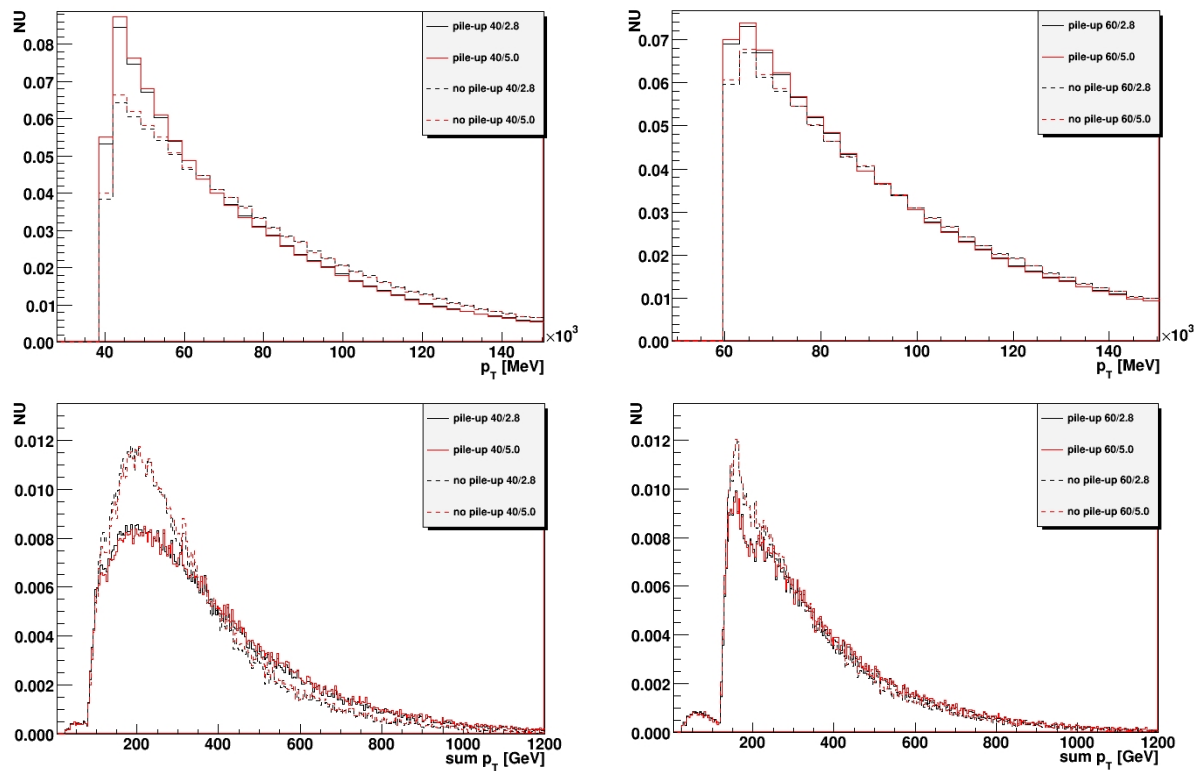
Appendix G

Standard Model MC Datasets

Dataset Name
mc09_7TeV.105009.J0_pythia_jetjet.merge.NTUP_JETMET.e468_s766_s767_r1303_p209
mc09_7TeV.105010.J1_pythia_jetjet.merge.NTUP_JETMET.e468_s766_s767_r1303_p209
mc09_7TeV.105011.J2_pythia_jetjet.merge.NTUP_JETMET.e468_s766_s767_r1303_p209
mc09_7TeV.105012.J3_pythia_jetjet.merge.NTUP_JETMET.e468_s766_s767_r1303_p209
mc09_7TeV.105013.J4_pythia_jetjet.merge.NTUP_JETMET.e468_s766_s767_r1303_p209
mc09_7TeV.105014.J5_pythia_jetjet.merge.NTUP_JETMET.e468_s766_s767_r1303_p209
mc09_7TeV.105015.J6_pythia_jetjet.merge.NTUP_JETMET.e468_s766_s767_r1303_p209
mc09_7TeV.105016.J7_pythia_jetjet.merge.NTUP_JETMET.e468_s766_s767_r1303_p209
mc09_7TeV.105017.J8_pythia_jetjet.merge.NTUP_JETMET.e468_s766_s767_r1336_p209

Table G.1: Pythia QCD MC samples.

Dataset Name
mc09_7TeV.113200.Jimmy_Zj_hadronic.merge.NTUP_JETMET.e552_s765_s767_r1302_r1306_p213
mc09_7TeV.113201.Jimmy_Wj_hadronic.merge.NTUP_JETMET.e552_s765_s767_r1302_r1306_p213

Table G.2: Z + jets and W + jets MC samples.

Dataset Name
mc09_7TeV.105200.T1 McAtNlo_Jimmy.merge.NTUP_JETMET.e510_s765_s767_r1302_r1306_p213
mc09_7TeV.105204.TTbar_FullHad_McAtNlo_Jimmy.merge.NTUP_JETMET.e540_s765_s767_r1302_r1306_p213

Table G.3: $t\bar{t}$ MC samples.

Dataset Name
mc09_7TeV.113129.AlpgenJimmyNjetsNp2_J1x.merge.NTUP_JETMET.e530_s765_s767_r1302_p209
mc09_7TeV.113130.AlpgenJimmyNjetsNp2_J2.merge.NTUP_JETMET.e530_s765_s767_r1302_p209
mc09_7TeV.113131.AlpgenJimmyNjetsNp2_J3.merge.NTUP_JETMET.e530_s765_s767_r1302_p209
mc09_7TeV.113132.AlpgenJimmyNjetsNp2_J4.merge.NTUP_JETMET.e530_s765_s767_r1302_p209
mc09_7TeV.113133.AlpgenJimmyNjetsNp2_J5.merge.NTUP_JETMET.e530_s765_s767_r1302_p209
mc09_7TeV.113134.AlpgenJimmyNjetsNp2_J6p.merge.NTUP_JETMET.e530_s765_s767_r1302_p209
mc09_7TeV.113135.AlpgenJimmyNjetsNp3_J1x.merge.NTUP_JETMET.e530_s765_s767_r1302_p209
mc09_7TeV.113136.AlpgenJimmyNjetsNp3_J2.merge.NTUP_JETMET.e530_s765_s767_r1302_p209
mc09_7TeV.113137.AlpgenJimmyNjetsNp3_J3.merge.NTUP_JETMET.e530_s765_s767_r1302_p209
mc09_7TeV.113138.AlpgenJimmyNjetsNp3_J4.merge.NTUP_JETMET.e530_s765_s767_r1302_p209
mc09_7TeV.113139.AlpgenJimmyNjetsNp3_J5.merge.NTUP_JETMET.e530_s765_s767_r1302_p209
mc09_7TeV.113140.AlpgenJimmyNjetsNp3_J6p.merge.NTUP_JETMET.e530_s765_s767_r1302_p209
mc09_7TeV.113141.AlpgenJimmyNjetsNp4_J1x.merge.NTUP_JETMET.e530_s765_s767_r1302_p209
mc09_7TeV.113142.AlpgenJimmyNjetsNp4_J2.merge.NTUP_JETMET.e530_s765_s767_r1302_p209
mc09_7TeV.113143.AlpgenJimmyNjetsNp4_J3.merge.NTUP_JETMET.e530_s765_s767_r1302_p209
mc09_7TeV.113144.AlpgenJimmyNjetsNp4_J4.merge.NTUP_JETMET.e530_s765_s767_r1302_p209
mc09_7TeV.113145.AlpgenJimmyNjetsNp4_J5.merge.NTUP_JETMET.e530_s765_s767_r1302_p209
mc09_7TeV.113146.AlpgenJimmyNjetsNp4_J6p.merge.NTUP_JETMET.e530_s765_s767_r1302_p209
mc09_7TeV.113147.AlpgenJimmyNjetsNp5_J1x.merge.NTUP_JETMET.e530_s765_s767_r1302_p209
mc09_7TeV.113148.AlpgenJimmyNjetsNp5_J2.merge.NTUP_JETMET.e530_s765_s767_r1302_p209
mc09_7TeV.113149.AlpgenJimmyNjetsNp5_J3.merge.NTUP_JETMET.e530_s765_s767_r1302_p209
mc09_7TeV.113150.AlpgenJimmyNjetsNp5_J4.merge.NTUP_JETMET.e530_s765_s767_r1302_p209
mc09_7TeV.113151.AlpgenJimmyNjetsNp5_J5.merge.NTUP_JETMET.e530_s765_s767_r1302_p209
mc09_7TeV.113152.AlpgenJimmyNjetsNp5_J6p.merge.NTUP_JETMET.e530_s765_s767_r1302_p209
mc09_7TeV.113153.AlpgenJimmyNjetsNp6_J1x.merge.NTUP_JETMET.e530_s765_s767_r1302_p209
mc09_7TeV.113154.AlpgenJimmyNjetsNp6_J2.merge.NTUP_JETMET.e530_s765_s767_r1302_p209
mc09_7TeV.113155.AlpgenJimmyNjetsNp6_J3.merge.NTUP_JETMET.e530_s765_s767_r1302_p209
mc09_7TeV.113156.AlpgenJimmyNjetsNp6_J4.merge.NTUP_JETMET.e530_s765_s767_r1302_p209
mc09_7TeV.113157.AlpgenJimmyNjetsNp6_J5.merge.NTUP_JETMET.e530_s765_s767_r1302_p209
mc09_7TeV.113158.AlpgenJimmyNjetsNp6_J6p.merge.NTUP_JETMET.e530_s765_s767_r1302_p209

Table G.4: Alpgen + Jimmy QCD MC samples.

Dataset Name
mc09_7TeV.108083.PythiaPhotonJet_Unbinned140.merge.NTUP_JETMET.e505_s765_s767_r1302_r1306_p213

Table G.5: γ + jets MC samples.

Appendix H

Additional Plots to Multi-jet Final State Studies
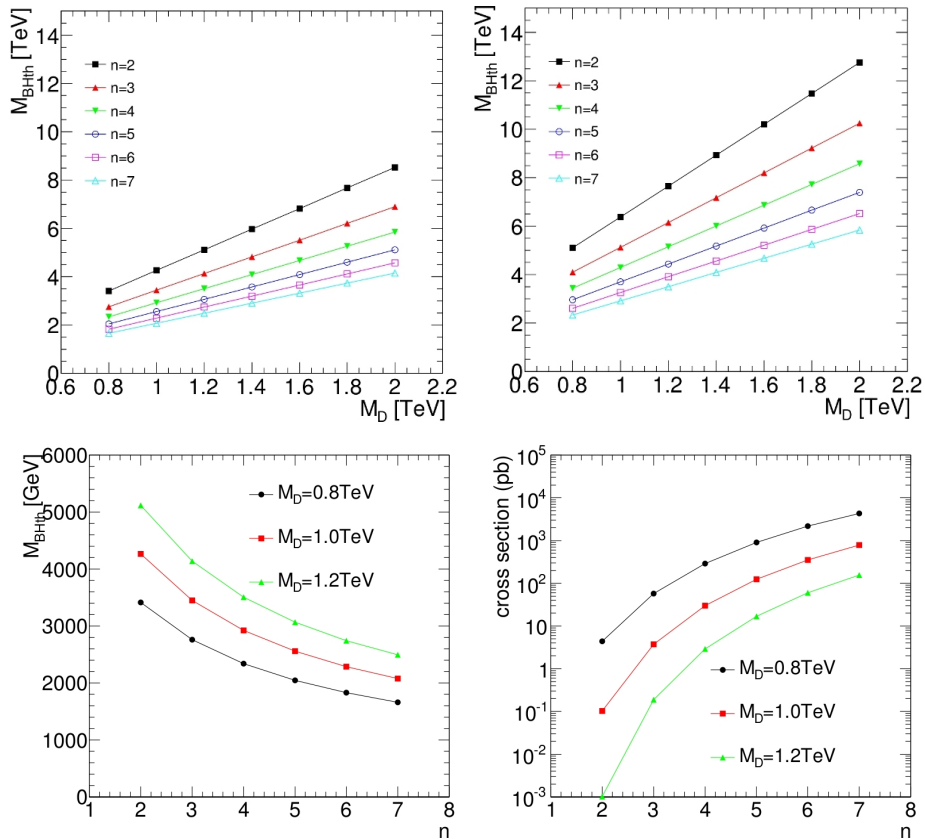
Figure H.1: Top: The threshold of black hole production with the condition $\lambda < r_s$ (on the left) and with $\lambda < r_h$ (on the right). Bottom: Mass thresholds calculated with Eq. 5.5 (a) and cross-sections for them (b) for each M_D as a function of n [135].

Figure H.2: p_T distributions of the leading jet (top left), the second leading jet (top right) to the fourth leading jet (bottom right) for data and QCD MC events. Yellow error bands represent the statistical uncertainties of the MC predictions [135].
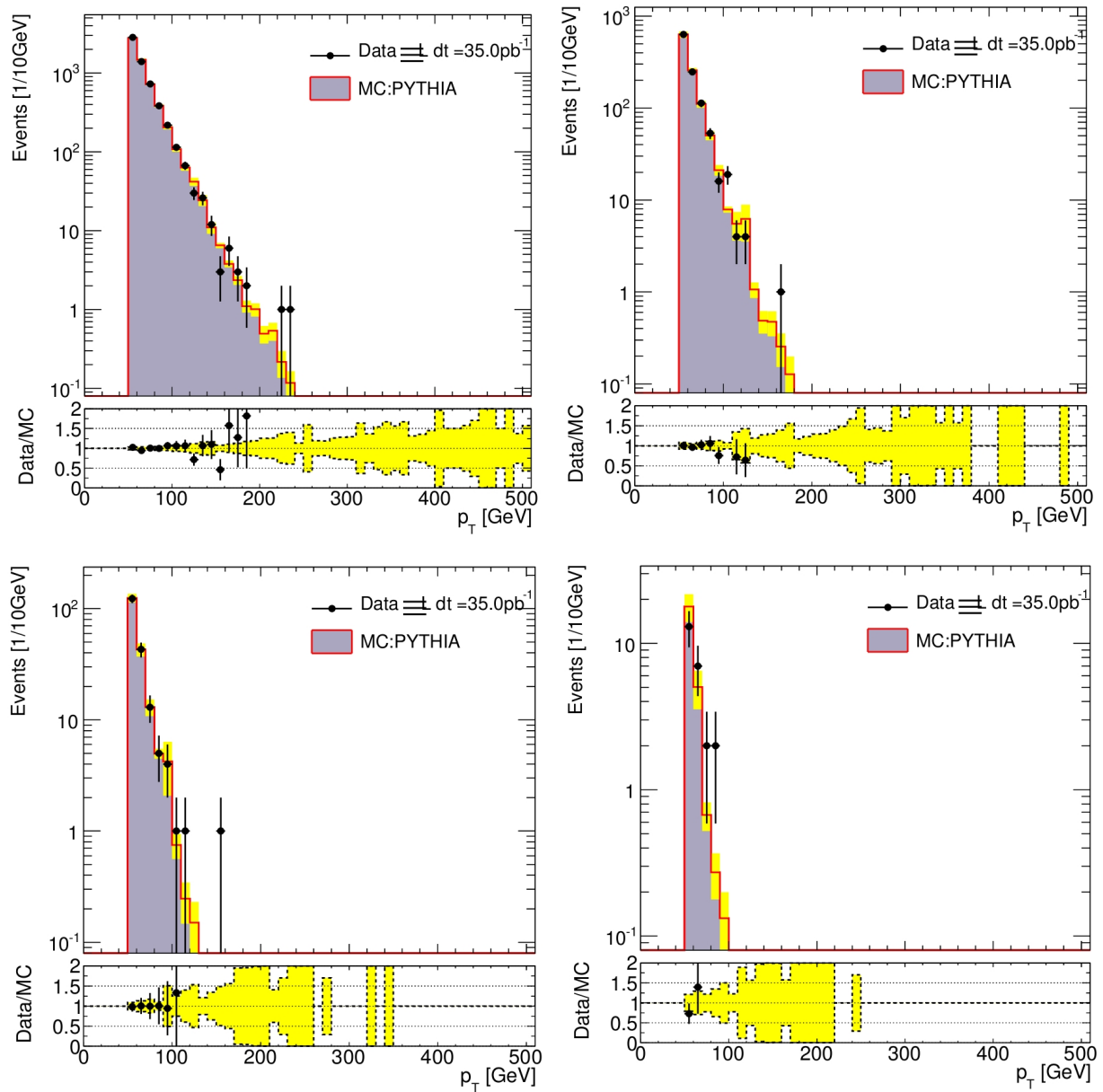
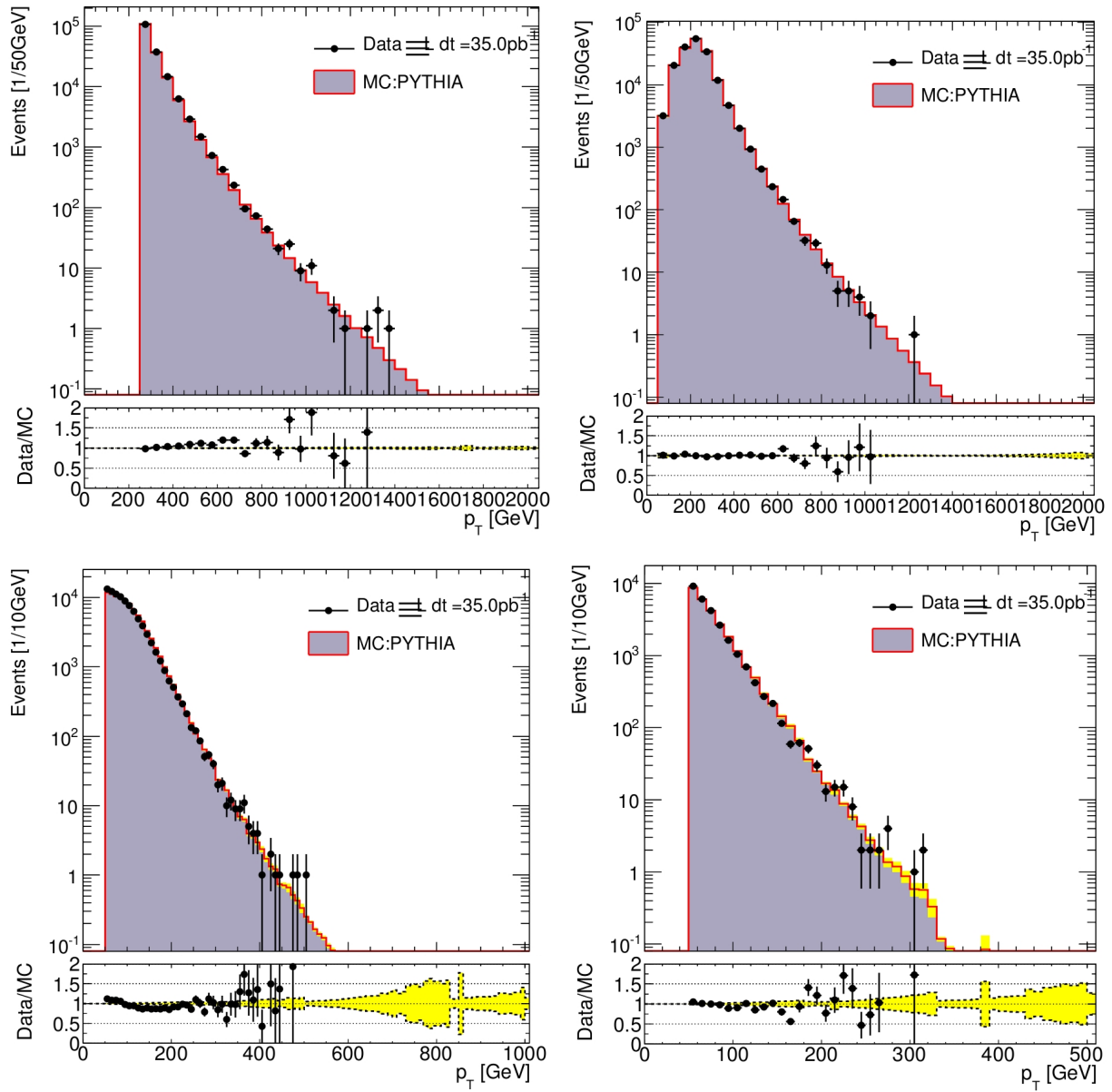Figure H.3: p_T distributions of the fifth leading jet (top left), the sixth leading jet (top right) to the eighth leading jet (bottom right) for data and QCD MC events. Yellow error bands represent the statistical uncertainties of the MC predictions [135].

Figure H.4: p_T distributions of the ninth leading jet (on the left) and the tenth leading jet (on the right) for data and QCD MC events. Yellow error bands represent the statistical uncertainties of the MC predictions [135].
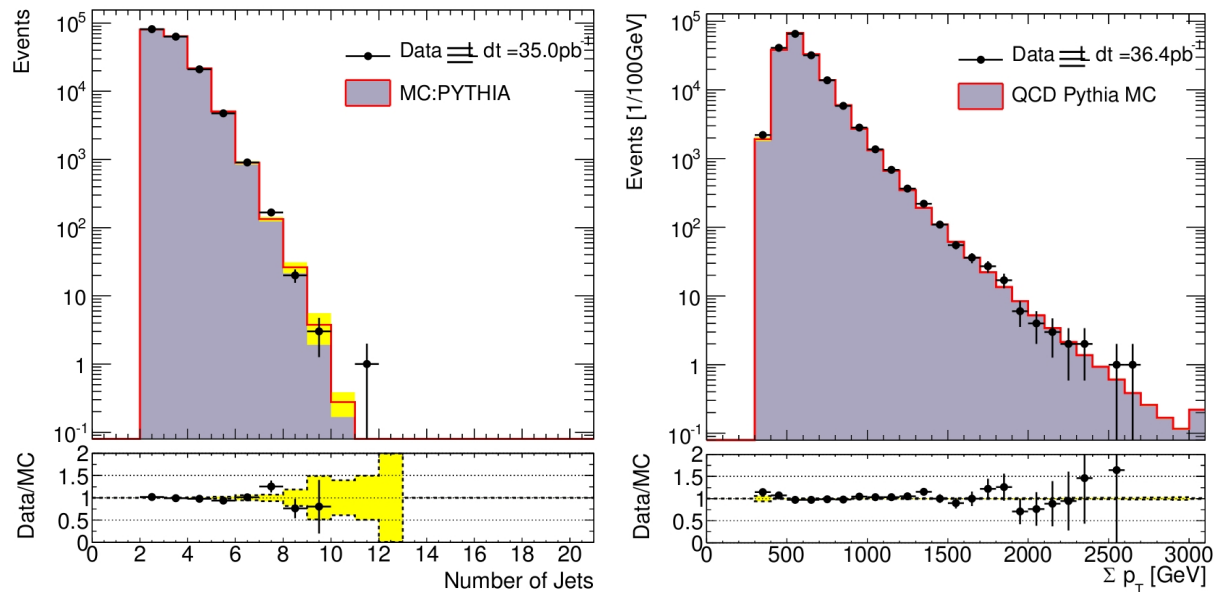
Figure H.5: N_J distribution (on the left) and $\sum p_T$ distribution for events with $N_J < 5$ (on the right) for data and QCD MC events. Yellow error bands represent the statistical uncertainties of the MC predictions [135].

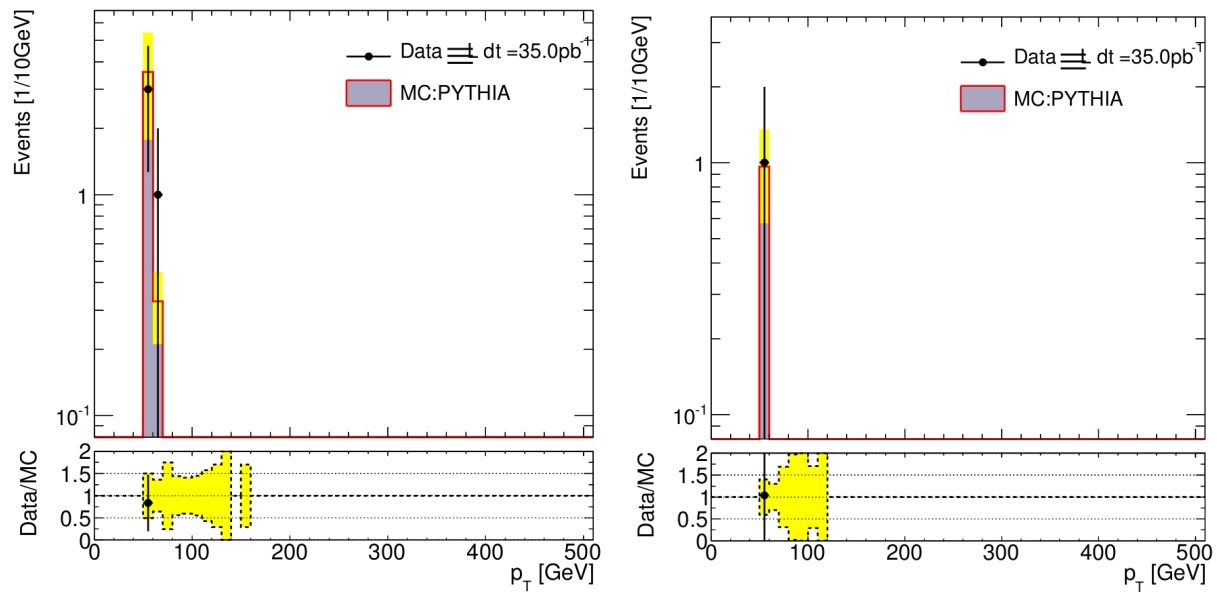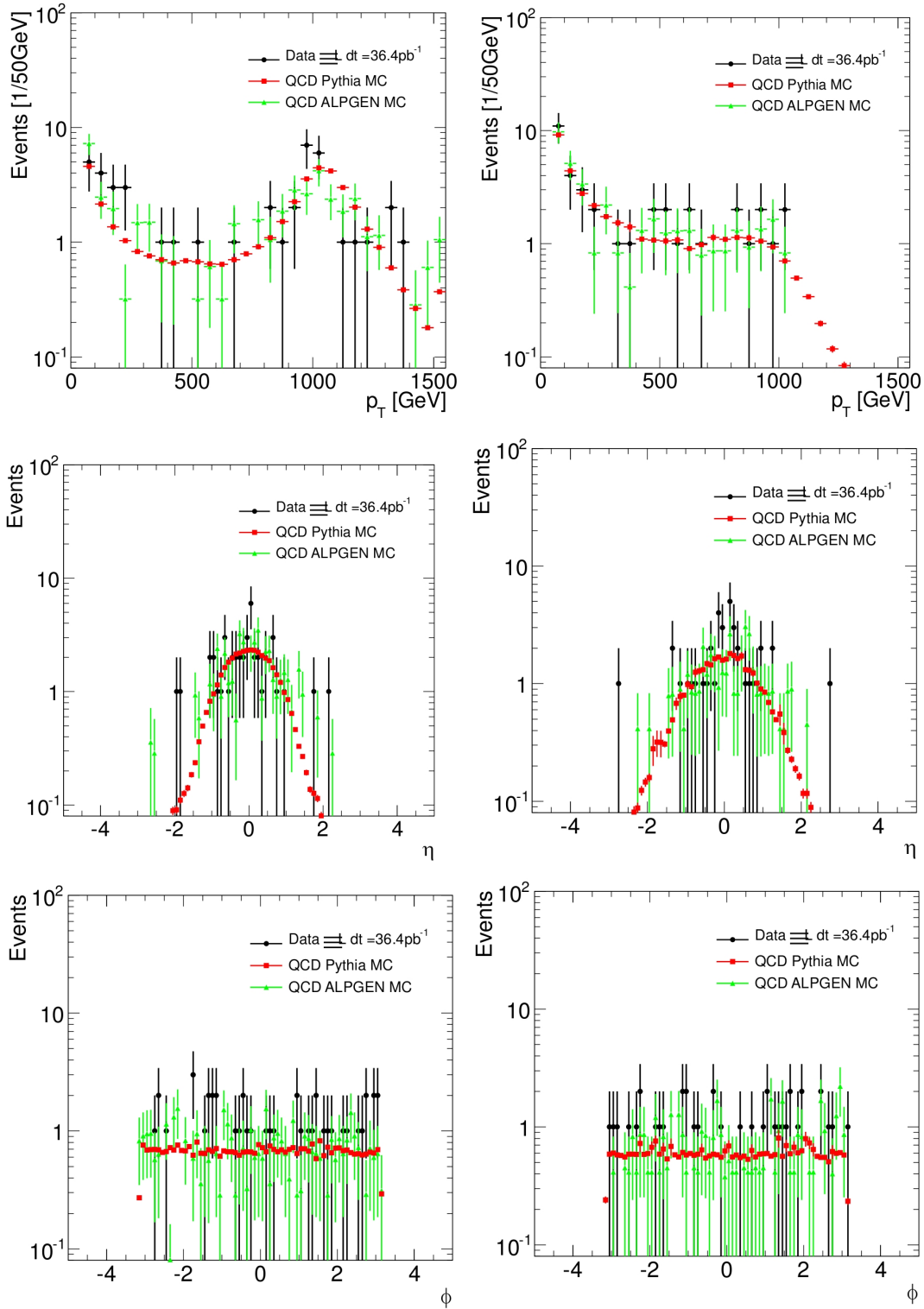Figure H.6: p_T, η and ϕ distributions of data, QCD Pythia and Alpgen MC events for $N_J < 5$ and $\sum p_T > 2000$ GeV (left column) and for $N_J \geq 5$ and $\sum p_T > 2000$ GeV (right column) [135].
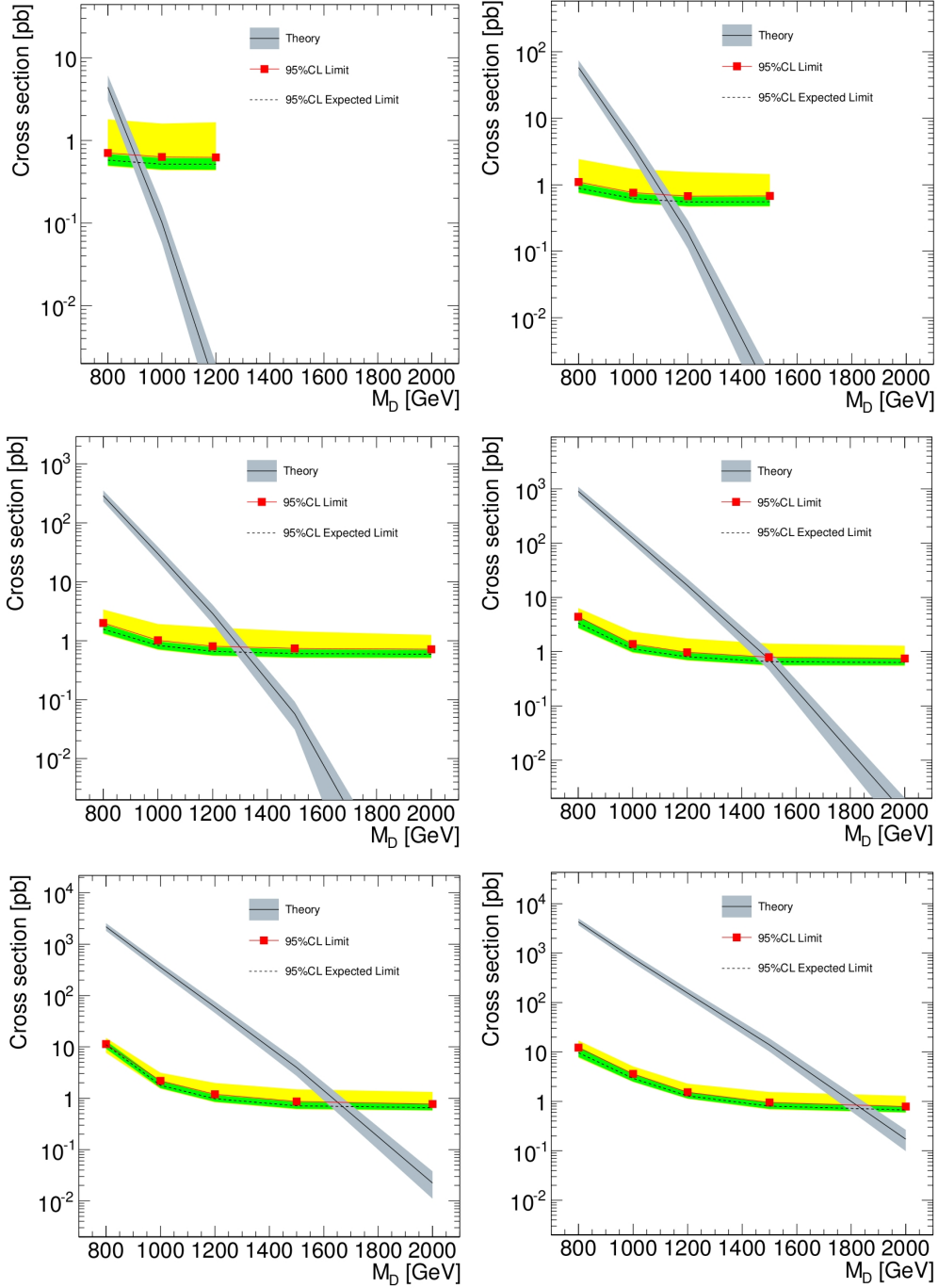
Figure H.7: 95% CL upper limit on the cross-section for $n = 2$ (3) on the top left (right), $n = 4$ (5) in the middle left (right) and $n = 6$ (7) at the bottom left (right) on the assumption of $\lambda < r_s$. The observed limit, the signal cross-section and the expected limit are shown by rectangles, a solid line and dashed line, respectively. The PDF uncertainty on the theoretical cross-section is shown by an error band and the 1σ (2σ) contour of the expected limit is shown in green (yellow) [135].
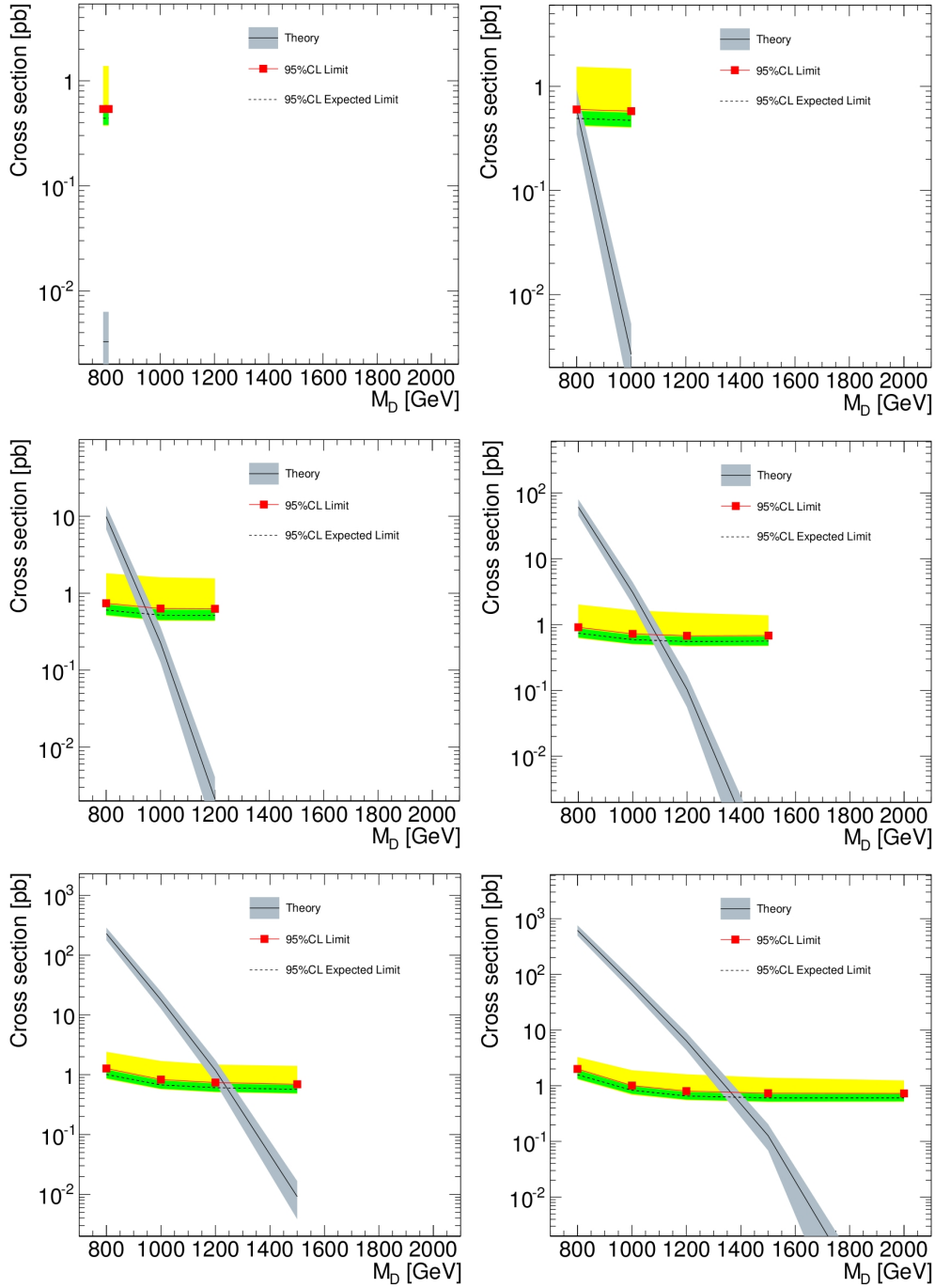
Figure H.8: 95% CL upper limit on the cross-section for $n = 2$ (3) on the top left (right), $n = 4$ (5) in the middle left (right) and $n = 6$ (7) at the bottom left (right) on the assumption of $\lambda < r_h$. The observed limit, the signal cross-section and the expected limit are shown by rectangles, a solid line and dashed line, respectively. The PDF uncertainty on the theoretical cross-section is shown by an error band and the 1σ (2σ) contour of the expected limit is shown in green (yellow) [135].

Figure H.9: 95% CL lower limit on M_D as a function of number of extra dimension. A solid (dashed) line is the result on the assumption $\lambda < r_s$ ($\lambda < r_h$). Filled histogram shows the lower limit by the previous collider experiments.

Bibliography

[1] M. Gell-Mann, **A Schematic Model of Baryons and Mesons**, Phys. Lett. 8, 214 (1964); M. Gell-Mann, **Nonleptonic Weak Decays and the Eightfold Way**, Phys. Rev. Lett. 12, 155 (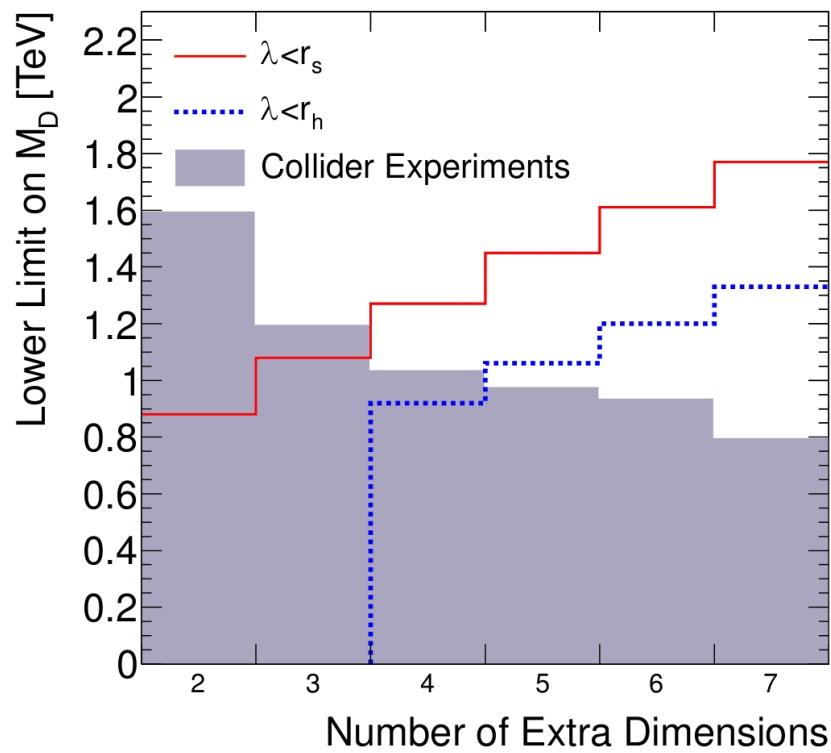1964); G. Zweig, **An SU(3) model for strong interaction symmetry and its breaking; Part I**, CERN-TH-401, 1964; G. Zweig, **An SU(3) model for strong interaction symmetry and its breaking; Part II**, CERN-TH-412, 1964

[2] Particle Data Group Collaboration, K. Nakamura, **Review of particle physics**, J. Phys. G37 (2010) 075021

[3] P. W. Higgs, **Broken Symmetries and the Masses of Gauge Bosons**, (1964) Phys. Rev. Lett. 13, pp. 508–509; P. W. Higgs, **Broken Symmetries, Massless Particles and Gauge Fields**, (1964) Physics Letters, 12 (2), pp. 132-133

[4] V. A. Bednyakov, N. D. Giokaris, A. V. Bednyakov, **On Higgs mass generation mechanism in the Standard Model**, Phys.Part.Nucl.39:13-36,2008, [arXiv:hep-ph/0703280v1]

[5] G. Abbiendi, et al., **Search for the Standard Model Higgs Boson at LEP**, Phys.Lett.B565: 61-75, 2003, [arXiv:hep-ex/0306033v1]

[6] The LEP Collaborations and the LEP Electroweak Working Group, **A Combination of Preliminary Electroweak Measurements and Constraints on the Standard Model**, [arXiv:hep-ex/0612034v2]

[7] The CDF Collaboration, the D0 Collaboration, the Tevatron New Physics, Higgs Working Group, **Combined CDF and D0 Upper Limits on Standard Model Higgs-Boson Production with 2.1 - 5.4 fb^{-1} of Data**, [arXiv:0911.3930v1 [hep-ex]]

[8] The CDF Collaboration, the D0 Collaboration, the Tevatron New Physics, Higgs Working Group, **Combined CDF and Dzero Upper Limits on Standard Model Higgs-Boson Production**, [arXiv:0712.2383v1 [hep-ex]]

[9] Fermilab Today, **Tevatron experiments report new Higgs search results**, http://www.fnal.gov/pub/today/images11/Higgs-mass-exclusion-March2011.jpg, [31. 03. 2011]

[10] A. D. Sakharov, **Violation of CP invariance, C asymmetry, and baryon asymmetry of the universe**, Sov. Phys. Usp. 34 (5), pp. 392–393, May 1991, http://www-itp.particle.uni-karlsruhe.de/~hofmann/lehre/GR/semSS2007LIT/ /Sakharov.pdf [28. 11. 2010]

[11] A. D. Dolgov, **Baryogenesis, 30 Years after**, [arXiv:hep-ph/9707419v1]; A. Riotto, **Theories of Baryogenesis**, [arXiv:hep-ph/9807454v2]; M. Trodden, **Electroweak Baryogenesis**, Rev.Mod.Phys.71:1463-1500,1999, [arXiv:hep-ph/9803479v2]

126

[12] T. Kaluza, **Zum Unitätsproblem der Physik**, Sitz.Preuss.Akad.Wiss. Phys Math.K1 (1921) 966

[13] J. van Dongen, **Einstein and the Kaluza-Klein particle**, Stud.Hist.Philos. Mod.Phys.33:185-210,2002, [arXiv:gr-qc/0009087v1]

[14] J. M. Overduin, P. S. Wesson, **Kaluza-Klein Gravity**, hys.Rept.283:303-380,1997, [arXiv:gr-qc/9805018v1]; M. J. Duff, **Kaluza-Klein Theory in Perspective**, [arXiv:hep-th/9410046v1]

[15] ESI Special Topics, **An Interview with Lisa Randall, Ph.D**, `http://www.esi-topics.com/brane/interviews/DrLisaRandall.html`, [11. 7. 2010]

[16] L. Randall, **Warped Passages: Untraveling the Mysteries of the Universe's Hidden Dimensions**, Harper Perennial (2006), 978-0060531096

[17] The ATLAS Collaboration, **The ATLAS Experiment at the CERN Large Hadron Collider**, 2008 JINST 3 S08003, `http://www.iop.org/EJ/article/1748-0221/3/08/S08003/` `/jinst8_08_s08003.pdf`, [22. 11. 2009]

[18] E. Richter-Was, **Prospect for the Higgs searches with the ATLAS detector**, ATL-PHYS-PROC-2009-044, [arXiv:0903.4198v1 [hep-ex]]

[19] CERN Document Server, **Civil Engineering in the ATLAS cavern**, `http://mediaarchive.cern.ch/MediaArchive/Photo/Public/2000/0002017/0002017_04/` `/0002017_04-A4-at-144-dpi.jpg`, [12. 9. 2010]

[20] CERN Document Server, **ATLAS beam pipe installation**, `http://mediaarchive.cern.ch/MediaArchive/Photo/Public/2008/0806011/0806011_01/` `/0806011_01-A4-at-144-dpi.jpg`, [12. 9. 2010]

[21] CERN Document Server, **Vue centrale du detecteur ATLAS avec ses huit toroides entourant le calorimetre avant son deplacement au centre du detecteur**, `http://mediaarchive.cern.ch/MediaArchive/Photo/Public/2005/0511013/0511013_01/` `/0511013_01-A4-at-144-dpi.jpg`, [2. 12. 2009]

[22] CERN Document Server, **ATLAS Magnet Toroid End-Cap**, `http://mediaarchive.cern.ch/MediaArchive/Photo/Public/2007/0705023/0705023_08/` `/0705023_08-A4-at-144-dpi.jpg`, [9. 1. 2010]

[23] The ATLAS Collaboration, **ATLAS High-Level Trigger, Data Acquisition and Controls Technical Design Report**, CERN-LHCC-2003-022 (2003)

[24] G.F.B. Riemann, Abh. Ges. Wiss. Gött. 13, 1 (1868)

[25] H. Minkowski, **Raum und Zeit**, Jahresberichte der Deutschen Mathematiker- Vereinigung, Leipzig, 1909. Online version: Wikisource, **Raum und Zeit (Minkowski)**, `http://de.wikisource.org/wiki/Raum_und_Zeit_(Minkowski)`, [10. 7. 2010]. English translation: V. Petkov, **Minkowski Spacetime: A Hundred Years Later**, ISBN 978-90-481-3474-8, Springer Dordrecht Heidelberg London New York (2010)

[26] L. O'Raifeartaigh, N. Straumann, **Early History of Gauge Theories and Kaluza-Klein Theories, with a Glance at Recent Developments**, [arXiv:hep-ph/9810524v2]

[27] E. Scholz, **The changing concept of matter in H. Weyl's thought, 1918 - 1930**, [arXiv:math/0409576v1]

[28] J. H. SCHWARZ, N. SEIBERG, **String Theory, Supersymmetry, Unification, and All That**, Rev.Mod.Phys.71:S112-S120,1999, [arXiv:hep-th/9803179v2]; M. J. DUFF, **The World in Eleven Dimensions: Supergravity, supermembranes and M-theory**, Taylor & Francis; 1 edition (January 1, 1999)

[29] K. BECKER, M. BECKER, J. H. SCHWARZ, **String Theory and M-Theory: A Modern Introduction**, Cambridge University Press; 1 edition (January 15, 2007)

[30] N. ARKANI-HAMED, M. SCHMALTZ, **Hierarchies without Symmetries from Extra Dimensions**, Phys.Rev. D61 (2000) 033005, [arXiv:hep-ph/9903417v1]; E. A. MIRABELLI, M. SCHMALTZ, **Yukawa Hierarchies from Split Fermions in Extra Dimensions**, Phys.Rev. D61 (2000) 113011, [arXiv:hep-ph/9912265v2]; N. ARKANI-HAMED, Y. GROSSMAN, M. SCHMALTZ, **Split Fermions in Extra Dimensions and Exponentially Small Cross-Sections at Future Colliders**, Phys.Rev. D61 (2000) 115004, [arXiv:hep-ph/9909411v1]

[31] A. COULTHURST, K. L. MCDONALD, B. H. J. MCKELLAR, **Suppressing Proton Decay By Separating Quarks And Leptons**, Phys.Rev.D74:127701,2006, [arXiv:hep-ph/0610345v2]; A. COULTHURST, **Generating the Baryon Asymmetry of the Universe in Split Fermion Models**, Phys.Rev. D73 (2006) 103517, [arXiv:hep-ph/0511244v3]; Y. NAGATANI, G. PEREZ, **Leptogenesis from Split Fermions**, JHEP0502:068,2005, [arXiv:hep-ph/0401070v1]; G. C. BRANCO, ANDRE DE GOUVEA, M. N. REBELO, **Split Fermions in Extra Dimensions and CP Violation**, Phys.Lett. B506 (2001) 115-122, [arXiv:hep-ph/0012289v2]

[32] N. ARKANI-HAMED, S. DIMOPOULOS, G. DVALI, **The Hierarchy Problem and New Dimensions at a Millimeter**, Phys.Lett.B429:263-272, 1998, [arXiv:hep-ph/9803315v1]

[33] I. ANTONIADIS, N. ARKANI-HAMED, S. DIMOPOULOS, G. DVALI, **New Dimensions at a Millimeter to a Fermi and Superstrings at a TeV**, Phys.Lett. B436:257-263, 1998, [arXiv:hep-ph/9804398v1]

[34] N. ARKANI-HAMED, S. DIMOPOULOS, G. DVALI, **Phenomenology, Astrophysics and Cosmology of Theories with Sub-Millimeter Dimensions and TeV Scale Quantum Gravity**, Phys.Rev. D59 (1999) 086004, [arXiv:hep-ph/9807344v1]

[35] ESI SPECIAL TOPICS, **An Interview with Dr. Nima Arkani-Hamed**, http://www.esi-topics.com/brane/interviews/DrNimaArkani-Hamed.html, [1. 8. 2010]

[36] C. D. HOYLE, D. J. KAPNER, B. R. HECKEL, E. G. ADELBERGER, J. H. GUNDLACH, U. SCHMIDT, H. E. SWANSON, **Sub-millimeter Tests of the Gravitational Inverse-square Law**, Phys.Rev.D70:042004,2004, [arXiv:hep-ph/0405262v2]

[37] E. G. ADELBERGER, B. R. HECKEL, A. E. NELSON, **Tests of the Gravitational Inverse-Square Law**, Ann.Rev.Nucl.Part.Sci.53:77-121,2003, [arXiv:hep-ph/0307284v1]

[38] J. C. LONG, H. W. CHAN, A. B. CHURNSIDE, E. A. GULBIS, M. C. M. VARNEY, J. C. PRICE, **New Experimental Limits on Macroscopic Forces Below 100 Microns**, Letter version published in Nature 421, 922-925 (2003), [arXiv:hep-ph/0210004v3]

[39] V. BARGER, T. HAN, C. KAO, R.-J. ZHANG, **Astrophysical Constraints on Large Extra Dimensions**, Phys.Lett.B461:34-42,1999, [arXiv:hep-ph/9905474v2]

[40] S. CULLEN, M. PERELSTEIN, **SN1987A Constraints on Large Compact Dimensions**, Phys.Rev.Lett. 83 (1999) 268-271, [arXiv:hep-ph/9903422v1]

[41] HUBBLE SITE, **NASA's Hubble Telescope Celebrates SN1987A's 20th Anniversary**, STScI-2007-10, `http://imgsrc.hubblesite.org/hu/db/images/hs-2007-10-a-print.jpg`, [20. 3. 2010]

[42] G. DVALI, S.-H. HENRY TYE, **Brane Inflation**, Phys.Lett. B450 (1999) 72-82, [arXiv:hep-ph/9812483v1]

[43] G. DVALI, G. GABADADZE, **Non-conservation of Global Charges in the Brane Universe and Baryogenesis**, Phys.Lett. B460 (1999) 47-57, [arXiv:hep-ph/9904221v3]

[44] M. NOVELLO, R. P. NEVES, **The mass of the graviton and the cosmological constant**, [arXiv:gr-qc/0210058v2]; A. S. GOLDHABER, M. M. NIETO, **Photon and Graviton Mass Limits**, [arXiv:0809.1003v4 [hep-ph]]

[45] J. KHOURY, B. A. OVRUT, P. J. STEINHARDT, N. TUROK, **The Ekpyrotic Universe: Colliding Branes and the Origin of the Hot Big Bang**, Phys.Rev.D64:123522,2001, [arXiv:hep-th/0103239v3]; J. KHOURY, B. A. OVRUT, P. J. STEINHARDT, N. TUROK, **Density Perturbations in the Ekpyrotic Scenario**, Phys.Rev.D66:046005,2002, [arXiv:hep-th/0109050v4]; R. BRANDENBERGER, F. FINELLI, **On the Spectrum of Fluctuations in an Effective Field Theory of the Ekpyrotic Universe**, JHEP 0111:056,2001, [arXiv:hep-th/0109004v4]

[46] P. J. STEINHARDT, N. TUROK, **Cosmic Evolution in a Cyclic Universe**, Phys.Rev.D65:126003,2002, [arXiv:hep-th/0111098v2]; P. J. STEINHARDT, N. TUROK, **A Cyclic Model of the Universe**, [arXiv:hep-th/0111030v2]; A. LINDE, **Inflationary Theory versus Ekpyrotic/Cyclic Scenario**, [arXiv:hep-th/0205259v1]

[47] R. KALLOSH, L. KOFMAN, A. LINDE, **Pyrotechnic Universe**, Phys.Rev.D64:123523,2001, [arXiv:hep-th/0104073v3]; S. KACHRU, R. KALLOSH, A. LINDE, J. MALDACENA, L. MCALLISTER, S. P. TRIVEDI, **Towards Inflation in String Theory**, JCAP 0310:013,2003, [arXiv:hep-th/0308055v2]

[48] N. ARKANI-HAMED, S. DIMOPOULOS, N. KALOPER, J. MARCH-RUSSELL, **Rapid Asymmetric Inflation and Early Cosmology in Theories with Sub-Millimeter Dimensions**, Nucl.Phys. B567 (2000) 189-228, [arXiv:hep-ph/9903224v1]

[49] T. HAN, J. D. LYKKEN, REN-JIE ZHANG, **On Kaluza-Klein States from Large Extra Dimensions**, Phys.Rev. D59 (1999) 105006, [arXiv:hep-ph/9811350v4]; S. CULLEN, M. PERELSTEIN, M. E. PESKIN, **TeV Strings and Collider Probes of Large Extra Dimensions**, Phys.Rev. D62 (2000) 055012, [arXiv:hep-ph/0001166v3]; J. HEWETT, M. SPIROPULU, **Particle Physics Probes Of Extra Spacetime Dimensions**, Ann.Rev.Nucl.Part.Sci.52:397-424,2002, [arXiv:hep-ph/0205106v1]

[50] J. L. HEWETT, **Indirect Collider Signals for Extra Dimensions**, Phys.Rev.Lett. 82 (1999) 4765-4768, [arXiv:hep-ph/9811356v2]; S. NUSSINOV, R. SHROCK, **Some Remarks on Theories with Large Compact Dimensions and TeV-Scale Quantum Gravity**, Phys.Rev. D59 (1999) 105002, [arXiv:hep-ph/9811323v1]; G. F. GIUDICE, A. STRUMIA, **Constraints on extra-dimensional theories from virtual-graviton exchange**, Nucl.Phys.B663:377-393, 2003, [arXiv:hep-ph/0301232v1]

[51] G. F. GIUDICE, R. RATTAZZI, J. D. WELLS, **Quantum Gravity and Extra Dimensions at High-Energy Colliders**, Nucl.Phys. B544 (1999) 3-38, [arXiv:hep-ph/9811291v2]

[52] E. A. MIRABELLI, M. PERELSTEIN, M. E. PESKIN, **Collider Signatures of New Large Space Dimensions**, Phys.Rev.Lett. 82 (1999) 2236-2239, [arXiv:hep-ph/9811337v4]

[53] L. Vacavant, I. Hinchliffe, **Model Independent Extra-dimension signatures with AT-LAS**, [arXiv:hep-ex/0005033v1]

[54] S. Ask, **Search For Extra Dimensions At LEP**, [arXiv:hep-ex/0410004v1]

[55] L3 Collaboration, **Search for Low Scale Gravity Effects in e^+e^- Collisions at LEP**, Phys.Lett.B464:135-144,1999, [arXiv:hep-ex/9909019v1]

[56] V. Krutelyov, **Searches for Large Extra Dimensions at the Tevatron**, FERMILAB-CONF-08-218-E, [arXiv:0807.0645v1]

[57] D0 Collaboration, V. M. Abazov, et al, **Search for Large Extra Spatial Dimensions in Dimuon Production with the D0 Detector**, Phys.Rev.Lett.95:161602,2005, [arXiv:hep-ex/0506063v2]; D0 Collaboration: V. M. Abazov, et al, **Search for Large Extra Dimensions via Single Photon plus Missing Energy Final States at sqrt(s) = 1.96 TeV**, Phys.Rev.Lett.101:011601,2008, [arXiv:0803.2137v2]; D0 Collaboration: V. M. Abazov, et al, **Search for Large extra spatial dimensions in the dielectron and diphoton channels in $p\bar{p}$ collisions at $\sqrt{s} = 1.96$ TeV**, Phys.Rev.Lett.102:051601,2009, [arXiv:0809.2813v1]; D0 Collaboration: V. M. Abazov et al., **Measurement of dijet angular distributions at sqrt(s) = 1.96 TeV and searches for quark compositeness and extra spatial dimensions**, Phys.Rev.Lett.103:191803,2009, [arXiv:0906.4819v2]

[58] J. Ellis et al, **Review of the safety of LHC collisions**, 2008 J. Phys. G: Nucl. Part. Phys. 35 115004, `http://iopscience.iop.org/0954-3899/35/11/115004`, [3. 9. 2010]

[59] R. Casadio, S. Fabi, B. Harms, **Possibility of Catastrophic Black Hole Growth in the Warped Brane-World Scenario at the LHC**, Phys.Rev.D80:084036,2009, [arXiv:0901.2948v3 [hep-ph]]

[60] L. Randall, R. Sundrum, **An Alternative to Compactification**, Phys.Rev. Lett. 83:4690-4693, 1999, [arXiv:hep-th/9906064v1]

[61] L. Randall, R. Sundrum, **A Large Mass Hierarchy from a Small Extra Dimension**, Phys.Rev.Lett. 83:3370-3373, 1999, [arXiv:hep-ph/9905221v1]

[62] K. Riesselmann, **The Symmetry Magazine, logbook: extra dimensions**, `http://www.symmetrymagazine.org/images/200506/logbook.jpg`, [2. 8. 2010]

[63] V. A. Rubakov, M. E. Shaposhnikov, **Do we live inside a domain wall?**, Phys. Lett. B 125, 136-139 (1983)

[64] N. Arkani-Hamed, S. Dimopoulos, N. Kaloper, R. Sundrum, **A Small Cosmological Constant from a Large Extra Dimension**, Phys.Lett.B480:193-199,2000, [arXiv:hep-th/0001197v2]; S. Kachru, M. Schulz, E. Silverstein, **Self-tuning flat domain walls in 5d gravity and string theory**, Phys.Rev.D62:045021,2000, [arXiv:hep-th/0001206v1]; C. Csaki, J. Erlich, C. Grojean, T. Hollowood, **General Properties of the Self-tuning Domain Wall Approach to the Cosmological Constant Problem**, Nucl.Phys.B584:359-386,2000, [arXiv:hep-th/0004133v2]; C. Csaki, J. Erlich, C. Grojean, **Gravitational Lorentz Violations and Adjustment of the Cosmological Constant in Asymmetrically Warped Spacetimes**, Nucl.Phys.B604:312-342,2001, [arXiv:hep-th/0012143v3]

[65] H. VERLINDE, **Holography and Compactification**, Nucl.Phys. B580 (2000) 264-274, [arXiv:hep-th/9906182v1]; R. RATTAZZI, A. ZAFFARONI, **Comments on the Holographic Picture of the Randall-Sundrum Model**, JHEP 0104:021,2001, [arXiv:hep-th/0012248v2]; M. PEREZ-VICTORIA, **Randall-Sundrum models and the regularized AdS/CFT correspondence**, JHEP 0105 (2001) 064, [arXiv:hep-th/0105048v2]

[66] T. APPELQUIST, HSIN-CHIA CHENG, B. A. DOBRESCU, **Bounds on Universal Extra Dimensions**, Phys.Rev. D64 (2001) 035002, [arXiv:hep-ph/0012100v2]

[67] C. MACESANU, C. D. MCMULLEN, S. NANDI, **Collider Implications of Universal Extra Dimensions**, Phys.Rev. D66 (2002) 015009, [arXiv:hep-ph/0201300v2]

[68] T. G. RIZZO, **Probes Of Universal Extra Dimensions at Colliders**, Phys.Rev. D64 (2001) 095010, [arXiv:hep-ph/0106336v1]

[69] I. ANTONIADIS, K. BENAKLI, **Limits on extra dimensions in orbifold compactifications of superstrings**, Phys.Lett.B326:69-78,1994, [arXiv:hep-th/9310151v1]; K. R. DIENES, E. DUDAS, T. GHERGHETTA, **Extra Spacetime Dimensions and Unification**, Phys.Lett. B436 (1998) 55-65, [arXiv:hep-ph/9803466v2]; K. R. DIENES, E. DUDAS, T. GHERGHETTA, **Grand Unification at Intermediate Mass Scales through Extra Dimensions**, Nucl.Phys. B537 (1999) 47-108, [arXiv:hep-ph/9806292v2]

[70] CH. D. CARONE, **Electroweak Constraints on Extended Models with Extra Dimensions**, Phys.Rev. D61 (2000) 015008, [arXiv:hep-ph/9907362v1]; A. DELGADO, A. POMAROL, M. QUIROS, **Electroweak and Flavor Physics in Extensions of the Standard Model with Large Extra Dimensions**, JHEP0001:030,2000, [arXiv:hep-ph/9911252v1]

[71] HSIN-CHIA CHENG, K. T. MATCHEV, M. SCHMALTZ, **Bosonic Supersymmetry? Getting Fooled at the LHC**, Phys.Rev.D66:056006,2002, [arXiv:hep-ph/0205314v1]

[72] C. MACESANU, C.D. MCMULLEN, S. NANDI, **New Signal for Universal Extra Dimensions**, Phys.Lett. B546 (2002) 253-260, [arXiv:hep-ph/0207269v2]

[73] G. BHATTACHARYYA, A. DATTA, S. K. MAJEE, A. RAYCHAUDHURI, **Exploring the Universal Extra Dimension at the LHC**, Nucl. Phys. B 821 (2009) 48-64, [arXiv:0904.0937v2 [hep-ph]]; B. BHATTACHERJEE, K. GHOSH, **Search for the minimal universal extra dimension model at the LHC with $\sqrt{s} = 7$ TeV**, TIFR/TH/10-14, RECAPP-HRI-2010-009, [arXiv:1006.3043v1 [hep-ph]]; D. CHOUDHURY, A. DATTA, K. GHOSH, **Deciphering Universal Extra Dimension from the top quark signals at the CERN LHC**, [arXiv:0911.4064v3 [hep-ph]]

[74] C. MACESANU, **The Phenomenology of Universal Extra Dimensions at Hadron Colliders**, Int.J.Mod.Phys. A21 (2006) 2259-2296, [arXiv:hep-ph/0510418v1]

[75] T. FLACKE, D. HOOPER, J. MARCH-RUSSELL, **Improved Bounds on Universal Extra Dimensions and Consequences for LKP Dark Matter**, Phys.Rev.D73:095002,2006, [arXiv:hep-ph/0509352v2]

[76] HSIN-CHIA CHENG, K. T. MATCHEV, M. SCHMALTZ, **Radiative Corrections to Kaluza-Klein Masses**, Phys.Rev.D66:036005,2002, [arXiv:hep-ph/0204342v1]

[77] G. BHATTACHARYYA, P. DEY, A. KUNDU, A. RAYCHAUDHURI, **Probing Universal Extra Dimension at the International Linear Collider**, Phys.Lett. B628 (2005) 141-147, [arXiv:hep-ph/0502031v2]

[78] B. A. Dobrescu, E. Poppitz, **Number of Fermion Generations Derived from Anomaly Cancellation**, Phys.Rev.Lett. 87 (2001) 031801, [arXiv:hep-ph/0102010v2]

[79] N. Arkani-Hamed, Hsin-Chia Cheng, B. A. Dobrescu, L. J. Hall, **Self-Breaking of the Standard Model Gauge Symmetry**, Phys.Rev. D62 (2000) 096006, [arXiv:hep-ph/0006238v2]

[80] N. R. Shah, C. E. M. Wagner, **Gravitons and Dark Matter in Universal Extra Dimensions**, Phys.Rev.D74:104008,2006, [arXiv:hep-ph/0608140v2]

[81] G. D. Kribs, **TASI 2004 Lectures on the Phenomenology of Extra Dimensions**, [arXiv:hep-ph/0605325v1]

[82] V. H. Satheesh Kumar, P. K. Suresh, **Gravity and Large Extra Dimensions**, [arXiv:hep-th/0606194v1]

[83] C. Csaki, **TASI Lectures on Extra Dimensions and Branes**, [arXiv:hep-ph/0404096v1]

[84] R. Tabbash, **Physics of Extra Dimensions**, [arXiv:hep-ph/0111334v1]

[85] J. Michell, **On the means of discovering the distance, magnitude etc. of the fixed stars ...**, Philosophical Transactions of the Royal Society, Vol. 74, (1784), `http://www.relativitybook.com/resources/Michell_1783.html` [9. 12. 2010]

[86] K. Schwarzschild (translation and foreword by S. Antoci and A. Loinger), **On the gravitational field of a mass point according to Einstein's theory**, Sitzungsber.Preuss.Akad.Wiss.Berlin (Math.Phys.) 1916, 189-196, [arXiv:physics/9905030v1]; K. Schwarzschild (translation by S. Antoci), **On the gravitational field of a sphere of incompressible fluid according to Einstein's theory**, Sitzungsber.Preuss.Akad.Wiss.Berlin (Math.Phys.) 1916, 424-434, [arXiv:physics/9912033v1]

[87] S. Chandrasekhar, **The Highly Collapsed Configurations of a Stellar Mass**, Monthly Notices of the Royal Astronomical Society 91 (1931), 456–466, `http://adsabs.harvard.edu/abs/1931MNRAS..91..456C`, [9. 12. 2010]; S. Chandrasekhar, **The Highly Collapsed Configurations of a Stellar Mass (second paper)**, Monthly Notices of the Royal Astronomical Society, 95 (1935), pp. 207-225, `http://adsabs.harvard.edu/abs/1935MNRAS..95..207C`, [9. 12. 2010]; S. Chandrasekhar, **The Maximum Mass of Ideal White Dwarfs**, Astrophysical Journal 74 (1931), pp. 81–82, `http://adsabs.harvard.edu/abs/1931ApJ....74...81C`, [9. 12. 2010]

[88] J. R. Oppenheimer, G. M. Volkoff, **On Massive Neutron Cores**, Phys.Rev.55, 374-381 (1939)

[89] R. P. Kerr, **Gravitational Field of a Spinning Mass as an Example of Algebraically Special Metrics**, Phys. Rev. Lett. 11, 237–238 (1963)

[90] E. T. Newman, E. Couch, K. Chinnapared, A. Exton, A. Prakash, R. Torrence, **Metric of a Rotating, Charged Mass**, J. Math. Phys. 6, 918 (1965)

[91] E. Brown, **Ann E. Ewing dies; science journalist turned nation's eyes to "black holes"**, The Washington Post, Sunday, August 1, 2010, `http://www.washingtonpost.com/wp-dyn/content/article/2010/07/31/AR2010073102772.html`, [1. 12. 2010]

[92] Wikipedia, the Free Encyclopedia, **Cygnus X-1**, `http://en.wikipedia.org/wiki/File:Cygnus_constellation_map.svg`, [2. 12. 2010]

[93] M. J. Reid, **Is there a Supermassive Black Hole at the Centre of the Milky Way?**, Int.J.Mod.Phys.D18:889-910,2009, [arXiv:0808.2624v1 [astro-ph]]

[94] S. Gillessen, et al., **Monitoring stellar orbits around the Massive Black Hole in the Galactic Center**, The Astrophysical Journal 692: 1075–1109, [arXiv:0810.4674v1 [astro-ph]]

[95] N O'Neill **Beyond Any Reasonable Doubt: A Supermassive Black Hole Lives in Centre of Our Galaxy**, Universe Today, December 10, 2008, `http://www.universetoday.com/22104/` `/beyond-any-reasonable-doubt-a-supermassive-black-hole-lives-in-centre-of-our-galaxy` [3. 12. 2010]

[96] J. M. Bardeen, B. Carter, S. W. Hawking, **The four laws of black hole mechanics**, Comm. Math. Phys. Volume 31, Number 2 (1973), 161-170

[97] S. W. Hawking, **Particle creation by black holes**, Comm. Math. Phys. Volume 43, Number 3 (1975), 199-220

[98] P. D. D'Eath, P. N. Payne, **Gravitational radiation in black-hole collisions at the speed of light. I. Perturbation treatment of the axisymmetric collision**, Phys. Rev. D 46, 658–674 (1992); P. D. D'Eath, P. N. Payne, **Gravitational radiation in black-hole collisions at the speed of light. II. Reduction to two independent variables and calculation of the second-order news function**, Phys. Rev. D 46, 675–693 (1992); P. D. D'Eath, P. N. Payne, **Gravitational radiation in black-hole collisions at the speed of light. III. Results and conclusions**, Phys. Rev. D 46, 694–701 (1992)

[99] L. A. Anchordoqui, J. L. Feng, H. Goldberg, A. D. Shapere, **Black Holes from Cosmic Rays: Probes of Extra Dimensions and New Limits on TeV-Scale Gravity**, Phys.Rev.D65:124027,2002, [arXiv:hep-ph/0112247v3]; S. N. Solodukhin, **Classical and quantum cross-section for black hole production in particle collisions**, Phys.Lett. B533 (2002) 153-161, [arXiv:hep-ph/0201248v2]

[100] M. Cavaglia, **Black hole and brane production in TeV gravity: A review**, Int.J.Mod.Phys. A18 (2003) 1843-1882, [arXiv:hep-ph/0210296v1]

[101] D. M. Gingrich, **Black Hole Production at the Large Hadron Collider**, Int.J.Mod.Phys.A22:5685-5699,2007, [arXiv:0706.0627v1 [hep-ph]]; D. M. Gingrich, **Black Hole Cross Section at the Large Hadron Collider**, Int.J.Mod.Phys. A21 (2006) 6653-6676, [arXiv:hep-ph/0609055v2]

[102] D. M. Eardley, S. B. Giddings, **Classical black hole production in high-energy collisions**, Phys. Rev. D 66, 044011 (2002); H. Yoshino, Y. Nambu, **Black hole formation in the grazing collision of high-energy particles**, Phys. Rev. D 67, 024009 (2003); H. Yoshino, V. S. Rychkov, **Improved analysis of black hole formation in high-energy particle collisions**, Phys. Rev. D 71, 104028 (2005)

[103] S. B. Giddings, S. Thomas, **High energy colliders as black hole factories: The end of short distance physics**, Phys. Rev. D 65, 056010 (2002)

[104] S. S. Gubser, I. R. Klebanov, A. A. Tseytlin, **String theory and classical absorption by three-branes**, Nucl. Phys. B499, 217 (1997)

[105] D. N. Page, **Particle emission rates from a black hole: Massless particles from an uncharged, nonrotating hole**, Phys. Rev. D 13, 198–206 (1976); D. N. Page, **Particle emission rates from a black hole. II. Massless particles from a rotating hole**, Phys. Rev. D 14, 3260–3273 (1976); W. G. Unruh, **Absorption cross section of small black holes**, Phys. Rev. D14, 3251 (1976)

[106] C. W. MISNER, K. T. THORNE, J. A. WHEELER, **Gravitation**, Freeman, San Fransisco, 1973

[107] G. W. GIBBONS, **Vacuum Polarization and the Spontaneous Loss of Charge by Black Holes**, Commun. Math. Phys. 44, 245 (1975); B. CARTER, **Charge and Particle Conservation in Black-Hole Decay**, Phys. Rev. Lett. 33, 558 (1974).

[108] P. CHEN, R. J. ADLER, **Black Hole Remnants and Dark Matter**, Nucl.Phys.Proc.Suppl. 124 (2003) 103-106, [arXiv:gr-qc/0205106v1]; J. D. BARROW, E. J. COPELAND, A. R. LIDDLE, **The cosmology of black hole relics**, Phys. Rev. D 46, 645 (1992)

[109] T. BANKS, **Lectures On Black Hole Evaporation and Information Loss**, Nucl.Phys.Proc.Suppl. 41 (1995) 21-65, [arXiv:hep-th/9412131v1]; T. BANKS, M. O'LOUGHLIN, A. STROMINGER, **Black Hole Remnants and the Information Puzzle**; S. B. GIDDINGS, **Comments on information loss and remnants**, Phys.Rev. D49 (1994) 4078-4088, [arXiv:hep-th/9310101v2]; S.B. GIDDINGS, **Constraints on Black Hole Remnants**, Phys.Rev. D49 (1994) 947-957, [arXiv:hep-th/9304027v3]

[110] R. C. MYERS, **Higher-dimensional black holes in compactified space-times**, Phys. Rev. D 35, 455–466 (1987); R. C. MYERS, M. J. PERRY, **Black holes in higher dimensional space-times**, Annals of Physics, 172, Issue 2, p.304-347

[111] S. CREEK, O. EFTHIMIOU, P. KANTI, K. TAMVAKIS, **Greybody Factors for Brane Scalar Fields in a Rotating Black-Hole Background**, Phys.Rev.D75:084043,2007, [arXiv:hep-th/0701288v2]; S. CREEK, O. EFTHIMIOU, P. KANTI, K. TAMVAKIS, **Greybody factors in a rotating black-hole background-II: fermions and gauge bosons**, Phys.Rev.D76:104013,2007, [arXiv:0707.1768v2 [hep-th]]

[112] G. DUFFY, C. HARRIS, P. KANTI, E. WINSTANLEY, **Brane decay of a $(4+n)$-dimensional rotating black hole: spin-0 particles**, JHEP 0509 (2005) 049, [arXiv:hep-th/0507274v1]; M. CASALS, P. KANTI, E. WINSTANLEY, **Brane Decay of a $(4+n)$-Dimensional Rotating Black Hole. II: spin-1 particles**, JHEP0602:051,2006, [arXiv:hep-th/0511163v1]; M. CASALS, S. R. DOLAN, P. KANTI, E. WINSTANLEY, **Brane Decay of a $(4+n)$-Dimensional Rotating Black Hole. III: spin-1/2 particles**, JHEP 0703:019,2007, [arXiv:hep-th/0608193v2]

[113] F. R. TANGHERLINI, **Atoms in Higher Dimensions**, Nuovo Cimento 14 (27), 636 (1963)

[114] E. JUNG, D. K. PARK, **Validity of Emparan-Horowitz-Myers argument in Hawking radiation into massless spin-2 fields**, Mod. Phys. Lett. A, Vol. 22, No. 22 (2007) pp. 1635-1642, [arXiv:hep-th/0612043v3]

[115] M. CASALS, S. R. DOLAN, P. KANTI, E. WINSTANLEY, **Bulk emission of scalars by a rotating black hole**, JHEP 0806:071,2008, [arXiv:0801.4910v2 [hep-th]]

[116] CH. M. HARRIS, P. KANTI, **Hawking Radiation from a $(4+n)$-dimensional Black Hole: Exact Results for the Schwarzschild Phase**, JHEP 0310 (2003) 014, [arXiv:hep-ph/0309054v2]

[117] S. CREEK, O. EFTHIMIOU, P. KANTI, K. TAMVAKIS, **Scalar Emission in the Bulk in a Rotating Black Hole Background**, Phys.Lett.B656:102-111,2007, [arXiv:0709.0241v2 [hep-th]]; T. KOBAYASHI, M. NOZAWA, Y. TAKAMIZU, **Bulk scalar emission from a rotating black hole pierced by a tense brane**, Phys.Rev.D77:044022,2008, [arXiv:0711.1395v4 [hep-th]]

[118] V. CARDOSO, M. CAVAGLIA, L. GUALTIERI, **Black hole particle emission in higher-dimensional spacetimes**, Phys.Rev.Lett. 96 (2006) 071301, [arXiv:hep-th/0512002v3]

[119] S. Creek, O. Efthimiou, P. Kanti, K. Tamvakis, **Graviton Emission in the Bulk from a Higher-Dimensional Schwarzschild Black Hole**, Phys.Lett.B635:39-49,2006, [arXiv:hep-th/0601126v2]; P. Kanti, Hideo Kodama, R. A. Konoplya, N. Pappas, A. Zhidenko, **Graviton Emission in the Bulk by a Simply Rotating Black Hole**, Phys.Rev.D80:084016,2009, [arXiv:0906.3845v3 [hep-th]]

[120] D. K. Park, **Hawking Radiation of the Brane-Localized Graviton from a $(4 + n)$-dimensional Black Hole**, Class.Quant.Grav. 23 (2006) 4101-4110, [arXiv:hep-th/0512021v5]; D. K. Park, **Emissivities for the various Graviton Modes in the Background of the Higher-Dimensional Black Hole**, Phys.Lett.B638:246-252,2006, [arXiv:hep-th/0603224v2]; E. Jung, D. K. Park, **Absorption and Emission Spectra of an higher-dimensional Reissner-Nordström black hole**, Nucl.Phys. B717 (2005) 272-303, [arXiv:hep-th/0502002v2]

[121] G. Barrand et al., **GAUDI - A Software Architecture and Framework for building HEP Data Processing Applications**, Proc. of CHEP 2000

[122] ATLAS Computing Group, **ATLAS Computing - Technical Design Report**, ATLAS TDR–017, CERN-LHCC-2005-022

[123] K. A. Assamagan et al., **Final report of the ATLAS AOD/ESD Definition Task Force**, ATLAS-SOFT-2004-006

[124] K. S. Cranmer and the ATLAS Collaboration, **The ATLAS Analysis Architecture**, ATL-SLIDE-2007-028

[125] C. M. Harris, P. Richardson, B. R. Webber, **CHARYBDIS: A Black Hole Event Generator**, JHEP0308:033,2003, [arXiv:hep-ph/0307305v2]

[126] D.-C. Dai et al., **BlackMax: A black-hole event generator with rotation, recoil, split branes and brane tension**, Phys. Rev. D77 (2008) 076007, [arXiv:0711.3012 [hep-ph]]; D.-C. Dai et al., **Manual of BlackMax, a black-hole event generator with rotation, recoil, split branes, and brane tension**, [arXiv:0902.3577 [hep-ph]]

[127] E. Boos et al., **Generic User Process Interface for Event Generators**, [arXiv:hep-ph/0109068v1]

[128] C. Buttar et al., **Standard Model Handles and Candles Working Group: Tools and Jets Summary Report**, [arXiv:0803.0678v1 [hep-ph]]

[129] G. Salam, **Jets at Hadron Colliders**, Academic Training Lecture at CERN, https://indico.cern.ch/conferenceDisplay.py?confId=115079 [2. 4. 2011]

[130] ATLAS Photos, **Simulated Black Hole Events**, http://atlas.ch/photos/atlas_photos/ /selected-photos/events/eve_gen_0101_001.jpg; http://atlas.ch/photos/atlas_photos/ /selected-photos/events/eve_gen_0101_002.jpg, [10. 1. 2011]

[131] G. Aad et al. [the ATLAS Collaboration], **Expected Performance of the ATLAS Experiment - Detector, Trigger and Physics**, CERN-OPEN-2008-020, [arXiv:0901.0512]

[132] **D. W. Miller, A. Schwartzman, D. Su, Pile-up jet energy scale corrections using the jet-vertex fraction method**, ATL-COM-PHYS-2009-180

[133] **T. Sjostrand, S. Mrenna, and P. Z. Skands, PYTHIA 6.4 Physics and Manual**, JHEP 05 (2006) 026, [arXiv:hep-ph/0603175]

[134] P. M. Nadolsky et al., **Implications of CTEQ global analysis for collider observables**, Phys. Rev. D78 (2008) 013004, [arXiv:0802.0007 [hep-ph]]

[135] G. Aad et al. [the ATLAS Collaboration], **Search for Microscopic Black Holes in Multi-Jet Final States with the ATLAS Detector at $\sqrt{s} = 7$ TeV**, to be published